Università degli Studi di Siena

Facoltà di Scienze M.F.N.

Tesi di Dottorato in Fisica Sperimentale
Ph.D. Thesis in Experimental Physics

Diffuse Gamma Ray emission detection with the AMS-02 electromagnetic calorimeter

Relatore Interno:
Chiar.mo Prof.
Pier Simone Marrocchesi

Candidato:
Federico Pilo

Relatore Esterno:
Chiar.mo Prof.
Franco Cervelli

XVI ciclo

Contents

Introduction

The all-sky observations of the EGRET experiment in the gamma band have demonstrated the correlation between the galactic structures and the gamma diffuse emission, hence confirming the model of gamma emission based on the interaction between cosmic rays and interstellar medium. Since the Galaxy is essentially transparent to high-energy gamma rays, the diffuse gamma-ray emission can be used to probe the matter and cosmic ray distributions throughout the disk of the Galaxy. The aim of theoretical studies is the development of a model consistent both with cosmic ray data and with diffuse γ-ray data *or* the clear explanation of the reason of discrepancy. In its turn, a detailed cosmic ray propagation model will provide a reliable basis for other studies such as investigation of dark matter signals in cosmic rays and diffuse γ-rays, spectrum and origin of the extragalactic γ-ray emission, theories of nucleosynthesis and evolution of elements.

Even if satellite experiments, in particular EGRET, have substantially contributed to the knowledge in the gamma band up to few GeV energy, the spectral range between 10 GeV and some hundreds GeV remains so far mostly unexplored. Energy spectrum measurements in this energy band would be very useful to fill the gap between ground based measurements and satellite measurements, and thus may allow key inspections of the current concepts concerning both the GeV and TeV regimes.

The *Alpha Magnetic Spectrometer* (AMS-02) is a space-borne experiment of new generation that may lead to a significative step forward in the comprehension of the diffuse γ-rays emission in the GeV to TeV energy band. AMS-02 is a particle detector aimed to high precision measurements of both cosmic ray and γ-ray fluxes in space. It is under construction by a world wide international collaboration and will be part of the scientific program on board the International Space Station, where it will collect data for three years. AMS-02 has been designed to investigate fundamental open questions in current astroparticle physics, including the existence of cosmological antimatter and the physical nature of the dark matter content of our galaxy. The core of the detector is a superconducting magnet, generating a very strong field and enclosing the silicon tracking system; the remaining subdetectors are the time of flight (TOF) system, the transition radiation detector (TRD), the ring imaging Čherenkov (RICH) and the electromagnetic calorimeter (ECAL).

The AMS-02 accurate measurements of cosmic-ray nuclei, protons, antiprotons, electrons and positrons will be completed by high energy gamma rays detection. The experiment will detect γ-rays, either by reconstructing e^+e^- pairs generated by photons converted before the tracker (*conversion mode*), or based on direct identification of electromagnetic showers in ECAL (*single mode*). In order to use the latter techniques, the ECAL must be provided with a neutral "stand alone" trigger able to recover the photons not acquired by the standard AMS-02 trigger based on the TOF counters. Moreover an efficient method to reject the huge background to the γ-rays signal is strongly required; the very good imaging capability of the calorimeter is much helpful for background suppression purposes. The calorimeter is a fine grained Pb-scintillating fibers sampling device designed to measure with good resolution the energy deposit over the range $1 \div 10^3\,\mathrm{GeV}$, and to image the longitudinal and the lateral development of the showers, allowing for the e/h discrimination between electromagnetic and hadronic cascades.

A research group of INFN (Gruppo collegato di Siena) partecipates to the construction and operation of the AMS-02 electromagnetic calorimeter in collaboration with the INFN group of Pisa, the Institute for High Energy Physics (IHEP) in Beijing and the Laboratory of Particle Physics (LAPP) in Annecy. My contribution to the activity of the AMS-02 ECAL group started in 1999 and touched many aspects of the detector assembly such as the characterization of photomultipliers and related electronics, the costruction of the detector "active volume", the analysis of beam test data in order to estimate the calorimeter performances. At the same time, I took part to the design of the "stand alone" trigger with Monte Carlo simulation studies and functional tests of prototype boards. My PhD thesis work continued with the implementation of new algorithms for the γ-rays identification with the aim of minimizing the background contamination. This analysis strategy was applied to MC simulated data giving, as a result, a detailed prediction of the AMS-02 sensitivity in diffuse gamma rays spectrum measurements.

The outline of the thesis, organized in seven chapters, is as follows:

Chapter 1 shows an outline of the present knowledge about the diffuse gamma rays emission from both a theoretical and an experimental point of view. Both the galactic and extragalactic components are discussed. The last results obtained by means of the GALPROP simulation code are compared with EGRET data and with other recent models.

Chapter 2 presents an overview of the overall apparatus of the AMS-02 experiment and of its main scientific goals. Charged particle detection strategies and charged Level 1 trigger system are also described.

Chapter 3 is focused on the principal features of the electromagnetic calorimeter (ECAL) and on its performances (measured by Cern beam test in the 2002) . Results of effective sampling thickness, longitudinal shower imaging, energy linearity and resolution, angular resolution are reported.

Chapter 4 illustrates the AMS-02 gamma rays detection strategy. Predicted performances for the *conversion mode* strategy are discussed. The topic of direct photon detection in ECAL is introduced.

Chapter 5 is mainly dedicated to the design of the ECAL "stand alone" trigger. The estimations of signal efficiency and of the background rate are given as well as specifications in terms of power consumption, timing and robustness.

Chapter 6 describes the analysis programs for the reconstruction and the identification of the events in the AMS-02 calorimeter. They are based on a set of selection criteria that allow to detect particles entering outside the sensitive volume, to analyze the topological shape of the shower in the calorimeter and to search for the signature of a charged particle in the other AMS-02 subdetectors. The resulting γ efficiency and the protons contamination were calculated.

Chapter 7 is focused on the computation of the expected number of gamma rays events from the Galaxy center region over a three years period. This number is computed by the AMS-02 fast simulation code which uses as input a set of exposition maps from the AMS-02 orbital simulation and a set of GALPROP γ-rays emission skymaps. Finally an estimate of the precision expected in the measurement of the galactic diffuse continuum emission is given by the reconstruction of the gamma-ray spectrum after background subtraction.

Chapter 1

Diffuse gamma rays emission

In 1967, an instrument on NASA's OSO III, with an effective area of approximately $4\,\mathrm{cm}^2$, detected the Milky Way as a source of diffuse gamma-ray emission.

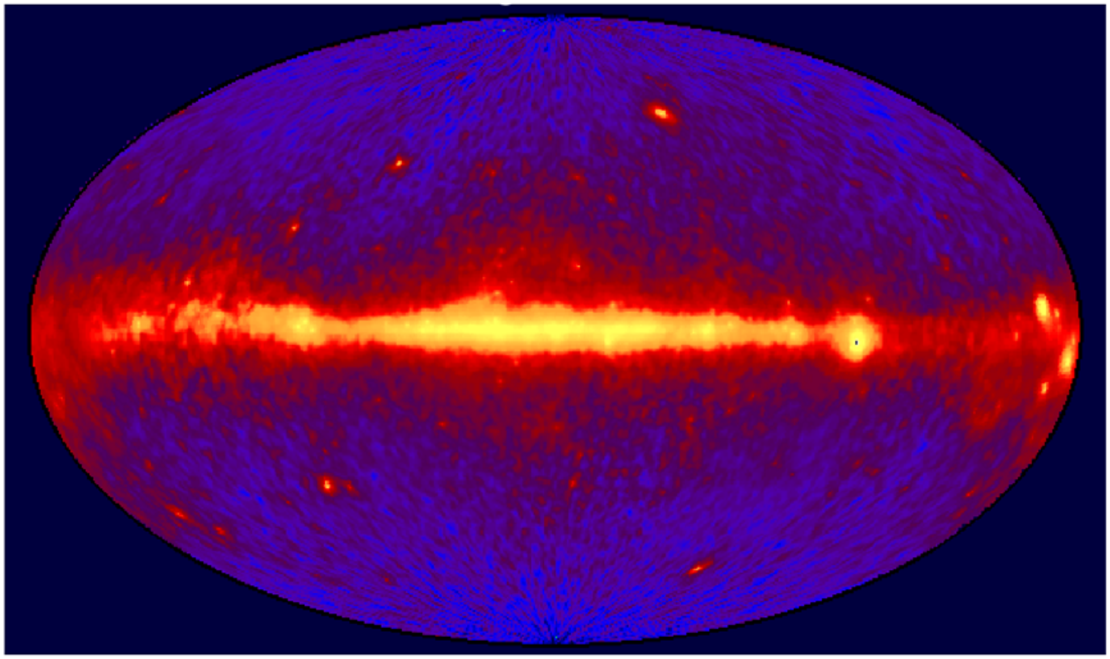

Figure 1.1: EGRET all-sky map: continuum γ-ray emission for energies $> 100\,\mathrm{MeV}$.

SAS-2, launched by NASA in 1972, had an effective area of about $100\,\mathrm{cm}^2$ and very low instrumental background. Though it operated for only six months, it was the first to detect the isotropic,apparently extragalactic, gamma-ray emission. COS-B observatory, which was launched by ESA in 1975, had an effective area of about $50\,\mathrm{cm}^2$ and greater background, owing partly to an elliptical orbit that carried it out of the magnetosphere for most of the time, but it operated for seven years. COS-B observations yielded a catalog of 25 gamma-ray point sources, including 3C 273, the first known extragalactic source. Our rudimentary understanding of the GeV γ-ray sky was greatly advanced with the launch of the Energetic Gamma Ray Telescope (EGRET) instrument on NASA's Compton Gamma-Ray Observatory (CGRO), which operated from 1991 April until 2000 May. EGRET observed the entire sky in the energy range from 30 MeV to over 30 GeV. The number of previously known GeV γ-ray sources increased from 1-2 dozen to the 271 listed in the 3rd EGRET catalog.

Together with COMPTEL, the low energy range ($0.75 \div 30\,\mathrm{MeV}$) instrument on board CRGO, EGRET unveiled the spectrum of the diffuse continuum γ-ray emission and, thus, it has shown the great potential of γ-rays in covering many "hot topics" of modern astrophysics and cosmology, such as the origin of galactic and extragalactic cosmic rays, particle acceleration and radiation processes under extreme astrophysical conditions, the search for dark matter. High energy gamma rays are excellent probes for non-thermal high-energy processes in the Universe: they penetrate the whole Universe without significant absorption and, traveling along straight lines, transport information about high energy interactions from distant sites and extreme energetic objects or events to the observer.

This Chapter reviews the present knowledge about the origin of the diffuse γ-ray emission, from both the theoretical and observational points of view. The great uncertainty of the theoretical model predictions clearly justifies future gamma ray missions with new generation detectors like GLAST and AMS-02. A high priority objective of future instrumental developments will be an attempt of exploration of the energy interval between 10 and a few hundred GeV. The interest to this relatively narrow energy band is motivated not only by the natural desire to enter a new domain which remains a *terra incognita*, but also because it provides a bridge between the high and very high astronomies, and thus may allow key inspections of the current concepts concerning both the GeV and TeV regimes.

The diffuse γ-ray emission supposedly consists of several components: truly diffuse Galactic emission from the interstellar medium, the extragalactic background (EGB), whose origin is not firmly established yet, and the contribution of unresolved and faint Galactic point sources. The Galactic diffuse emission dominates other components and has a wide distribution with most emission coming from the Galactic plane.

1.1 Diffuse Galactic emission

The dominant feature of the high-energy gamma-ray sky is the narrow band of intense emission along the Galactic plane, which arises from cosmic-ray interactions with gas ambient photon field. This emission is stronger within $\pm 60°$ in Galactic longitude (l) and $\pm 10°$ in Galactic latitude (b), where the most part of the interstellar gas is located, while it rapidly decreases at higher latitudes.

The Galactic diffuse γ-rays are produced in energetic interactions of CR nucleons with gas, via neutral pion production, and by electrons, via inverse Compton (IC) scattering and bremsstrahlung. Since the Galaxy is trasparent to high energy γ-rays, the observed γ-ray emission is the line-of-sight integral over the emissivity of the interstellar medium. The latter is essentialy the product of the cosmic ray density and the density of the gas or radiation field. So, while direct measurements of cosmic rays are possible in only one location on the outskirts of the Milky Way, Galactic diffuse γ-rays provide insights into the spectra of cosmic rays in distant location, therefore completing the local cosmic ray studies.

This connection, however, requires extensive modeling and is yet to be explored in detail. Before proceeding with the description of the diffuse Galactic emission models, we will briefly summarize the principal characteristics of the cosmic rays and of the interstellar medium that are used as constraints to the parameters of the models.

1.1.1 Cosmic rays

Cosmic rays (CR) play a primary role in determining the dynamics and processes in the interstellar medium: the energy density of relativistic particles is about $1\,\mathrm{eV\ cm^{-3}}$, comparable to the energy density of the interstellar radiation field, magnetic field, and turbolent motions of the interstellar gas. Meanwhile the origin, spectrum and composition of the CR have been debated for almost a century. Only in the last decade, analysing the EGRET observations of the Small Magellanic Cloud (SMC) [1], the long-standing question about the origin of the cosmic rays was answered. The SMC is one of the closest galaxies to our own and, according to measurements, is in a state of irreversible disintegration. The flux of γ-rays escaping from the SMC was measured by EGRET considerably lower than the expected. Thats clearly reflects a cosmic rays density greatly below that in our Galaxy and is consistent with the concept that the cosmic rays are a Galactic and not a “metagalactic” phenomenon.

The relative abundances of the different elements are related to the composition at the source and to the propagation history of cosmic rays. The sources of cosmic rays are believed to be supernovae and SNRs, pulsars, compact objects in close binary system, and stellar winds. The power required to mantain the observed CR energy density ($5 \times 10^{40}\,\mathrm{erg\,s^{-1}}$) can be provided by supernova explosions, whose rate in our Galaxy is 1 every 30 years, if only the $5\,\%$ of the kinetic energy of the ejecta is transferred to cosmic rays. This value is in agreement with the prediction of the diffusive acceleration theory applied to strong shock waves. Particles accelerated near the sources propagate in the interstellar medium where they lose or gain energy and produce secondary particles and gamma-ray, changing their initial spectra and composition. When possible, cosmic rays escape from our Galaxy with a typical time scale of 10 Mys. Primary cosmic rays are mainly constituted of protons ($\sim 90\,\%$) and helium nuclei ($\sim 10\,(\%)$) with small abundances of electrons ($\mathcal{O}(1\,\%)$) and all other elements. The destruction of primary nuclei via spallation gives rise to the secondary nuclei and the isotopes which are rare in nature, to the antiprotons and to the pions which decay producing γ-rays and secondary positrons and electrons.

The cosmic ray nuclei are characterized by a power-law spectral flux $dF/dE \propto E^{-\beta}$ with an index β that changes at two break-energies, the “knee” and the “ankle”. In the interval $10^{10}\,\mathrm{eV} < E < E_{knee} \sim 3 \times 10^{15}\,\mathrm{eV}$, the spectral index β_1 is around 2.7, while steepens to $\beta_2 \sim 3.0$ in the interval $E_{knee} < E < E_{ankle} \sim 3 \times 10^{18}\,\mathrm{eV}$, flattening again to $\beta_3 \sim 2.5$ above E_{ankle}. The various changes in the spectral index reflect the different origin and propagation history of cosmic rays with different energy. During supernova explosion, the expanding shock wave is able to accelerate charged particles up to the knee range. Collisionless shock simulations [2] indicate a source spectrum dF^s/dE with index $\beta_s \sim 2.2$. After acceleration, the spectrum of CR nuclei is modulated by their residence time in the Galaxy, $\tau_{gal}(E)$. For a steady source of cosmic rays the energy dependence of the observed flux is roughly that of $\tau_{gal} \cdot dF^s/dE$. Observations of astrophysical and solar plasmas and of nuclear abundances as a function of energy [3] indicate that $\tau_{gal}(E) \propto E^{-0.5\pm0.1}$, explaining $\beta_1 \sim \beta_s + 0.5 \sim 2.7$. Above E_{knee}, the existence of measurable CR fluxes requires a new kind of engine in our Galaxy: a reacceleration process can take place in the vicinity of the pulsars [4], where the rapidly rotating magnetic field is a powerful astrophysical dynamo.

Fig. 1.2 (a) shows the most recent measurements in the primary proton spectrum. Below 10 GeV the proton flux is dumped by the solar wind originated by solar activity and shows a not fully understood periodical modulation (called *solar modulation*). Thus the measured spectrum is not the same as the average galactic spectrum, neither it is the same as the local interstellar spectrum (LIS), i.e. the spectrum outside the eliosphere but not too distant from the sun.

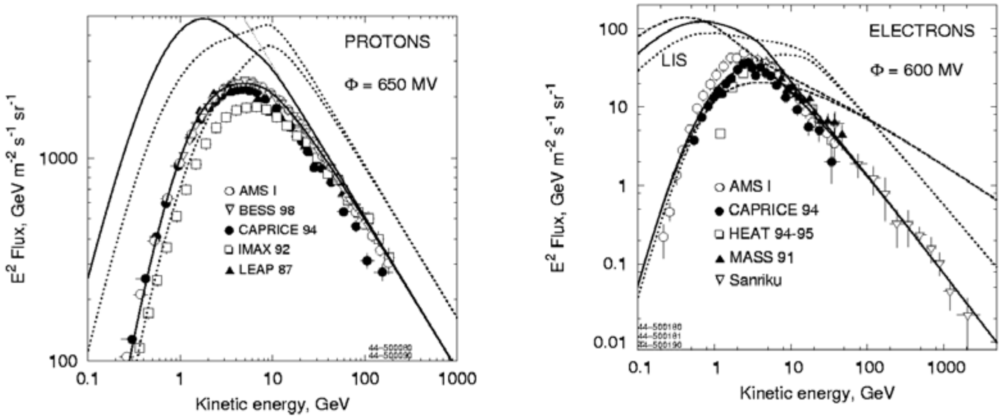

(a) (b)

Figure 1.2: (a) Calculated proton spectra using different models (solid lines and dots) compared with data (upper curve - LIS, lower - with solar modulation of 650 MV). (b) Calculated electron spectra using different models (solid lines and dots) compared with data (upper curve - LIS, lower - with solar modulation of 600 MV). Adapted from [21].

Cosmic ray electrons are probably accelerated by the same engines that accelerate CR protons and nuclei. To the extent that particle-specific losses (such as synchrotron radiation) can be neglected at the acceleration stage, for electrons below the "electron's knee" at $E_e = (m_e/m_p)E_{knee} \sim 2\,\mathrm{TeV}$, we expect $dF_e^s/dE \propto E^{-\beta_s}$, with $\beta_s \sim 2.2$. But, unlike hadrons, the electrons suffer large energy losses due to electromagnetic processes as synchrotron radiation, bremsstrahlung and inverse Compton scattering. This implies that the CR electron spectrum is modulated mainly by their "cooling" time which is shorter than their galactic confinement time, $\tau_{gal}(E)$, above a relatively low energy.

According to [6], the energy loss is governed by the rate at which a single electron interacts with the ambient electromagnetic fields, weigthed by the corresponding average energy density:

$$\mathrm{P} = \sigma_T c \left[n_\star \varepsilon_\star + n_0 \varepsilon_0 + \frac{B^2}{8\pi}\right] \tag{1.1}$$

where σ_T is the Thomson cross-section, $n_\star \simeq 0.22\,\mathrm{cm}^{-3}$ and $\varepsilon_\star \simeq 1\,\mathrm{eV}$ are the number density and the mean energy for the galactic starlight, $n_0 \simeq 411\,\mathrm{cm}^{-3}$ and $\varepsilon_0 \simeq 2.7kT_0 \simeq 6.36 \times 10^{-10}\,\mathrm{MeV}$ are the number density and the mean energy of the CMB. Finally $B^2/(8\pi) \simeq 1\,\mathrm{eV\,cm}^{-3}$ is the magnetic energy density.

Starting from Eq. 1.1, the electrons spectrum shape can be computed resulting in a spectral index $\beta_e = \beta_s + 1 \sim 3.2$, in good agreement with experimental data. The dependency of the cooling time of the electrons from energy is written as $\tau_{cool}(E) \propto E^{-1}$. At sufficiently low energy, then, $\tau_{gal} < \tau_{cool}$, and processes other than Compton or synchrotron cooling (such as bremsstrahlung) become relevant. This implies another change in the spectral index, but it occurs at $E < 10\,\mathrm{GeV}$, a range in which local modulation would mask the effect.

For energy above the "electron's knee", $E_e > (m_e/m_p)E_{knee}$, the spectrum should steepen up by $\Delta\beta \simeq 0.25$, like that of CR hadrons. Anyway the available spectral measurements extend only to $E_e \leq 1.5\,\mathrm{TeV}$.

1.1.2 Galactic Structure

The morphology of the Galaxy, the distribution of the gas and of the interstellar radiation are key parameters in modelling the gamma ray diffuse emission. Also the synchrotron emission is very important since it provides limits on the interstellar electron spectrum.

The Galaxy is a barred spiral with a radius of about 30 kpc whose gas's content is dominated by atomic (H_I) and molecular hydrogen (H_2). They are present in approximately equal quantities ($\sim 10^9 M_\odot$) in the inner Galaxy, but with different radial distributions. The H_I is mapped directly via 21 cm radio line surveys, which provide both distance and density information [5]. Its surface density is lower than $1.9\,\mathrm{M_\odot\,pc^{-2}}$ within a radius of 6 kpc from the Galactic center, attains the maximum values at radii 7 - 12 kpc, where it becomes larger than $4\,\mathrm{M_\odot\,pc^{-2}}$, and then decreases toward the outer region up to 17 kpc. The H_I disk is asymmetric with warping in the outer disk, and it extends to about 1.5 kpc above the Galactic plane and to about 1 kpc below. The gas density is roughly uniform at $1\,\mathrm{atom\,cm^{-3}}$ and a typical scale height is about 200 pc. The molecular hydrogen, devoid of a permanent electric dipole moment, is almost impossible to be observed directly: the 115 GHz emission of the abundant molecule ^{12}CO is a good "tracer", since it forms in the dense clouds where the H_2 resides [7]. The H_2 is distributed within 10 kpc with a peak around 5 kpc and small scale height of about 70 pc (Fig. 1.3 (a)). It is concentrated mainly in dense clouds with sizes of 50 - 200 pc with typical density of $10^4\,\mathrm{atom\,cm^{-3}}$. Beside atomic and molecular hydrogen, the presence of ionized hydrogen H_{II} is detected at lower densities ($\sim 10^{-3}\,\mathrm{atom\,cm^{-3}}$), but with much larger vertical extent (1 kpc height). In addition to hydrogen, the interstellar gas contains heavier elements, dominated by helium, with a ratio of $\sim 10\,\%$ by number relative to hydrogen.

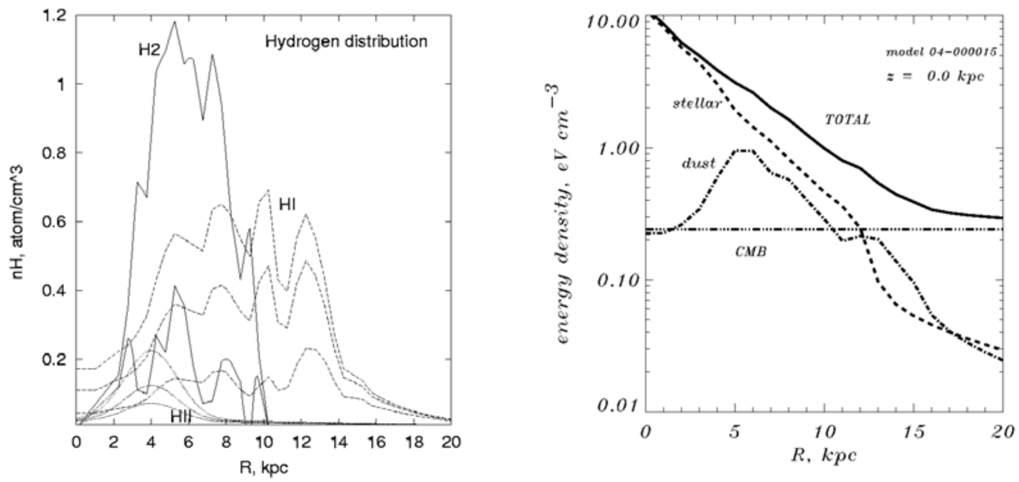

(a) (b)

Figure 1.3: (a) Number density distributions of $2\times\mathrm{H}_2$ (solid), H_I (dashes) and H_II in the Galaxy. Shown are the plots for different distances from the galactic plane ($z = 0, 0.1, 0.2$ kpc, decreasing density). Adapted from [17]. (b) ISRF energy density as a function of the Galactocentric radius R at $z = 0$. Adapted from [14].

The interstellar radiation field (ISRF) is made up of contributions from starlight, emission from dust and cosmic microwave background (CMB). The infrared surveys by the IRAS and COBE satellites have greatly improved our knowledge of both stellar distribution and dust emission. The ISRF has a vertical extent of several kpc, where the Galaxy acts as a disk-like sources of radius ~ 10 kpc. The radial distribution of the stellar component is also centrally peaked while the dust component is related to that of the neutral gas ($\mathrm{H}_\mathrm{I} + \mathrm{H}_2$) and is therefore distributed more uniformly.

Observations of synchrotron intensity and spectral index provide essential and stringent constraints on the Galactic magnetic field and on the interstellar electron spectrum. The average strength of the *total* field is $6 \pm 2\,\mu$G locally and about $10 \pm 3\,\mu$G at 3 kpc from the galactic center [8]. The radial scale is 10 kpc while a reasonable value for the scale height is 2 kpc. Cosmic ray electrons travelling in the Galactic magnetic field undergo syncthroton emission. The emission in the 10 MHz - 10 GHz band constrains the electron spectrum in the $\sim 1 - 10$ GeV range [9]. In particular the synchrotron spectral index ($T \propto \nu^{-\gamma}$) provides information on the interstellar electron spectral index β according to the relation:

$$\gamma = 2 + \frac{\beta - 1}{2} \tag{1.2}$$

1.1.3 Diffuse emission models

In theoretical models, the locally observed spectra of cosmic rays and the Galactic distribution of interstellar gas and soft photons field are used to predict the intensity, $j(E_\gamma, l, b)$, of diffuse gamma rays of energy E_γ emitted from a sky region of Galactic longitude l and latitude b. In a general form, the intensity is expressed by:

$$\begin{aligned} j(E_\gamma, l, b) &= \frac{1}{4\pi}\int [c_e(\rho,l,b)q_{em}(E_\gamma) + c_n(\rho,l,b)q_{nm}(E_\gamma)] \\ &\quad \times[n_{\mathrm{H_I}}(\rho,l,b) + n_{\mathrm{H_{II}}}(\rho,l,b) + n_{\mathrm{H_2}}(\rho,l,b)]d\rho + \\ &\quad \frac{1}{4\pi}\sum_i \int c_e(\rho,l,b)q_{pi}(E_\gamma,\rho)u_{pi}(\rho,l,b)d\rho \\ &\quad \mathrm{ph.\,cm^{-2}\,s^{-1}\,sr^{-1}\,GeV^{-1}} \end{aligned} \tag{1.3}$$

The first integral represents the γ-ray production due to cosmic ray interactions with matter, where $q_{em}(E_\gamma)$ and $q_{nm}(E_\gamma)$ are the electron bremsstrahlung and nucleon-nucleon production functions per target H atom based on the local cosmic ray density, i.e., in the vicinity of the Sun. The functions $c_e(\rho, l, b)$ and $c_n(\rho, l, b)$ are the ratios of the electron and nucleon cosmic ray intensities relative to the local intensities. These functions could also depend on the energy if the spectral indices vary with location in the Galaxy. The quantities $n_{\mathrm{H_I}}(\rho, l, b)$, $n_{\mathrm{H_{II}}}(\rho, l, b)$ and $n_{\mathrm{H_2}}(\rho, l, b)$ are the three-dimensional density distributions of atomic and molecular hydrogen.

The second integral describes the contribution from inverse Compton interactions between cosmic ray electrons and ISRF photons. The summation is over discrete wavelength bands: cosmic black-body radiation, far-infrared, near-infrared two optical bands, and ultraviolet, with photon energy density distributions $u_{pi}(\rho, l, b)$. The production function $q_{pi}(E_\gamma, \rho)$ is based on the local electron spectrum.

Conventional models

The first detailed analysis of the diffuse γ-ray emission from the Galactic plane ($300° < l < 60°$ and $|b| \leq 10°$) is presented in Hunter et al. (1997) [10]. The basic assumptions of this calculation were that (i) the cosmic rays are Galactic in origin, (ii) that a correlation exists between the cosmic ray density and interstellar matter in the Galaxy, and (iii) that the spectra of nucleons and electrons in the Galaxy are the same as observed in the solar vicinity. Under these hypothesis, the functions c_e and c_n of Eq. 1.3 are independent of energy. The electron-to-proton ratio is thus assumed constant throughout the Galaxy and the cosmic ray density is inferred on a broad scale from the distribution of the matter using an adjustable coupling scale r_0.

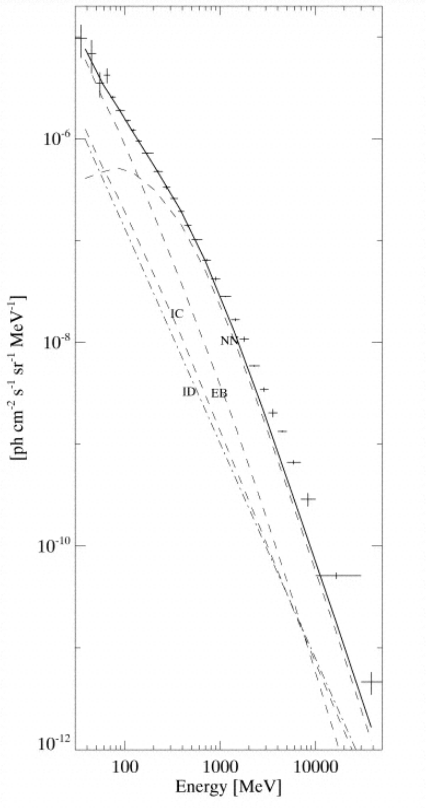

Figure 1.4: Average diffuse γ-ray spectrum of the inner Galaxy region, $300° < l < 60°$, $|b| \leq 10°$. The best-fit model calculation plus the isotropic diffuse emission is shown as the solid line. The individual components of this calculation, nucleon-nucleon, electron bremsstrahlung, and inverse Compton, are shown as dashed lines. The isotropic diffuse emission [32] is shown as a dash-dotted line. Adapted from [10].

In Fig. 1.4 the spatial distribution of the diffuse emission, determined from EGRET data after removing the contribution from point sources detected with greater than 5 σ significance, is compared to the model. The good agreement between model and observations support the assumption that the cosmic ray are coupled to the matter on the scale of r_0 and are not uniformly distributed. Thus, it is reasonable to assume that, in our Galaxy, the expansive pressures from the cosmic rays, the interstellar matter and the magnetic fields are in dynamic balance with the overall gravitational attraction of the interstellar matter.

Nevertheless the emission in the outer Galaxy is not well predicted by the model, indicating that cosmic-rays are perhaps coupled less well to the matter in the outer Galaxy and that the IC component is underestimated [11]. Beside this, the observed intesity above 1 GeV exceeeds the model prediction by about 60 % and this *excess* appears at *all latitudes/longitudes ranges.*

Over the years Moskalenko, Strong and their collaborators have developed what is presumably the most elaborate and detailed understanding of CR, radio and γ observations of our Galaxy [13], [22], [20].

The GALPROP cosmic ray and γ-ray propagation computer code has been developed with the aim to reproduce self-consistently observational data of many kinds related to CR origin and propagation: direct measurements of nuclei, antiprotons, electrons and positrons, γ-rays, and synchrotron radiation. Using numerical solution of the propagation equation, the method computes three-dimensional models of our Galaxy. The models have cylindrical symmetry in the Galaxy, and the basic coordinates are (R,z,p), where R is Galactocentric radius, z is the distance from the Galactic plane and p is the total particle momentum. The propagation region is bounded by $R_h = 30\,\mathrm{kpc}$ and $\pm z_h$, beyond which free escape of particle is assumed.

The reaction network is solved starting from the heaviest nuclei. The propagation is solved first giving the primary distribution as a function of (R, z, p) and all resulting secondary source functions obtained from the gas density and cross sections; then proceeds to the nuclei with $A - 1$ and is repeated down to $A = 1$. In this way all secondary, tertiary, etc., reactions are automatically accounted for. Once the Galaxy model is obained, γ-ray intensities are computed self-consistently from the gas and radiation fields used for propagation, using Eq.1.3.

The general propagation equation is written in the form:

$$\begin{aligned}\frac{\partial\psi}{\partial t} &= q(\boldsymbol{r},p) + \boldsymbol{\nabla}\cdot(D_{xx}\boldsymbol{\nabla}\psi - \boldsymbol{V}\psi) + \frac{\partial}{\partial p}p^2 D_{pp}\frac{\partial}{\partial p}\frac{1}{p^2}\psi \\ &\quad -\frac{\partial}{\partial p}[\dot{p}\psi - \frac{p}{3}(\boldsymbol{\nabla}\cdot\boldsymbol{V})\psi] - \frac{1}{\tau_f}\psi - \frac{1}{\tau_r}\psi \qquad (1.4)\end{aligned}$$

where $\psi = \psi(\boldsymbol{r}, p, t)$ is the density per unit of total particle momentum[1] with $\psi(R_h, z, p) = \psi(R, \pm z_h, p) = 0$ according to the previously described boundary conditions, $q(\boldsymbol{r}, p)$ is the source term, $\dot{p}$ is the momentum loss rate, τ_f is the time scale for fragmentation, and τ_r is the time scale for the radioactive decay.

Two kinds of spatial propagation mechanisms are usually taken in account: in diffusion/convection models, the diffusion is regulated by coefficient D_{xx} and the convection velocity, $V(z)$, is assumed to increase linearly with distance from the Galactic plane; in diffusion/reacceleration models, $V(z) = 0$ and the momentum space diffusion coefficient D_{pp}, related to D_{xx} using the formula given in [15], is added to describe a CR reacceleration phenomenon. For a given z_h, the dependency of D_{xx} from particle's rigidity is taken as $D_{xx} = v/c\, D_0(\rho/\rho_0)^\delta$ and is determined fitting boron-to-carbon (B/C) ratio data [13]. While with diffusion/convection models the fit to the data if obtained only with a break in D_{xx} (i.e. $\delta = \delta_1$ below rigidity ρ_0, $\delta = \delta_2$ above), reacceleration provides a natural mechanism to reproduce the B/C ratio without an ad hoc form for the diffusion coefficient.

The limits on z_h are based on the comparison of the ^{10}Be/^{9}Be ratio observed by Ulysses [16] with model predictions as a function of z_h, being all other parameters fixed at their adopted values. In diffusion/reacceleration models, a lower limit of 4 kpc and an upper of 12 kpc are compatible with data.

---

[1] $\psi(p)dp = 4\pi p^2 f(\boldsymbol{p})$ in terms of phase-space density $f((\boldsymbol{p})$.

The distribution of primary CR sources is obtained empirically by requiring consistency (after propagation) with the cosmic ray distribution determined by analysis of EGRET γ-ray data [12]. For secondary nucleons, the source term is $q(\boldsymbol{r}, p) = v\, \psi_p(\boldsymbol{r}, p)[\sigma^{ps}_{\mathrm{H}} n_{\mathrm{H}}(\boldsymbol{r}) + \sigma^{ps}_{\mathrm{He}} n_{\mathrm{He}}(\boldsymbol{r})]$, where σ^{ps}_{H}, $\sigma^{ps}_{\mathrm{He}}$ are the production cross sections for the secondary from the progenitor on H and He targets, ψ_p is the progenitor density, and n_{H}, n_{He} are the interstellar hydrogen and Helium number densities.

The injection spectrum of nucleons is assumed to be a power law in momentum for different species, $dq(p)/dp \propto p^{-\beta_s}$. In "conventional" models the injection spectra and the propagation parameters are chosen to reproduce the most recent measurements of local primary and secondary nuclei. In particular, the antiproton and positron data, tracing the protons on a large scale (up to $\sim 10\,\mathrm{kpc}$), provide an important constraint on the intensity normalization of the average spectrum. For protons and Helium, a break in the spectrum is introduced below 10 GeV: for the protons β_s is assumed equal to 1.98 below 9 GV rigidity and 2.42 above 9 GV rigidity (solid lines of Fig. 1.2 (a)).

For primary electrons the injection spectrum still follows a power law adjusted to reproduce the local measurements, γ-ray and synchroton data: the spectral index is 1.6 below 4 GV, ~ 2.5 above 4 GV (solid lines of Fig. 1.2 (b)).

Energy losses for nucleons by ionization and Coulomb interactions are included, and for electrons by ionization, Coulomb interactions, bremsstrahlung, inverse Compton (IC) on ISRF, and synchrotron radiation. Secondary and tertiary antiprotons are calculated [17] along with secondary positron and electron production [18]. In particular secondary positrons contribute about half of the total lepton flux at $\sim 1\,\mathrm{GeV}$ while secondary electrons add up another 10 %. This leads to a considerable contribution of secondary positrons and electrons to the diffuse γ-ray flux via IC scattering and bremsstrahlung and significantly increases the flux of diffuse Galactic γ-rays in the MeV range.

The expected γ-ray spectra in 7 test regions are shown in Fig. 1.5, where they are compared with data. Respect to the analysis reported by Hunter et al. (1997) [10] corresponding to the first region on the top row, the spectra are computed also for the "outer Galaxy" and for regions with high latitudes ($b \leq 90°$). A more complete set of EGRET data, with energies up to 120 GeV, has been used. However, since the actual number of photons with $E > 10\,\mathrm{GeV}$ is small and concentrated mainly in the inner Galaxy, the comparison with models above 10 GeV has been made only in this region. The study confirmed that "conventional" models are consistent with γ-ray measurements in the 30 MeV - 500 MeV range, but outside this range excesses are evident. The GeV excess appears again in all latitude/longitudes ranges.

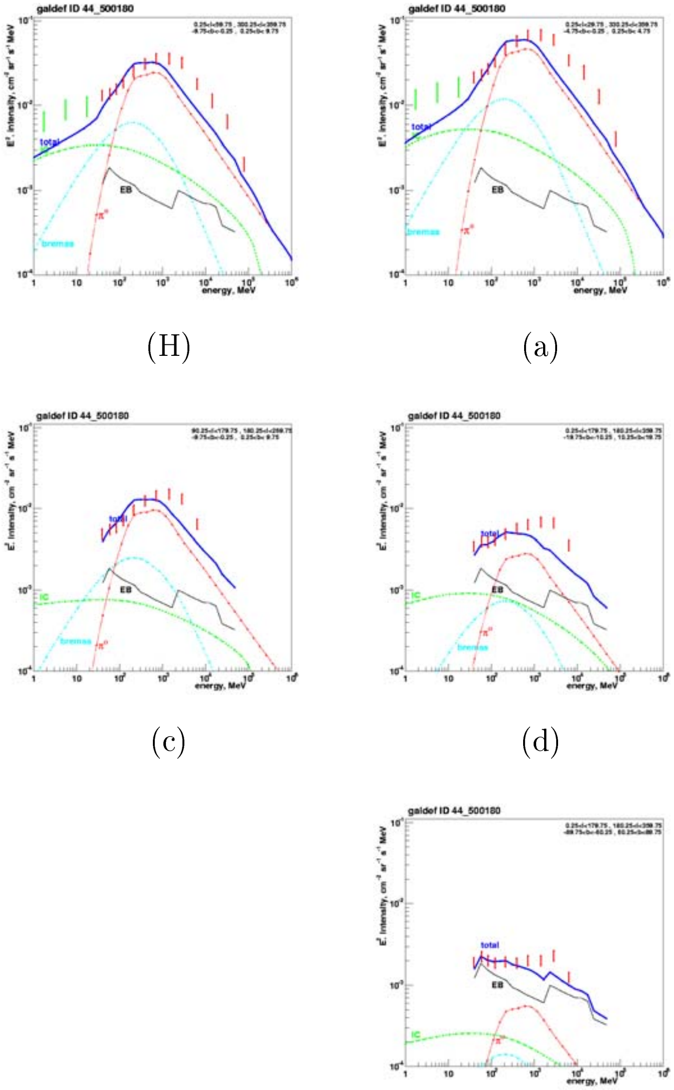

(H) (a) (b)

(c) (d) (f)

(g)

Figure 1.5: γ-ray spectrum of conventional model for 7 sky regions: Hunter et al.(1997) [10] region (H), inner Galaxy (a), Galactic plane avoiding inner Galaxy (b), outer Galaxy (c), intermediate latitudes (d,f), Glactic poles (g). The model components are: π^0 decay (dots, red), IC (dashed, green), bremstrahlung (dash-dot, cyan), EGB (thin solid, black) added only to EGRET data, total (thick solid, blue). EGRET data: red vertical bars. COMPTEL data: green vertical bars. Adapted from [20].

Towards an optimized model

The GeV excess is unlikely to be an instrumental effect, in particular because the Crab spectrum is observed as a single power-law with no indication of an excess at GeV energies. Since the GeV excess appears in all latitude/longitudes ranges, this implies that is not a feature restricted to the Galactic ridge or the gas-related emission. Furthermore a simple re-scaling of the π^0-decay component does not improve the fit in any region, since the observed peak is at an energy higher than the π^0 peak. A population of unresolved sources can not help to explain the excess either, since the excess is also present at high Galactic latitudes. These are all arguments towards a substantial inverse Compton component at high energies.

As explained in Section 1.1.1, high-energy electrons suffer energy losses so rapidly, that they do not propagate very far from their sources. As a result, the spatial distribution of these electrons would be inhomogeneous and the locally observed spectrum would not be representative for electron spectra at other places in the Galaxy, where they could be substantially harder. According to [19], the corresponding hard IC gamma-ray spectrum, would explain much of the GeV excess. In these calculations it was assumed that the electrons are instantly released when accelerated and that the electron acceleration would proceed for 10^4 to 10^5 years in a typical remnant. GeV-scale IC emission is produced by TeV-scale electrons, which have a radiative lifetime of about 10^5 years. During that time the average electron will propagate about 300 pc, so that the SNR would be embended in a cloud of high-energy electrons with radius 300 pc. Seen from a distance, say 5 kpc away, the corresponding enhancement in the IC intensity wold have a radius of about 3°. The enhancements at distances less than 5 kpc from us would not be point sources for EGRET and, consequently, would be subsumed with the diffuse Galactic emission as originally assumed. In order to include fluctuations in the source spectra in the GALPROP code, a model with explicit time-dependence and a stochastic SNR population has been developed (see Fig. 1.6). The results indicate that, although the inhomogeneities are large, they are insufficient to explain the GeV excess [22].

Other models with a hard electron injection index (β_s) of about 2 without breaks have been computed, reproducing quite well the GeV excess in all sky areas except for the inner Galaxy [23]. However the spectral shape is not well reproduced. Moreover comparing with the EGRET data above 10 GeV from the inner Galaxy, the spectrum is much too hard.

At present, the best model seems to be a new one with moderate changes of electron and nucleon spectra relative to the “conventional” models. This changes

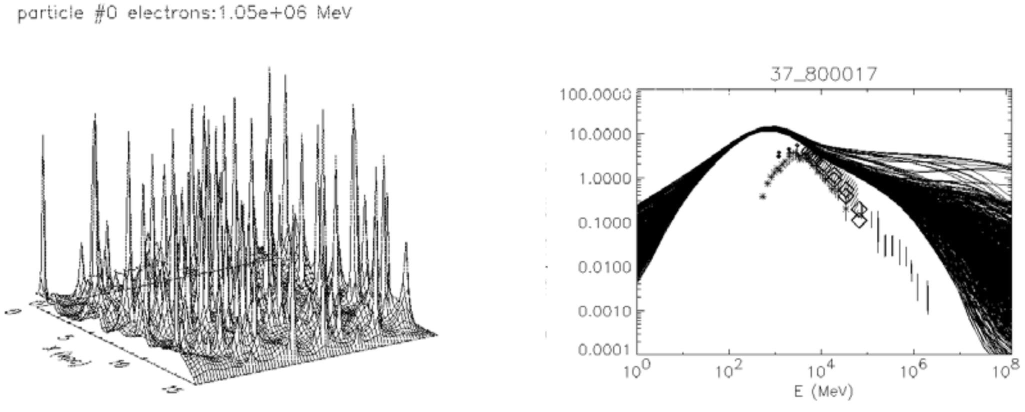

(a) (b)

Figure 1.6: Simulated distribution if 1 TeV electrons at $z = 0$ (a) and spectral variations in $4 < R < 10$ kpc compared with locally measured electron spectra (b). Adapted from [22].

are compatible with the direct measurement, considering fluctuations due to energy losses and the stochastic character of cosmic ray sources and propagation. In the "optimized" model [20], the adopted average electron spectrum resembles the local one with a steepening from 1.5 to 2.42 at 20 GeV, but it is normalized upward by a factor of ~ 4 (dots in Fig. 1.2 (b)). The proton injection spectrum is also normalized upward, by a factor 1.8; it has the same shape as for the electrons, but the break is at 10 GeV (dots in Fig. 1.2 (a)). This allows to fit the γ-ray spectrum, while still remaining within the constraints provided by the locally-observed antiproton and positron spectra.

The proposed scenario implies a substantial contribution of IC at all energies, but especially below 100 MeV and above 1 GeV. Furthermore IC dominates al latitudes $|b| > 10°$ at all energies. The spectra in different sky regions are satisfactory reproduced and there is no longer a significant GeV excess. Hence the γ-rays spectrum can be reproduced from 30 MeV to 100 GeV.

1.2 The extragalactic emission

The extragalactic diffuse γ-ray emission is the component of the diffuse emission which is most difficult to determine. Its spectrum depends much on the adopted model for the diffuse Galactic background which is not yet firmly established: even at the Galactic poles the isotropic component is comparable with the Galactic contribution from IC scattering of galactic cosmic ray electrons to the diffuse γ-ray background. The size of the halo, the electron spectrum there, and the spectrum of low-energy background photons are all model dependent and derived from many different kinds of observations.

The origin of the ERGB is still unknown. Neither is known if it is truly diffuse or it results from unresolved sources contributions. The most conservative hypothesis is that it arises primarily from the integrated emission of unresolved Active Galactic Nuclei (AGNs) [24]. EGRET detected a large number of a subset of active galaxies called blazars. Blazars are believed to possess a relativistic jet aligned very close to the line-of-sight. The average spectral energy distribution for gamma-ray blazars indicates maximal power output at gamma-ray energies. With current blazar detections that go out to red-shifts of 2.5, it can be argued that a cosmological distribution of gamma-ray blazars spread over a large range of redshifts can contribute to a uniform (at least at angular scales of many degrees) EGRB. Under more exotic hypothesis, a component of ERGB could originate from evaporation of primordial black holes [27] [28], annihilation of weakly interactive big-bang remnants [30], million solar-mass black holes which collapsed at very high redshift [29]. Moreover, ERGB can provide very important information about the phase of baryon-antibaryon annihilation [26], extragalactic infrared and optical photon spectra [31].

Extensive works has been done by Sreekumar et al. (1998) [32] and Strong et al. (2004) [21] to derive the spectrum of the ERGB based on EGRET data. In both cases the relation of modelled-Galactic-diffuse-emission vs. total-diffuse-emission was used to determine the ERGB as the extrapolation to zero column density. Assuming:

$$I_{total}(l, b, E) = A + B \times I_{Gal}(l, b, E) \tag{1.5}$$

the slope, B, of a straight line fitted to a plot of observed emission versus the Galactic model gives an independent measure of the normalization of the model while the intercept, A, equals the extragalactic emission (see for example Fig. 1.7 (a)). The difference between the two estimations for the ERGB lies in the model for the Galactic diffuse emission. While the previous works rely on the Hunter et al. (1997) model, the second rely on the optmized GALPROP model described in section 1.1.3. In the first model the flux is well described by a power law:

$$\frac{d\mathrm{F}_\gamma}{dE} \simeq (2.74 \pm 0.11) \times 10^{-3} [\frac{E}{MeV}]^{-2.10 \pm 0.03}\,\mathrm{cm}^{-2}\,\mathrm{s}^{-1}\,\mathrm{sr}^{-1}\,\mathrm{MeV}^{-1} \tag{1.6}$$

In the second model the spectrum is not consistent with a power law: it appears to be steeper than -2.10 with an indication of a possible upturn at $\sim 10\,\mathrm{GeV}$ (see

Fig. 1.7 (b)). The positive curvature in the newly determined ERGB is interesting, and it is to be expected in the “unresolved blazar origin hypothesis” of ERGB [25].

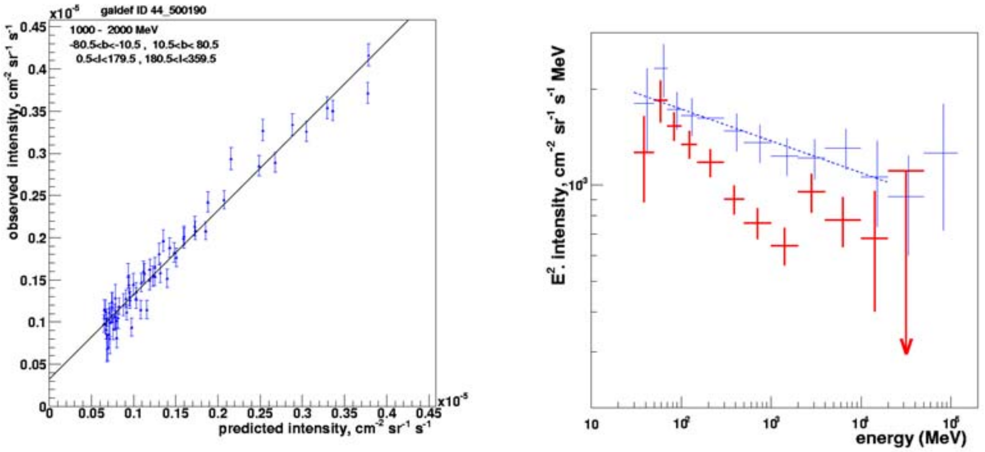

(a) (b)

Figure 1.7: (a) Observed versus predicted intensities using GALPROP model in the 1 - 2 GeV energy range. Predicted is Galactic only, intercet is ERGB. (b) Comparison of Strong et al. (2004) (solid, red) with Sreekumar et al. (1998) (dots, magenta). The dashed (blue) line is the fit of Sreekumar et al. (1998). Adapted from [21]

1.3 Faint sources and tracers of exotic physics

Blazar AGNs compose the largest fraction of identified γ-ray emitters in the EGRET range. Known to emit up to the highest energies, a significant number of not-yet-discovered and unresolved AGN is expected to contribute to the γ-ray sky [24] [33] [34]. There is a consensus that blazars should contribute between 25 % and 100 % to the observed extragalactic diffuse emission. Also contributions from other extragalactic faint sources, like normal galaxies [35] [10], galaxy clusters [36], distant γ-ray burst events have been suggested.

Faint sources will likely contribute also to the diffuse Galactic emission. In the 1-30 MeV range, it appears difficult to account for all the emission observed by COMPTEL in terms of interstellar processes (bremsstrahlung/inverse Compton), and hence a significant source contribution has been proposed. The contribution of pulsars to the Glactic diffuse emission is supposedly very little at MeV-energies, but

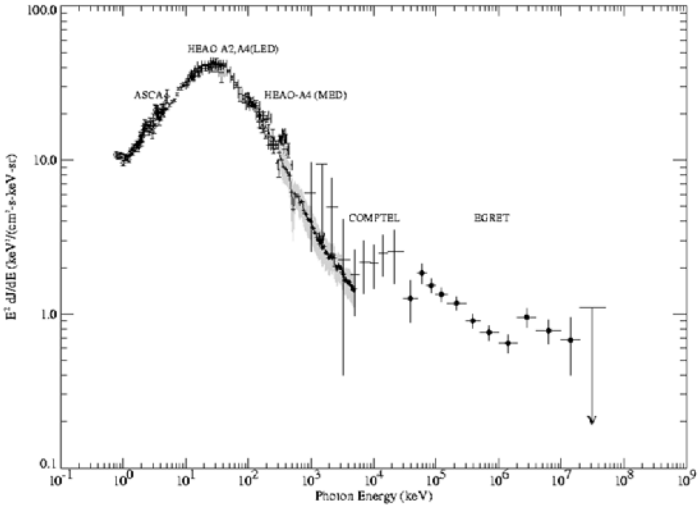

Figure 1.8: Extragalactic X-ray and γ-ray spectrum. Adapted from Strong et al. (2004) [21]

might in the order of $\sim 20\,\%$ at GeV's [37]. Nevertheless only a few pulsars, among which Vela, Crab and Geminga, have been detected in γ-rays [38], and the nature of the majority of Galactic γ-ray sources is still unknown.

Gamma rays streaming from the centre of our galaxy could be the signature of elusive Dark Matter. The dark matter is expected to constitute a significant fraction of the mass of the Universe. Among the favoured dark matter candidates are weakly interactive massive particles (WIMPs), whose existence follows from supersymmetric models: the conservation of R parity in supersymmetric theories requires that the lighest supersymmetric particle (LSP) is stable. Most of the models predict that LSP is the lighest neutralino (χ^0), an electrically neutral particle resulting from the superposition of the neutral gauge (bino, B^0 and wino, W_3^0) and Higgs boson superpartners (H_1^0, H_2^0).

The neutralino has appropriate annihilation cross section and mass to provide suitable relic density. The current accelerator limit $m_\chi \gtrsim 50\,\mathrm{GeV}$ [39] suggests that the LSP is heavy. The chemical freeze-out determines the amount of neutralinos today and occurs when the annihilation rate of neutralinos drops below the Hubble rate, $\Gamma_{ann}/H < 1$. Soon after the neutralinos become non relativistic and a relic cosmological abundance remains, the rate for neutralino annihilation,

$\Gamma_{ann} = \langle \sigma_{ann} v \rangle n_\chi$, being suppressed by the Boltzmann factor in the number density of the neutralinos, $n_\chi \sim (m_\chi T)^{3/2} e^{(-m_\chi/T)}$. The freeze-out temperature of neutralino, given by $\Gamma_{ann}(T_f) = H(T_f)$, turns out to be $T_f \simeq m > \chi/20$ [30] well below m_χ. The neutralinos thus behave as cold dark matter by the time of matter dominance and structure formation.

A number of methods have been proposed to search for evidence of such particles. These include direct searches for scattering off a nucleons in the detector, indirect searches to detect the annihilation products, and collider experiments [40]. The indirect searches include antiprotons and positrons in cosmic rays, γ-rays from the Galactic center and halo (diffuse emission), and neutrinos from massive bodies like Glactic center, the sun and the earth.

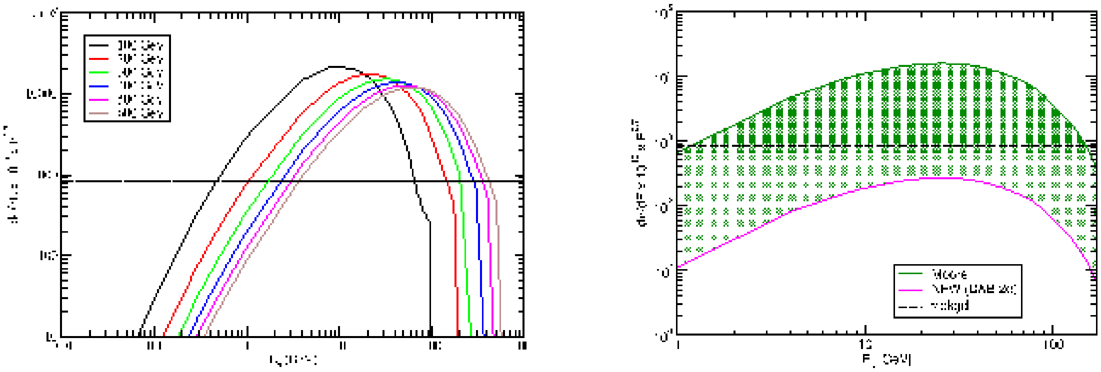

(a) (b)

Figure 1.9: Continuum γ-spectrum from neutralino annihilation: (a) for different neutralino masses using a More dark matter halo profile; (b) for different dark matter halo profiles with $m_\chi = 200\,\mathrm{GeV}$. In both figures the spectrum is computed using the AMS-02 detector characteristics, integrating the signal coming from the Glactic center in $\Delta\Omega = 10^{-3}\,\mathrm{sr}$ for 3 years.

In the γ-rays channel, the signal could be a relatively narrow line with energy far beyond that of ordinary particles, or a broad feature. The former results from direct annihilation $\chi\chi \to \gamma\gamma$ and $\chi\chi \to Z\gamma$ producing monoenergetic photons with energy $E_\gamma = m_\chi$ and $E_\gamma = m_\chi(1 - m_Z^2/4m_\chi^2)$ rispectively. The continuum contribution, instead, is mainly due to the decay of π^0 mesons produced in quark jets from neutralino annihilations. In contrast to the 'smoking gun' signature arising from the line processes, the continuum spectrum lacks distinctive features, but produces a larger number of photons [41]. The γ-ray flux from neutralino annihilation can be written as:

$$F_\gamma(\xi) = \frac{N_\gamma \langle \sigma_{ann} v \rangle}{4\pi m_\chi^2} \int_{line-of-sight} \rho_\chi^2(l) dl(\xi) \, \mathrm{cm}^{-2} \, \mathrm{s}^{-1} \, \mathrm{sr}^{-1} \tag{1.7}$$

where ξ is the angle between the direction of the Galactic center and the line-of-sight, ρ_χ is the halo dark matter density at distance l along the line of sight, N_γ is the number of photons created per annihilation. According to this equation the detection probability of a gamma ray signal, either continuous or line, will depend sensitively on the density profile of the dark matter halo. Recent N-body simulations for dark matter halos have given indications of a universal profile, where the density increases substantially near the galactic center [42]. This would be the best region to search for the signature of relic WIMPs.

The present goal of astroparticle physics experiments and measurements is to develop a model consistent either with cosmic ray data and with diffuse *gamma*-ray data, *or* to clearly indicate the reason for the discrepancy. The new detailed spectra and skymaps of Galactic diffuse γ-rays emission by GLAST [43] and AMS-02 experiment in the GeV to TeV energy range, complemented by the accurate measurements of cosmic-ray nuclei, protons, antiprotons, electrons and positrons of the AMS-02 mission, will change the “status quo” dramatically. In its turn, a detailed cosmic ray propagation model will provide a reliable basis for other studies such as (i) search for dark matter signals in cosmic rays and diffuse γ-rays, (ii) spectrum and origin of the extragalactic γ-ray emission, (iii) theories of nucleosynthesis and evolution of elements.

Chapter 2

The AMS-02 experiment

AMS-02 is an astroparticle experiment designed for a very precise measurement of primary cosmic rays spectrum operating on board of the ISS at a 400 km altitude for a period of about 3 years. Because this is the major scientific experiment on the ISS, NASA is following the progress of AMS with detailed reviews concerning the design and construction, safety and ground operation to ensure the detector can be launched in April 2008.

2.1 Scientific goals of the experiment

In recent years several space borne experiments have been proposed to measure, with growing accuracy, the composition of primary high energy cosmic rays [44]. The AMS-02 experiment will cover the energy window $1\,\mathrm{GeV} \div 1\,\mathrm{TeV}$, a region that is interesting for various physical processes and which is today very poorly known; AMS-02 will be able to identify charged cosmic rays with an accuracy up to 1 part in 10^9 as well as high energy gamma rays.

The main scientific goals of the AMS-02 experiment are:

Antimatter search

The Standard Model cannot generate the asymmetry between matter and antimatter we observe in the Universe today [45]. Either the asymmetry is due to physics beyond the Standard Model, or there are undetected domains of antimatter in the Universe. The gamma-ray observations set an upper limit of 10^{-5} on the fraction of antimatter in the local galaxy cluster, leading to the conclusion that matter and antimatter must be separated on a scale greater than about 10 Mpc [46]. This limit was recently improved [47], leading to the conclusion that the nearest part of the

Universe dominated by antimatter should be at least at Gpc distance scale. Despite these bounds, an existence of astronomically large objects of antimatter (gas clouds, anti-stars, anti-galaxies,...) is not only possible but quite natural in many scenarios of baryogenesis. They may be as close as halo of the Galaxy and rich of anti-nuclei.

An unambiguous proof of existence of cosmic antimatter would be observation of anti-nuclei in cosmic rays. The probability of production of anti-nuclei in high energy hadronic interaction of CR with the interstellar medium quickly vanishes with increasing atomic number. While for antiprotons the secondary production probability is at the level of 10^{-4}, for $\overline{\mathrm{D}}$ is at the level of 10^{-8} or less and for $^4\overline{\mathrm{He}}$ is well below 10^{-12}. An observation even of a single $^4\overline{\mathrm{He}}$-nuclei or a heavier one would demostrate that primordial antimatter indeed exists not too far from us.

During the last 35 years, experiments on balloons have pushed the limit on the $^4\overline{\mathrm{He}}/^4\mathrm{He}$ flux ratio to the level of less than about one part in a million. AMS-02 is expected to improve the current sensitivity by three orders of magnitude, reaching rigidities of the order of a TV (see Fig. 2.1 (a)).

Dark Matter search

A good dark matter candidate in the Cold Dark Matter scenario is the neutralino (χ). Rare cosmic ray components such as high energy $\overline{\mathrm{p}}$, e^+ and γ have been suggested as potential indirect signatures for cold DM [40]. The annihilation of the exotic χ would produce deviations from the smooth energy spectra of rare CRs that have, however, to be detectable against several sources of background due to the primary CR spectrum. AMS-02 will produce a very accurate study of the $\overline{\mathrm{p}}$, e^+, γ spectra (for a review on dark matter detection in the positron and γ channel with AMS-02, see [48] [49] [50]).

High energy cosmic rays physics

The measurements of cosmic rays particles fluxes are of fundamental importance because the search of any signal of new physics would have such fluxes as a background.

AMS-02 will allow to test the propagation models by means of high statistic fluxes measurements of individual elements up to $\mathrm{Z} \sim 26$ in the energy range from $\sim 1\,\mathrm{GV}$ to $\sim 1\,\mathrm{TV}$. Precise measurements of fluxes of H, He and CR species which are believed to have a primary origin (CNO) in a wide energy range, can be related to the injection spectra and can constrain the primary acceleration mechanisms of CR. The fluxes of secondaries and, their ratio with the parent primaries (D/p, $^3\mathrm{He}/^4\mathrm{He}$, B/C, sub-Fe/Fe), define the amount of material traversed by the CR since their acceleration. Finally, the ratio of unstable to stable secondary nuclei, as ^{10}Be/^{9}Be, can be used to determine the cosmic ray confinement time in the galaxy and, in diffusion models, the effective thickness of the galactic halo.

The expected sensitivity to the B/C and the ^{10}Be/^{9}Be ratios, respectively after 6 months and one year of data taking, is shown in Fig. 2.1 (c), (d).

Gamma rays physics

In addition to charged particles, the physics scope of AMS-02 is greatly broadened by the measurement of gamma rays.

The Universe is largely transparent to gamma rays in the energy range of AMS; moreover gamma rays point back to their sources, unlike high-energy cosmic rays, which are deflected by magnetic fields. Thanks to these characteristics, gamma rays are ideal to provide a direct view into nature's highest-energy acceleration processes.

2.2 Detector layout

A high accurancy measurement of spectra of energetic particles requires minimal material in the particle trajectory so that the material itself is not a source of background nor a source of large angle nuclear scattering. Furthermore to ensure that background particles be not confused with the signal, redundant measurements of momentum, energy, velocity and charge are required. AMS-02 design strictly follows these two principles.

The detector must also fulfill the requirements imposed by its operation in space over several years. Every subsystem conforms to NASA specifications (concerning weight, resistance to load and vibrations) and is able to operate in vacuum over a very wide temperature range. The detector electronics withstands the highly ionizing enviroment, guarantees redundancy against failures and ensures very low power consumption.

Fig. 2.2 shows the AMS-02 detector configuration. The main components are:

- TRD, which distinguishes electrons and positrons from hadrons at 0.1 % level.
- TOF, which measures the time of flight with 120 ps accuracy.
- Superconducting Magnet with a bending power $BL^2 = 0.86\,\mathrm{Tm}^2$.

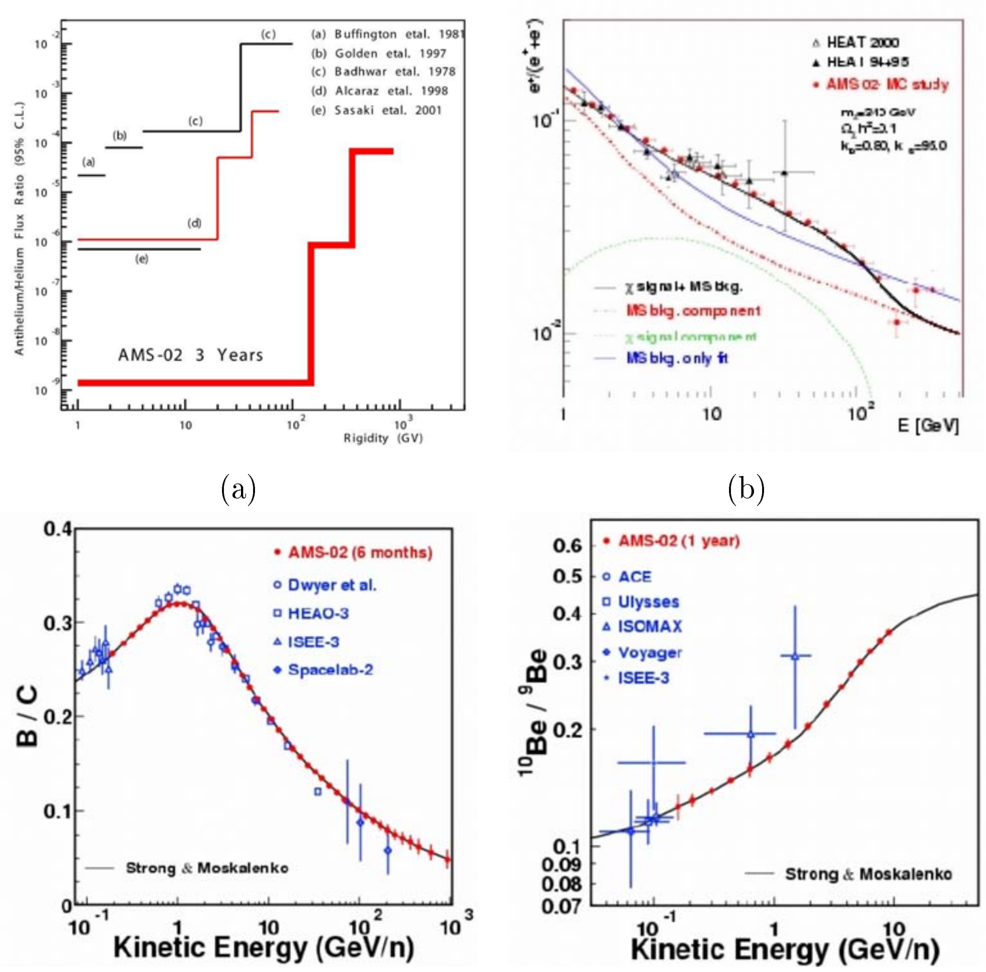

(a) (b)

(c) (d)

Figure 2.1: Projected AMS-02 measurements. Compilation of limits on the antimatter-to-matter flux ratio (a). Detection of a primary component in the e^+ spectrum produced by annihilanting neutralinos (b). Sensitivity to the B/C and the ^{10}Be/^{9}Be ratio (c,d).

- Silicon Tracker (STD), wich provides a proton rigidity resolution of 20 % at 500 GeV and a charge resolution of nuclei up to $Z = 26$.

- ACC, which ensures that only particles passing through the magnet aperture be accepted.

- RICH, which measures the charge and the velocity (to 0.1 % level) of particles and nuclei.

- ECAL, which identifies electrons, positrons and gamma rays against hadrons and measures their energy at few percent level.

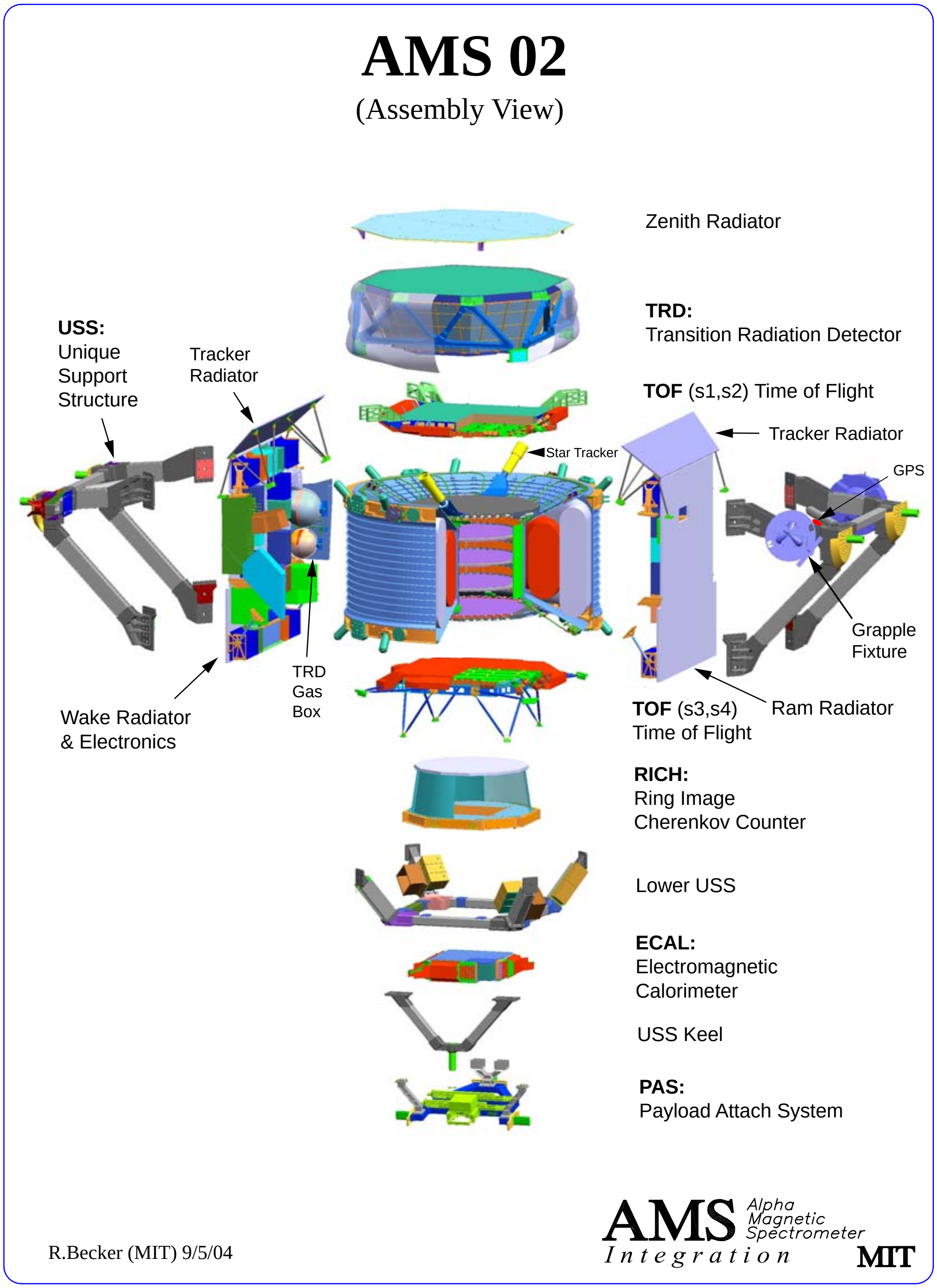

Figure 2.2: The AMS-02 detector layout.

In addition, to correlate the sources of gamma rays with the detected signal, the AMS attitude is determined, with an accuracy of a few arc seconds, by the AMICA (Astro Mapper for Instrument Check of Attitude) Star Tracker (AST). AST consists of a pair of small optical telescopes mounted on each side of the upper Silicon Tracker, acquiring the images of the stars and comparing them with an on-board astromeric star catalogue. Finally a Global Positioning System (GPS) is deployed on AMS-02 to provide timing information with a reference time accuracy of few microseconds.

All the AMS-02 subdetectors are attached to the Unique Support Structure (USS2), the mechanical frame designed to connect AMS-02 to the Shuttle and to the ISS.

2.2.1 Transition Radiation Detector (TRD)

A charged particle traversing the Transition Radiation Detector (TRD) produces a characteristic electromagnetic radiation, depending on its mass and energy. Once known the particle momentum, the detected transition radiation can be used to distinguish between particles of different masses.

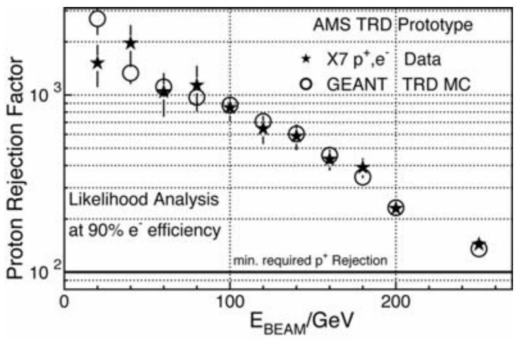

Figure 2.3: AMS-02 TRD proton rejection factor. Prototype performances requiring an electron efficiency of 90 %.

The TRD detector [51] is composed by 328 modules arranged in 20 layers supported by a pyramidal aluminum-honeycomb octagon. The lower and upper four layers are oriented parallel to the magnetic field, while the middle 12 layers run perpendicularly to provide three-dimensional tracking. Each module contains 16 straw tubes, with lenghts ranging from 0.8 to 2 m, and filled with a Xe : Co$_2$ (80 % : 20 %) gas mixture. The tubes operate at 1600 V. Above the straw tubes a 20 mm thick fleece is used as a radiator. With its multilayer structure the fleece enhances the probability up to the 50 % for a traversing particle to emit a photon. Electronic and gas supply system with the Xe and Co$_2$ storage vessels complete the TRD system.

The thermal stability and the gas tightness of the straw modules are the most critical design issues. The former is essential for the performance of the detector as temperature variations change the gas density and hence the gas gain in the straw tubes. The full cover in multi-layer-insulation (MLI) will keep the spatial and temporal orbit gradient below 1 °C, corresponding to a gain variation of few percent. Regarding gas tightness, since the available supplies of gas will have to last for three years of operation, the leak rate from the straw tubes must be carefully reduced. The design forsees a double layer kapton-aluminum foil for the walls and of two special polycarbonate endpieces at the ends. Besides, selecting one by one each module, a mean operating time of about 20 years ("safety factor" of 7.9) was reached.

A full 20 layers prototype were built to verify the performances of the TRD. Fig. 2.3 shows the capability to separate electrons in a proton background. By means of a likelihood algorithm and requiring an electron efficiency of 90 %, the background rejection factor is well above 100 for proton beam energies between 15 and 250 GeV.

2.2.2 Time of Flight (TOF)

The Time of Flight scintillators [52] provide the fast trigger for charged particle, the measurement of the particle velocity including the discrimination between upward and downward going particles and a measurement of the absolute charge which complements those made in the silicon tracker and in the RICH.

The TOF system is composed of four roughly circular planes of plastic scintillator paddles with a sensitive area of $1.2\,\mathrm{m}^2$ each. One pair of planes is placed above the superconducting magnet and one pair below. In a plane, the paddles, 12 cm wide and 1 cm thick, are overlapped by 0.5 cm to avoid geometrical inefficiencies. Between the two adjacent planes, the paddles are perpendicular for background rejection and to aid the offline analysis. This geometry allows a granularity of about $12 \times 12\,\mathrm{cm}^2$ for trigger purposes with an efficiency of $\sim 100\,\%$.

The scintillation light, driven by means of plexiglas light guides, is collected by two or three photomultipliers from each end of a paddle. To stand the 1-3 kG field produced by the magnet in the TOF zone, "fine mesh" PMT's (Hamamatsu R5946) enclosed in magnetic shields are employed. The best performances from the photomultipliers are obtained when their axis is aligned within 45 degrees along the field direction. The light guides are tilted and bent to assure this allignment. Moreover the signals from the PMT's connected to the same end of a paddle are combined with a linear adder for good redundancy and photo-statistics enhancement.

With a weight less than 280 Kg and a power consumption less than 170 W, the

TOF system provides a time resolution of about 130 ps for a minimum ionizing particle, while the energy loss by a charged particle is measured with a resolution sufficient to distinguish nuclei up to charge $Z \sim 20$.

2.2.3 Superconducting Magnet

In comparison to permanent magnets, the superconducting magnet allows to achieve a higher bending power ($BL^2 = 0.86\,\mathrm{Tm}^2$), and thus to extend the range of measurements of particles and nuclei to the multi- TeV region [54].

The magnet design follows NASA safety standards, including negligible dipole moment (to avoid forces on the ISS due to interaction with the geomagnetic field) and a stray field smaller than 300 G at 2 m distance from the center of the magnet (to not interfere with life support system of the astronauts).

The whole magnet system consists of superconducting coils, a superfluid helium vessel and a cryogenic system, all enclosed in a vacuum tank. The vacuum tank is toroidal with 1.1 m inner diameter, 2.7 m outer diameter; the length of the central cylinder surrounding the tracker is 0.9 m. Outside of the vacuum tank there are the supporting electronics, valves and cabling (see Fig. 2.4 (a))

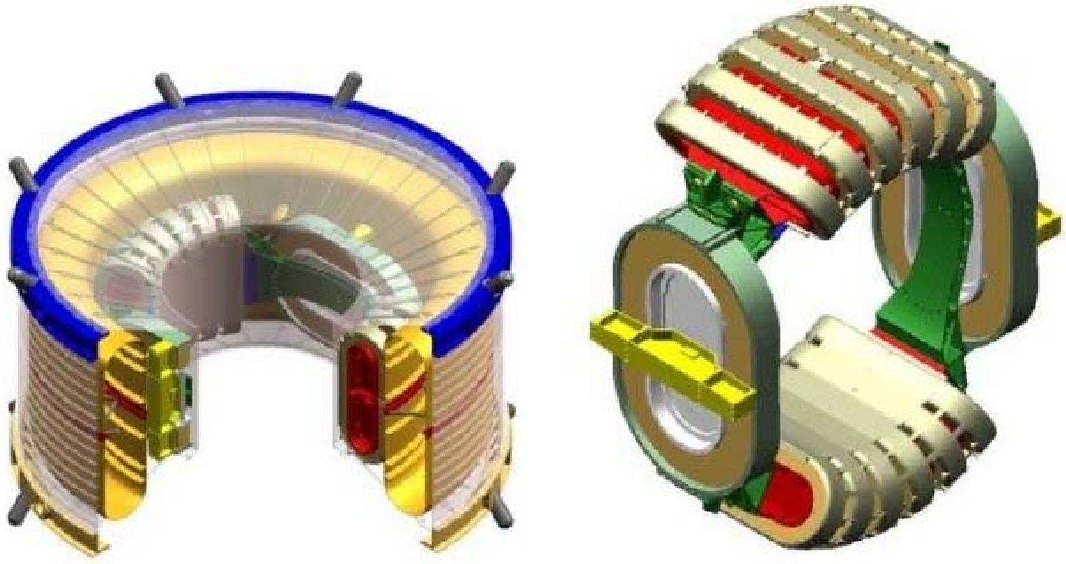

(a) (b)

Figure 2.4: Superconducting magnet layout. (a) The vacuum tank containing the superconducting coils, the superfluid helium vessel and the cryogenic system. (b) The 14 coils arrangement.

The coil system consists of a set of 14 superconducting coils arranged as shown in Fig. 2.4 (b), around the inner cylinder of the vacuum tank. A single large pair of Helmholtz coils generates the magnetic dipole field perpendicular to the experiment axis (with a central magnetic field of 0.86 T). The other twelve smaller flux coils control the stray field and contribute to the useful dipole field. All the coils are wound from the same superconducting wire specifically developed to meet the AMS magnet requirements. The current is carried by tiny filaments of niobium titanium (NbTi), embedded in copper matrix. The copper is encased in a rectangular cross section high-purity aluminum sheath wich is extremely conductive, thus providing thermal stability at minimum weight. According to test results, compared to other materials, this conductor reduces the quench probability by a factor of 2000.

The magnet operates at a temperature of 1.8 K, cooled by superfluid helium stored in the vessel. It is launched at operating temperature, with the vessel full of 2500 litres of superfluid helium (more than 2000 kg). The magnet will be launched with no field and will be charged only after installation on ISS. Because of parasitic heat loads, the helium will gradually boil away throughout the lifetime of the experiment. In order to ensure the 3 year endurance very carefull studies were done in the project to minimize the heat loss to $\leq 100\,\mathrm{mW}$.

2.2.4 Silicon Tracker (STD)

In AMS-02, the tracking information is provided by a tracker detector made of $\sim 6.4\,\mathrm{m}^2$ of silicon sensors [55]. The realization of such a large-scale detector requires to employ sensors with a larger surface and higher inter-strip capacitances in comparison with that used for vertex detectors in colliding-beam experiments. As a consequence, the major challenges were to maintain the required mechanical precision and low-noise performance. In the AMS-02 silicon tracker, charged particle tracks are traced by 8 space points in a $\sim 1\,\mathrm{m}^3$ sized magnetic field: each point is determined with an accuracy better than $10\,\mu\mathrm{m}$.

The silicon tracker is composed of $41.360 \times 72.045 \times 0.300\,\mathrm{mm}^3$ double-sided silicon micro-strip sensors. The sensor design uses capacitive charge coupling with implantation (readout) strip pitches of 27.5 (110) μm for the p-side (or s-side) and 104 (208) μm for the n-side (k-side). The finer pitch p-side strips are used to measure the bending coordinate because they give the best position resolution.

For readout and biasing, the silicon sensors are grouped together in ladders of different lenghts to match the cylindrical geometry of the AMS-02 magnet. A metalized Upilex film, glued directly to the silicon sensors, serves as routing cable to bring the n-side signals to the n-side front end hybrid, which is located at the ladder end closest to the magnet wall. The flexible Upilex film and a second short Upilex film joining the p-side strips to their hybrid allow the ladders to be placed back-to-back. A doubly-metalized Upilex film surround each ladder to ensure an electromagnetic shield.

The ladders are installed in 8 layers, on 5 planes of an ultra-light support structure. These support planes are obtained surrounding a low density honeycomb slab with two carbon fiber layers. A number of ladders ranging from 20 to 24 are necessary to form each of the three detection planes lying inside the magnet. 30 ladders are necessary to compose the two layers external to the magnet. The STD mechanical support structure is divided into three sections: a carbon fiber cylindrical shell supporting the three planes inside the magnet, and two carbon fiber flanges supporting the external planes. The internal planes are equipped on both sides with silicon ladders for a total of 8 sampling planes.

The hybrids are mounted on Thermal Pyrolytic Graphite-Al cooling bars, which evacuate the heat generated by the front-end electronics. The presence of the superconducting magnet requires an active cooling system for the tracker. The system consists in a two-phase mechanically pumped loop, where a cooling liquid (CO_2) enters in the tracker at a temperature just below the boiling point, starts evaporating due to the heat and finally condenses again when traversing two radiator panels facing deep space.

The alignment system provides optically generated signals in the 8 layers of the silicon tracker that mimic straight tracks. These artificial straight tracks allow a position alignment better than $5\,\mu$m. This procedure will be active during data taking to correct any possible change in tracker geometry due to rapid thermal deformation or to long term displacements.

A measurement of the position resolution was provided by a dedicated setup consisting of a reference telescope (composed of four single-sided silicon sensors with $50\,\mu$m pitch readout) and an AMS-02 ladder. The detectors were placed in front of a 120 GeV muon beam. Fig. 2.5 shows the residual position distribution of the ladder: the fit is obtained using a Gaussian function plus a flat background. The widths of the Gaussian are 8.5 and $30\,\mu$m for the p- and the n-side respectively.

2.2.5 Anticoincidence counters (ACC)

The Anticoincidence counters (ACC) detect particles which enter the tracker laterally. Those particles may confuse the charge determination by producing background

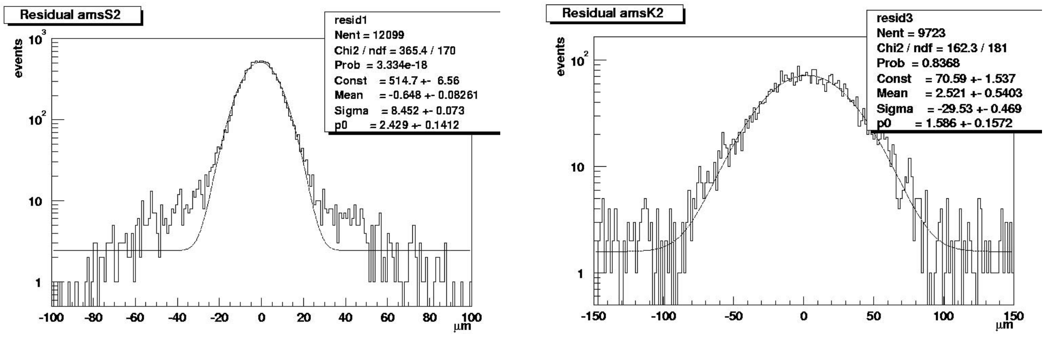

(a) (b)

Figure 2.5: AMS-02 Tracker position resolution in bending (a) and in non-bending (b) direction.

hits.

Sixteen scintillating panels 8 mm thick form the ACC. They fit tightly inside the inner bore of the superconducting magnet and surround the STD. The light from each scintillator is firsty collected by wavelength shifter fibers (embedded in the scintillator) and then routed up to two PMT's (Hamamatsu R5946), one mounted on the bottom and one on the top rim of the vacuum case. Both the PMTs have axis parallel to the stray field.

Signals from the ACC are included in the level 1 trigger of AMS-02 to minimize background events.

2.2.6 Ring Imaging Čerenkov Detector (RICH)

When a relativistic particle with charge Ze passes through a dielectric material with refractive index $n(\omega)$, a cone of Čerenkov radiation is created along its trajectory. The half opening angle of the cone is $cos\theta_C = 1/\beta n(\omega)$ and the number of radiated photons in a frequency range $d\omega$ for a traversed thickness dx of the material is $d^2N/(d\omega\, dx) = \alpha Z^2 sin^2\theta_C$, where $\alpha = (370\hbar c)\,\mathrm{eV}^{-1}\mathrm{cm}^{-1}$. Therefore the velocity of the particle can be determined from measurement of the opening angle, while the number of detected photons provides an estimation of the charge.

The Ring Imaging Čerenkov Detector (RICH) [56] has a truncated conical shape with 60 cm upper radius, 67 cm lower radius and a height of 47 cm. The lower base is fully covered by an array of 680 PMT's, with the exception of a $64 \times 64\,\mathrm{cm}^2$ square central hole to let particles go unaffected to the ECAL. On the top of the RICH, a supporting plate holds a 3 cm thick radiator consisting in 80 rectangular blocks of silica Aereogels and 16 central blocks of NaF, which give a wider cone for particles that fall upon the central hole of the detection plane. Photons, emerging from the radiator and pointing outside the detection array, are redirected to the lower plate by the lateral surface of the RICH which is covered by a reflector.

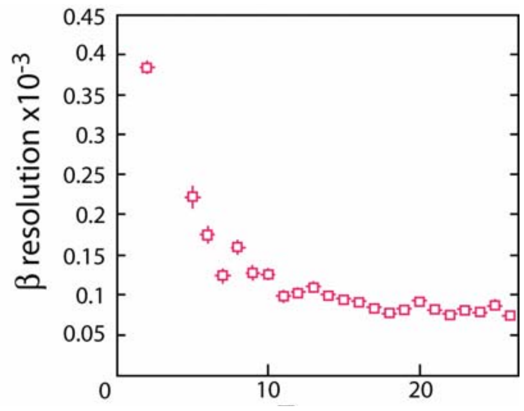

Figure 2.6: AMS-02 RICH measured β resolution as a function of the charge of the particle.

The accuracy in the measurement of the velocity dependes significantly on the size of the photon sensors. The Hamamatsu R7600-00-M16 photomultipliers have a multianodic structure 4×4 pixels, each one with a sensitive area of $4{\times}4\,\mathrm{mm}^2$. Each PMT is protected by a shielding against a 300 G residual magnetic field and is equipped with 16 independent light guides. The PMT fine granularity guarantees a resolution in the measurement of the velocity of 1 per mil. In Fig. 2.6 the dependence of the resolution on the velocity as a function of the particle charge of the particle is shown: data were collected using a RICH prototype in front of a proton beam with rigidities between 5 and 13 GV and an ion beam (A/Z = 2) with a rigidity of 40 GV.

2.2.7 Electromagnetic Calorimeter (ECAL)

The Electromagnetic Calorimeter (ECAL) of the AMS-02 experiment is a fine grained lead-scintillanting fiber sampling calorimeter, that allow precise, 3-dimensional imaging of the longitudinal and lateral shower development, providing high e/h discrimination and good energy resolution. The calorimeter also provides a “stand alone” photon trigger capability to AMS-02.

The ECAL system will be extensively described in the next chapter.

2.3 Charged particles detection strategies

The AMS-02 trigger recognizes charged particles passing through the apparatus thanks to the coincidence of fast signals from the TOF scintillators. Fast trigger, required for precise timing measurement in TOF [58], and Level 1 trigger are generated by a logic combination of TOF, ACC and ECAL responses. Once the event is accepted, the DAQ process starts and data from detectors recorded.

2.3.1 Fast and Level 1 (LV1) trigger logic

In the scintillator front-end time board ($SFET2$), the pulse coming out from one side of a TOF scintillator paddle is compared to three different thresholds, labeled as "low-threshold" (LT), "high-threshold" (HT, about $\sim 0.4\,$MIP) and "superhigh-threshold" (SHT, $\sim 3.5\,$MIP). While the LT digital output is used to start the time measurements, a logic combination of the HT and the SHT outputs generate three types of signals for each TOF plane: the "charged particle" (CP) signal by the OR of the HT of all counter sides, the "central charge particle" (CT) signal by the OR of the HT of the central counter sides, and the "particle with big charge" (BZ) signal by the OR of the SHT of all counter sides. The CP and CT signals from each TOF plane are fed into lookup tables (LUT's) to generate the "$Z \geq 1$ charged particle" fast trigger, FTC. The BZ signals are instead combined by an AND gate or an OR gate to generate the "$Z > 2$ charged particle" fast trigger, FTZ [57].

The fast trigger is both sent to the TOF TDC's and used in LV1 trigger logic (see Fig. 2.7). After the fast trigger, a 240 ns gate is opened to latch signals from TOF, ACC and ECAL. The CP, CT, BZ outputs of each TOF plane are fed into lookup tables to produce the signals $FTCP0$, $FTCP1$, $FTCT0$, $FTCT1$, *LUT-BZ*. The latched ACC signals are used to count number of fired ACC counters. This number is compared with two adjustable thresholds to produce the $ACC0$ and $ACC1$ signals. Latched ECAL Fast signals (defined in Sec. 5.4), combined by an AND gate or OR gate, are used to generate $ECAL - F_{and}$ and $ECAL - F_{or}$. All these signals are sent to a LV1 subtrigger unit, where they are enabled or disabled by a mask, and then combined by an AND gate. The LV1 trigger decision corresponds to the logic OR of the output signals of 8 LV1 subtrigger units.

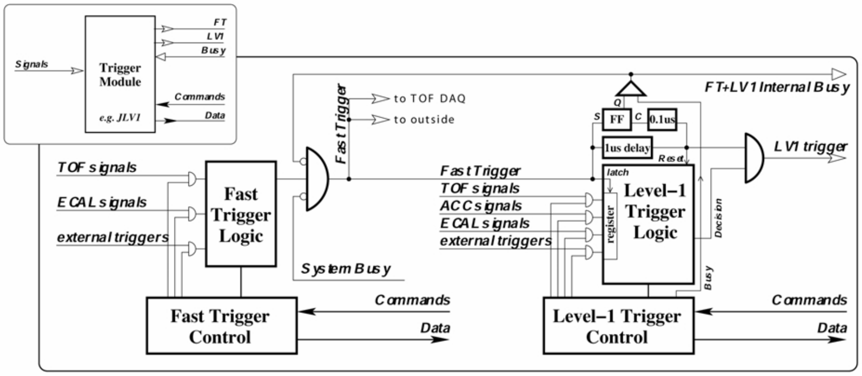

Figure 2.7: AMS-02 Fast and Level 1 trigger scheme.

The AMS-02 trigger scheme allows very high flexibility thanks to masks and lookup tables. An example of an implementable trigger logic is summarized in Tab. 2.1. FCT is generated when at least one scintillator paddle is hitted in 3 TOF planes out of 4. When the geomagnetic latitude θ_{Mag} of the orbit > 0.7, the $ACC0$ signal (with threshold set to zero) is used to guarantee that the detected particle is inside the tracker acceptance. When θ_{Mag} decreases and consequently increases the energy of the CR, one hit in ACC ($ACC1$) is allowed to recover efficency. With heavy ions the expected rate is much smaller than with the protons: therefore an ACC flag is not necessary to reject events and the *LUT-BZ* flag is used. For electrons or positrons, the fast signal from ECAL gives a powerful solution to avoid backsplash phenomena (more detail in Sec. 5.9).

Trigger	**Primary Targets**
FTC & $ACC0$ if $\theta_{Mag} > 0.7$	p, $\overline{\text{p}}$, He
FTC & $ACC1$ if $\theta_{Mag} < 0.7$	High energy p, $\overline{\text{p}}$, He
FTC & $(LUT - BZ)$	He, Heavy Ions
FTC & $(ECAL - F_{and})$	$\text{e}^{\pm}$

Table 2.1: "Charged particle" LV1 trigger logic. Each row is implemented in a LV1 subtrigge unit and combined with the others by an OR gate. θ_{Mag} is the geomagnetic latitude at which particles are detected.

The total LV1 trigger rate is estimated to vary from 200 and 2000 Hz, depending on the geomagnetic latitude. The electronics system is being consevatively designed to perform precision physics at twice these rates.

2.3.2 Particle identification and spectrum measurement

A charged cosmic ray is univocally identified by measuring its charge, velocity and rigidity. The rigidity is defined as:

$$R = \frac{pc}{ze} = \gamma\,\beta\,\frac{m_0 c^2}{ze} \tag{2.1}$$

thus by knowing the particle momentum p, its charge ze and the particle velocity $v = \beta\, c$, it is possible to infer the particle rest mass m_0, so ensuring its identification.

The particle velocity is measured both by TOF and RICH subdetectors. The TOF measures the time of flight (t) of the particle along the path $l = L/cos\theta$ where L is the distance between the upper and lower TOF planes and θ is the trajectory colatitude angle. β is obtained from the relation:

$$\beta = \frac{L}{tc\ cos\theta} \tag{2.2}$$

with an uncertainity

$$\sigma_\beta^2 \simeq \frac{L^2}{c^2}\frac{\sigma_t^2}{t^4 cos^2\theta} \tag{2.3}$$

where the time resolution σ_t is of the order of 0.1 ns. This resolution corresponds to a $\Delta\beta/\beta \approx 0.5\%$ allowing particle velocity to be measured up to $\beta \approx 0.95$. Moreover, upward and downward going particles are distinguished by the TOF system at the level of 1 failure over 10^9. Also the RICH can determine β with an accuracy of $\Delta\beta/\beta \approx 0.1\%$, so enhancing the sensitivity to light element's isotopes.

The particle rigidity is measured by the tracker. The trajectory of a particle with rigidity R and charge ze, traversing a uniform magnetic field B, is a helix with curvature ρ:

$$\rho = \frac{B}{R\ sen\theta} \tag{2.4}$$

where θ is the pitch angle between the particle momentum and the magnetic field. If σ_y is the spatial resolution of the tracking system in the bending plane, N is the number of position samplings and s_{mag} is the magnetic field strength along the particle trajectory $\int \boldsymbol{B} \cdot \boldsymbol{dl}$, the relative uncertainty on the rigidity is approximized as []:

$$\frac{\Delta R}{R} \propto \frac{R\sigma_y}{s_{mag}}\frac{1}{\sqrt{N+4}} \tag{2.5}$$

An estimate of the AMS-02 rigidity resolution for proton and helium is presented in Fig. 2.8 (a). Position resolutions of 30 and 10 μm were used for the x and y coordinates and the silicon detection efficiency was supposed to be 90 %. The maximum detectable rigidity (MDR) is usually defined as the rigidity for which the measurement uncertainity is 100 %. In AMS-02 the MDR will be above 1 TV.

The absolute value of a particle charge of a particle, $|z|$, is obtained by measuring its energy deposition in "active" materials. According to the Bethe-Bloch formula, the mean energy lost over a distance dx by a particle, other than electrons, is:

$$-\frac{dE}{dx} = K\frac{Z}{A}\frac{z^2}{\beta^2}[\frac{1}{2}\ln\frac{2m_ec^2(\beta\gamma)^2T_{max}}{\langle I\rangle^2} - \beta^2 - \frac{\delta}{2}] \tag{2.6}$$

where $K = 0.307075\,\text{MeV}\,\text{cm}^2$, $\langle I\rangle^2$ is the mean ionization energy of the medium, δ is a "density effect" correction and T_{max} is the maximum kinetic energy which can be provided to a free electron in a single collision. Eq. 2.6 can be used to derive $|z|$, once the particle velocity β is known. In AMS-02 this is possible in TOF and

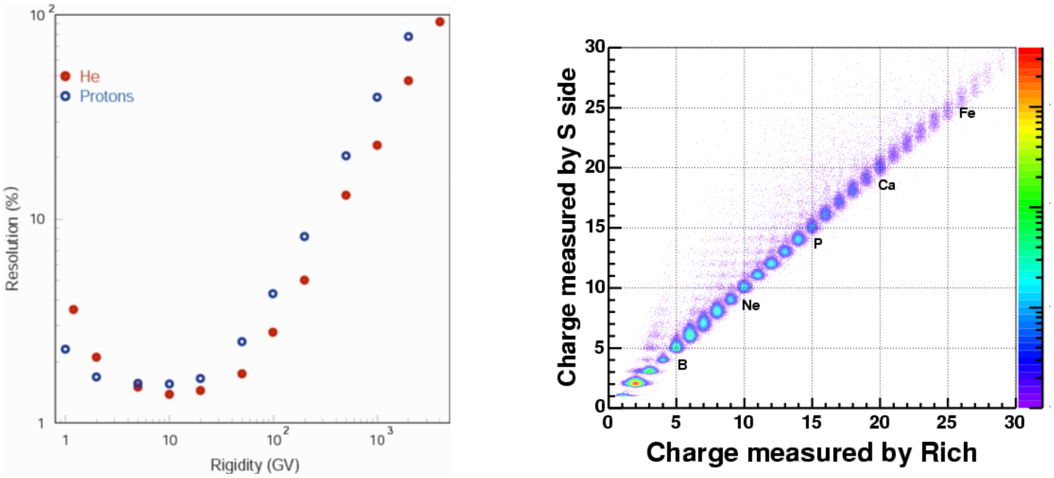

(a) (b)

Figure 2.8: Estimated rigidity resolution for protons (blue) and He nuclei (red) with the AMS-02 silicon tracker (a). Correlation plot between particle charge measurements in tracker and RICH (b).

Tracker planes. Since Čerenkov light depends on z^2 (see Sec. 2.2.6), also RICH can be used to measure charge. Altogether elements with $Z < 26$ will be identified up to an energy per nucleon E/n $\sim$ 1 TeV, while element's isotopes will be distinguished up to $A < 25$ with E/n $\sim$ 15 GeV.

The charge sign is found by looking at the track curvature once the upward or downward direction is determined by TOF. When the particle rigidity is comparable with the MDR, the wrong deflection sign may be attributed to the trajectory ("spillover"). Below the MDR the accurancy in the measurement of the charge sign is expected to be $\sim 10^{-10}$, both for $\overline{\mathrm{p}}/\,\mathrm{p}$ and $\mathrm{e}^+/\,\mathrm{e}^-$.

To identify low abundance particles, like positrons and antiprotons, the previously discussed techniques aren't effective. The background generated by protons (same charge as positrons) and by electrons (same charge of antiprotons) have a much higher flux than the signal. To solve the problem, both TRD and ECAL will be employed to distinguish between hadrons and leptons (e/h discrimination). The TRD will provide a discrimination power of the order of 10^{-2}-10^{-3} up to 100 GeV, while in ECAL hadrons will be rejected with a power of 10^{-4}-10^{-5}, using as discriminating tools the shower shape and the matching between the energy deposit and the momentum measured by the Tracker. With the combined use of TRD and ECAL, an e/h discrimination of 10^{-6} is forseen in the range few GeV to 1 TeV [59].

Chapter 3

The AMS-02 Electromagnetic calorimeter

The AMS 02 calorimeter was designed to measure the total energy released by $e^{\pm}$ and γ-rays of cosmic origin in the range between 1 GeV and 1 TeV approximately. The main requirements for ECAL are a good linearity and energy resolution, while its 3D imaging capability is needed to provide additional particle tracking. Moreover, in order to perform accurate measurements of $e^{\pm}$ and γ spectra, a key issue is a high capability to suppress the CR background, mainly consisting of p and He nuclei.

In this chapter the ECAL characteristics along with the results of beam test on a full-scale prototype are presented.

3.1 ECAL design overview

In ECAL active volume, a particle passing through scintillanting fibers produces light which is collected by photomultipliers installed all around. The active volume

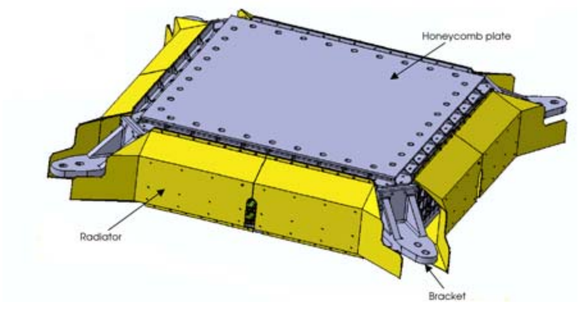

Figure 3.1: The AMS-02 electromagnetic calorimeter.

is contained in a mechanical support frame which hold the light collection system in position and connect the detector to the lower part of the USS2.

The two main constraints in the project were the limits on weight (638 kg) and on power consumption (100 W).

In 2001 an ECAL full scale prototype was assembled and then submitted to space qualification and beam tests with results in full agreements with the MC simulations. Based on the experience gained in the construction of the prototype, the ECAL flight model assembling started in November 2004 with the integration of the active volume into the mechanical support frame.

3.1.1 Active volume

The AMS 02 electromagnetic calorimeter is a sampling device built employing a lead-scintillanting fibers composite material. This structure, which was developed to increase the X_0/λ ratio respect to other concurrent materials, is characterized by a lead-fiber-glue volumes ratio of 1:0.57:0.15 cm^3, an average density of 6.8 ± 0.3 g/cm^3 and a radiation length of about 10 mm.

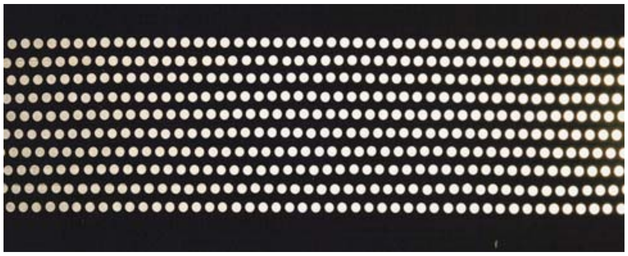

Figure 3.2: The cross section of the ECAL lead-fiber-glue composite structure.

The active volume results as the pile up of 9 “superlayers”. Each superlayer, designed as a square parallelepiped with 65.8 cm side and 1.85 cm thickness, consists of 11 grooved lead foils, 1 mm thick, interleaved with 10 layers of 1 mm diameter scintillanting fibers glued by means of Bicron BC-600 optical cement (Fig. 3.2 and Fig. 3.3 (a)). At the end of the manufacturing process, the whole calorimeter has a total weight of 487 kg and a thickness of 16.6 cm corresponding to almost 17 radiation lengths.

To improve the rejection power it’s extremely useful to image the longitudinal and the lateral development of the electromagnetic and hadronic showers. The 3D shower reconstruction and the fine granularity allow the detector a very good imaging capability. In ECAL the former is obtained by alterning superlayers with fibers along the X axis to superlayers with fibers along the Y axis (see Fig. 3.3 (b)). The calorimeter has 4 superlayers in the X view and 5 in the Y view (bending plane of the spectrometer magnetic field).

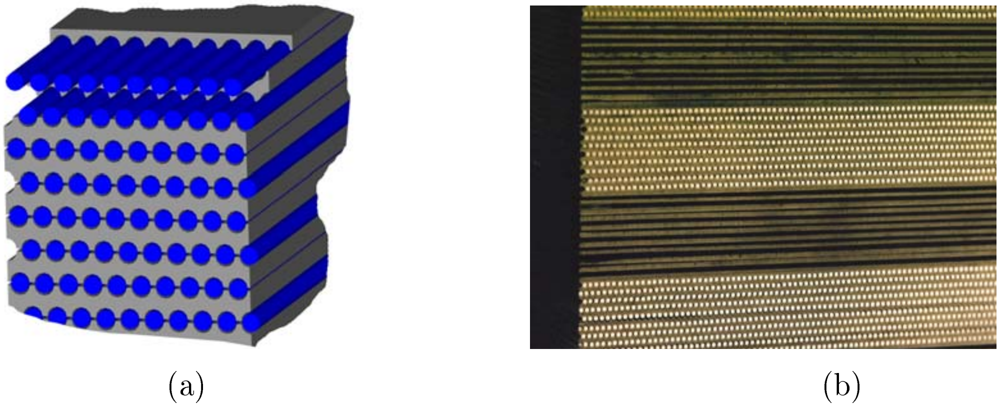
(a) (b)

Figure 3.3: ECAL active volume. (a) Scketch of the superlayer structure. (b) Assembling of the superlayers with fibers running along orthogonal directions.

Each readout element, called a "cell", is individuated as a square area of 9 mm side covering about 35 fibers; it roughly corresponds to a Moliere radius in transverse dimensions and one radiation length in depth. With this configuration each superlayer can be seen as build up by two 9 mm thick layers. The total number of cells is 1296 allowing the signal to be sampled 18 times in depth (10 in Y and 8 in X direction).

3.1.2 Mechanical assembly and thermal control

The ECAL mechanical assembly supports the active volume, the light collection system and related electronics. It is designed in order to minimize the weight with the first resonance frequency above 50 Hz, to withstand accelerations up to 14 g in any direction and to have thermal characteristics limiting the temperature gradient in the detector.

The optimization of the mechanical project through finite element analysis led to an alluminium alloy support frame, composed of a top and a bottom honeycomb plates, four lateral panels lodging the light collection system, and four brackets for connections to the main AMS-02 supporting structure (USS2). According to the space qualification test results, the structure has a first resonance frequency above 60 Hz in front of only 67 kg total weight.

The thermal requirements, mainly chosen to guarantee a good PMT gain stability, foresee that the operating temperature shall be in the range −20 °C to +40 °C and that the temperature shall change less than 5 °C over one orbit. According to simulations, four radiators displaced around the lateral panels of the detector and a multi layer insulation (MLI), covering of bottom/top plates and brackets, will ensure a non-operating time shorter than 5 % of one year mission.Moreover, during the flight, a complete set of sensors will allow an on-line monitoring of the detector's temperature.

3.1.3 Light collection system

The multianodes Hamamatsu R7600-00-M4 were preferred above many other similar photomultipliers considering the behaviour in magnetic field and the dimension of the anodes. Each photomultiplier accomodates four anodes with a light collecting area of $8.9 \times 8.9\,\mathrm{mm}^2$ which very well fits the ECAL granularity. In the meanwhile the light spectrum of the scintillanting fibers Pol.hi.tech. polifi 0244-100, used in the active volume, is well contained in the sensitivity range of the catode.

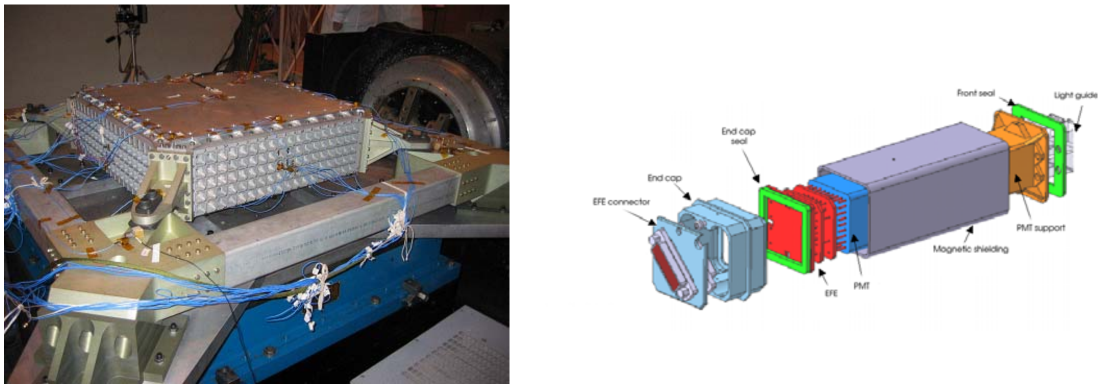

(a) (b)

Figure 3.4: (a) Space qualification tests of the detector. (b) Exploded view of a light collection unit: each unit is lodged in one of the holes of the lateral pannels showed in (a). Light guides, PMT and FE card fit inside the square section magnetic shielding. On the back, the "End-cap" assure the light tightness and solid connection to the ECAL support frame.

In designing the light collection system, the tight limits on power consumption and weight illustrated before, imposed a limit on the maximum number of usable PMT's. For this reason one end only of the fibers is read. Thus each superlayer is equipped with 36 photomultipliers alternatively arranged on the two opposite sides in order not to create mechanical interference. The coupling between fibers and PMT's is realized by means of plexiglass light guides which maximize light yield and reduce cross-talk between pixel. The light guides are shaped as a truncated pyramid and inserted inside a polycarbonate support tube; two trasparent silicone joints positioned on both light guides ends assure a very good optical contact even when high mechanical stresses are applied.

In the calorimeter region, at a distance of about 140 cm from the center of the the superconductive magnet, the intensity of the residual magnetic field rises up to 200 − 300 Gauss. The studies of the PMT's sensitivity to magnetic field [60] clearly evidenced the necessity of a shield able to keep the intensity below 20 Gauss. According to FEA simulations which take in account also the reciprocal interferences due to neighbor PMT's shieldings, the best shielding is achieved with 1 mm thick soft iron tubes, shaped as square parallelepiped with 30.5 mm side and 100 mm length. This shielding also acts as mechanical support frame for the entire light collection system which, along with the bleeder and the FE card, constitutes a very compact and easly replaceable structure (see Fig 3.4 (b)).

3.1.4 Electronic support system

The most challenging issues in designing the electronic system were to assure a very high reliability, while containing the power consumption and the weight.

Except for the front end, each electronics board is composed of two completely independent sectors (the "hot" and the "cold" sectors), separately powered but capable of the same functionality. In case of any fault it is possible to switch from one sector to the other, while maintaining full functionality of the ECAL.

Commercial off-the-shelf components were widely used in order to reduce costs and use state-of-the-art devices. According to space rules, proper testing for total dose and single events effects, were performed. Qualification models of the crates and of all the electronics boards were produced to undergo vibration, thermal vacuum and electro-magnetic interference (EMI) tests.

The total power consumption is limited to less than 90 W, the weight, considering also the light collection system, to 125 kg.

Front end (FE) electronics

Three electronics cards with square cross-section, embedded in a potting compound to avoid sparks at low air pressure, are attached to the rear part of each photomultiplier. The bleeder is implemented on the first two cards, while the third accommodates the front end electronics.

The high dynamic range, requested to the calorimeter, imposes severe constraints both on the PMT's divider choice and on the FE electronics design. According to measurements, the light emission due to 1 MIP traversing a cell corresponds to about 8 photoelectrons (p.e.). To detect the MIP signal above read out electronics noise, this imposes to set the working point of the photomultipliers at a gain of about 10^5. On the other hand the Monte Carlo simulations state that the maximum energy deposit in one cell by 1 TeV electrons is $\sim$ 55000 p.e. corrisponding to about 7000 MIP's. With the previous gain, PMTs and front-end electronics must be able to handle input charge up to 900 pC.

The performances of many PMT's bases were tested to reach a reduction of the power consumption preserving the response linearity over the widest dynamic range. Among several different divider ratios, a particoular tapered one (1.5 : 1.5 : 1.5 : 1 : 1 : 1 : 1 : 1 : 1 : 1 : 2 : 3.6) is able to reduce the power consumption down to 100 mW (at the standard working point of 650 V) limiting the linearity deviation to 30 % for light pulse of about 55000 p.e. (see Fig. 3.5 (a)).

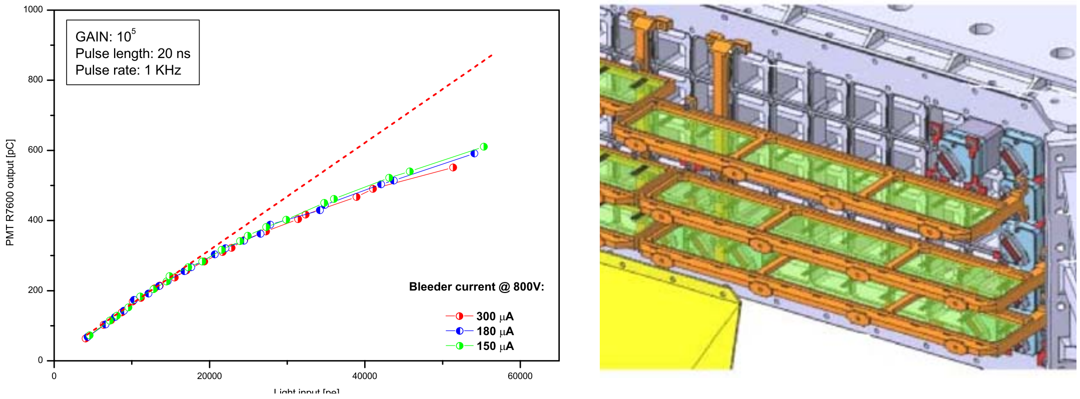

(a) (b)

Figure 3.5: (a) The PMT linearity plot. the three curves are obtained with bleeders with same HV distribution ratio but different current. (b) Lateral view of the calorimeter, when the radiator, in yellow, is removed: each EIB (green) collects data from 9 PMT's (light blue) fitted inside the back+lateral panel frame.

The FE card contains the "sample and hold" electronics and the digitization systems. Choosing to set a 1 MIP signal equivalent to 5 LSB's of the ADC, the corresponding dynamic range of 3.4 10^4 would require 16 bits ADC's. A dedicated ASIC chip with a very low power consumption (21 mW) was thought to employ standard 12 bit ADC's. Each of the four signals of the photomultiplier is shaped, sent to two parallel amplification stages with different gain (with a gain ratio of about 33) and then digitalized: the low gain output is used when the other, more sensitive and precise, is saturated. Together with the 8 signals coming from the PMT's anodes, an analog and a digital signal of the last dynode are also provided: the former is used to build up the ECAL "stand alone" trigger.

The digitized outputs from 9 PMT's are sent to an intermediate board (EIB) mounted on the ECAL mechanical support frame and then to the EDR2 (see below). The EIB, besides lodging the analog part of the γ-rays trigger, regulates the low voltages to the 9 front end electronics and distributes the pulse sequence from the EDR2 to drive ASIC chips and ADC's.

DAQ system

The EDR2 card is the node of DAQ closest to the front end. The EDR2 receives the digitized signals from 27 PMT's (3 EIB's) over Low Voltage Differential Signaling (LVDS) lines, subtracts pedestals, suppresses zeros and send the results through a Backplane to the next node in the DAQ chain, the JINF. The EDR2 also acts as a bridge for the front end electronics power and as control of the EIB, using single ended TTL signaling. Six EDR2 and one JINF are mounted in each of the two crates located at opposite corners of the detector on the arms of the USS2.

Slow control ans high/low voltage supply

The main functions of the Slow Control System are to supervise the switching between the two redundant sections of each board and to set and monitor the high voltages. The primary slow control interface is located on the JINF card, which provides 8 serial buses (using the LeCroy protocol), distributed to the HV control modules and to the low voltage control cards (EPSFE). The EPSFE was designed to host the power switches for the front end electronis. Each group of 9 front ends (1 EIB) is powered through one of this switches, so that in case of a major failure a single section can be isolated from the full system. Three EPSFE plus one trigger board (ETRG) complete the set of boards placed in each ECAL crate.

Located in a dedicated box (ERPD), 6 DC-DC converters supply the low voltages (+3.8, -2.8, +3.3 and +5.6 V) and the filtered +28 V to the hot or cold sides of the boards, as controlled by the power coming from two highly reliable switches of the Power Distribution System (PDS).

The high voltage system consists of 6 HV Brick (EHV), each one made up of 1 controller, 2 elevator and 5 linear regulator modules (LR) for a total of 40 regulated channels supplying 55 PMT's. The controller module contains the digital to analog converters needed to regulate the system and all the slow control functions. The elevator is based on a 4 stage Cockcroft-Walton multiplier, which raises the input 28 V to a high voltage in the range 500 to 1000 V. Each linear regulator provides a selection of the high voltage with a 2 V accuracy, through a discrete "series transistor". Each linear regulator powers one or two PMT's. The power dissipation has been kept below 3 W per Brick by maintaining the efficiency at more than 90 %.

3.2 The detector performances

The beam test of July 2002 at Cern SPS (following to the ones with a reduced scale prototype in 2000 [61] and in 2001 [62]) provided very useful informations in defining the equalization and the calibration procedure, so to be able to correct the calorimeter answer owing to dead channels, rear and lateral leakages; this is an essential task in space, where the calorimenter is continuously subjected to the action of many external factors (temperature variation, vibrations, ionizing radiations, etc.).

The detector performances were measured on the full scale prototype using muons, protons and antiprotons beams at 120 GeV and electrons with energy ranging from 3 to 180 GeV. The calorimeter was not completely instrumented: only 63 over 324 photomultipliers were installed, covering the full depth of a squared area with 126 mm side. The PMT's were equipped with the real FE electronics and were powered by a prototype of the HV supply system.

3.2.1 Read out channels equalization

For each cell i, raw data are offline corrected according to the following expression:

$$A_i^{corr}(x_c) = A_i^{raw}(x_i) \cdot \frac{\mathrm{L(x_c)}}{\mathrm{L(x_i)}} \cdot C_i^{\mathrm{PMT}} \cdot C_i^{\mathrm{FEE}} \tag{3.1}$$

where $L(x)$ is the mean light attenuation function of the fibers computed respectively for the coordinate x_i of the energy deposit and for the coordinate x_c of the ECAL center, C_i^{PMT} corrects for differences in the light conversion efficiency among the cells and C_i^{FEE} selects the high or the low gain FE outputs according to the signal's magnitude.

After correction, the response of the cells may be seen as equivalent to the one expected with the beam impinging in the central point (x_c, y_c) of the calorimeter entrance face.

Light attenuation function ($L(x)$)

The light attenuation curve was measured by a fine scan along the fibers' length, using a 120 GeV electron beam. The average signal of each single cell was fitted as a function of the distance between the beam impact point and the photomultiplier cathode. Considering the combination of two exponential functions with small (λ_s) and long (λ_l) attenuation lengths, the mean attenuation curve resulted to be:

$$L(x) = A(0)\,(f\,e^{-\frac{x}{\lambda_s}} + (1-f)\,e^{-\frac{x}{\lambda_l}}) \tag{3.2}$$

with $\lambda_s = 130\,\mathrm{mm}$, $\lambda_l = 2200\,\mathrm{mm}$ and $f = 0.19$.

Correction for the light conversion efficency (C^{PMT})

The changes in the light conversion efficiency among cells are mainly due to the differences in the coupling between fibers and photomultipliers, in the PMTs' gain, in the responses of the four pixels of each PMT. The factors C_i^{PMT} correct these effects for each cell i.

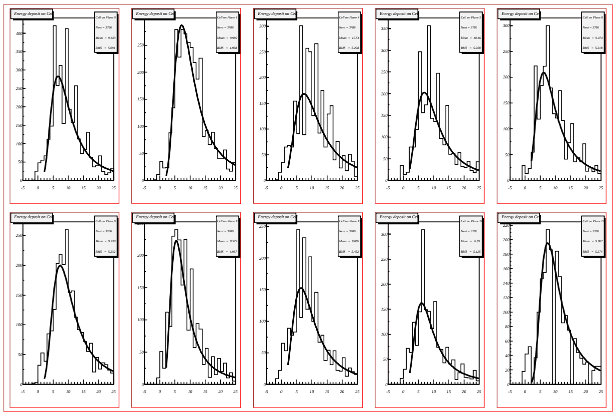

Figure 3.6: MIP's energy distribution in some ECAL cells. The distribution are fitted by a Landau function.

Two methods were applied to estimate the best value of the correction factors. One equalizes the MIP's signal, as MIP's release the same amount of energy in each cell of the calorimeter (Fig. 3.6). The other method, already developed for 2001 test beam, relies on the characteristics of the longitudinal profile of the e.m. showers. Selecting only electron events, distributed on the whole instrumented area, first the cells of each layer are interequalized, then the layers intercalibration is obtained using a fitting procedure with a gamma function as a function of the beam energy [49].

The last method provides better results in terms of detector linearity and of response uniformity as a function of the beam impinging point.

Selection of the FE outputs (C^{FEE})

As explained in Par. 3.1.4, the ASIC chip mounted on the front end card splits the output of each cell in two signals of low and high gain. The high to low ratio was estimated by plotting for each cell the high vs. the low gain output (A_i^{high} vs. A_i^{low}). The plot in Fig. 3.7 evidenciates an undesired dependency of the Hi/Lo ratio from the signal's amplitude. The reasons of this problem was found in a erroneus setting in the low voltage supply system of the ASIC chip.

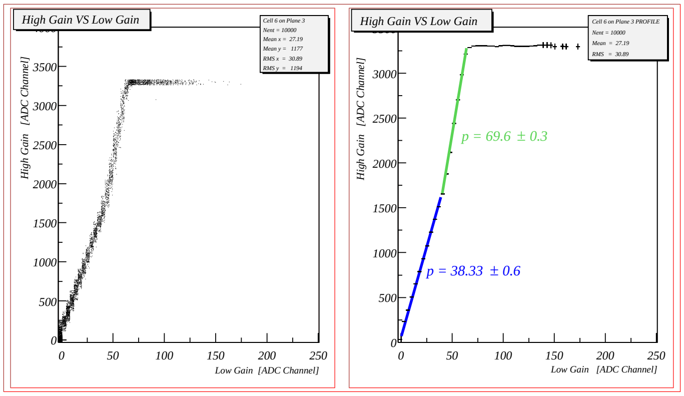

Figure 3.7: HIgh vs low gain output in a cell; the two slopes are fitted separately.

Fitting the two slopes R_i' and R_i'' for each cell i, the function C_i^{FEE} was defined as:

$$C_i^{\mathrm{FEE}} = \begin{cases} 1/R_i' & \text{if } A_i^{low} < 50 \\ 1/R_i'' & \text{if } 50 \leq A_i^{low} < 100 \\ 1 & \text{if } A_i^{low} \geq 100 \end{cases} \tag{3.3}$$

3.2.2 Measurement of the effective sampling thickness

An electromagnetic shower shape well scales longitudinally with the radiation length X_0 of the medium. The mean longitudinal profile of the energy deposition if the shower is well described by a gamma distribution [?]:

$$\frac{dE}{dt} = E_0 \frac{\mathrm{b}^{(\alpha+1)}}{\Gamma(\alpha+1)} t^{\alpha} e^{-}\mathrm{b}t \tag{3.4}$$

where $t = \frac{x}{X_0}$ is the longitudinal depth in X_0 units, E_0 is the energy of the incident particle, and $b \sim 0.5$ with a weak dependence on Z. The maximum of the showers occurs at $t_{max} = \alpha/\mathrm{b}$ and can be expressed as a function of E_0:

$$t_{max} = \frac{\alpha}{b} = log(E_0/E_c) + C_j \qquad C_j = e, \gamma \tag{3.5}$$

where $C_e = -0.5$ for electron-induced cascades and $C_\gamma = +0.5$ for photon-induced cascades.

In beam test data, the integrated longitudinal profiles of the e.m. showers were fitted using the expression of Eq. 3.4 with t replaced by $x = t \cdot \mathrm{X}_0$. The maximum of the showers occurs at $x_{max} = \alpha/\mathrm{b} \cdot \mathrm{X}_0$, hence the dependency form energy beam is expressed by the relation:

$$x_{max} = \mathrm{X}_0 \cdot \mathrm{log}E(GeV) + const \tag{3.6}$$

Fitting with this expression the x_{max} values as a function of the beam energy, a measurement of the radiation length (X_0) was extracted. A value of $\mathrm{X}_0 = (9.94 \pm 0.17)$ mm was found, implying an ECAL total thickness of about $16.7\,\mathrm{X}_0$'s.

3.2.3 Lateral and rear leakage corrections

According to Eq. 3.4, for electrons beams below 10 GeV the rear leakage is almost negligible (less than 2 %). Thus these data were used to determine the calibration constant of the calorimeter. At higher energies the rear leakage becomes important and a correction to the measured energy is needed.

The simpliest and effective correction relies on the hypothesis that the quantity of energy not contained in the rear part of ECAL depends linearly on the fraction $E_{layer18}/E_{TOT}$, i.e. on the energy deposited in the last layer with respect to the total one:

$$E^C_{TOT} - E_{TOT} = \alpha \frac{E_{layer18}}{E_{TOT}} \tag{3.7}$$

where E^C_{TOT} is the corrected total energy and the parameter α is estimated fitting the profile plot $\frac{E_{TOT}}{E_{Beam}}$ vs. $\frac{E_{layer18}}{E_{TOT}}$ (see Fig. 3.8 (a)).

Fig. 3.8 (b) shows the improvements in the energy linearity after rear leakage correction. Good linearity is obtained up to 20 GeV while above 30 GeV there is a costant 5 % missing energy which increases starting above 150 GeV. This problem, problably linked to some missing corrections in the equalization procedure (lateral leakage, PMT's or FE cards non linearity, etc.) will be better studied in future beam tests.

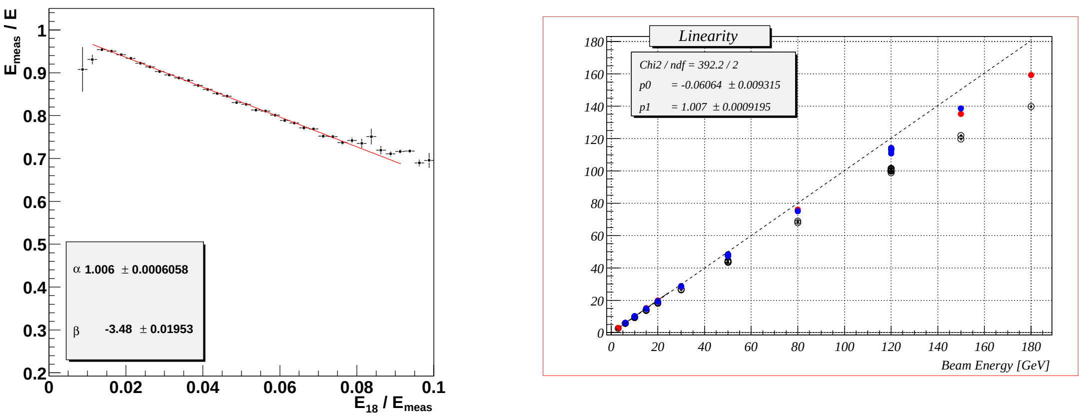

(a) (b)

Figure 3.8: Rear leakage correction. (a) Profile plot of $\frac{E_{TOT}}{E_{Beam}}$ vs. $\frac{E_{layer18}}{E_{TOT}}$ for electrons at 120 GeV. (b) Energy linearity curve after leakage correction. The open circles are for the total energy deposit in the calorimeter without the leakage correction. The filled circles are corrected for leakage with the "last plane" method; the red ones are for runs with beam impact points in the middle of the instrumented part of the ECAL, the blue ones are for runs with different impact points.

A preliminary analysis of the lateral leakage effect is reported in [63]. According to Monte Carlo simulations the developped method allows to recover energy which leaks from ECAL in the peripheral region up to the area close to the last cell's edge. The corrections are almost energy independent and can be applied as multiplicative factors different for each layer of the detector:

$$C_{layer}(x, E^{meas}_{layer}) = \frac{p0 + \frac{p1}{p2^2}}{p0 + \frac{p1}{(x-p2)^2}} \tag{3.8}$$

where the parameters p0, p1 and p2 are obtained fitting the energy deposit in the layer E^{meas}_{layer} as a function of the distance x of the particle from the detector center. In particular p0 estimates the average energy deposited in the layer if there is no transeverse leakage, while p2 is a asymptotic line of the fitted function and gives information about the geometrical active area. The absolute values of p2 are higher for low energies which means that the ECAL active area is larger for low energies.

In Fig. 3.9 (a) the energy resolution for 120 GeV electrons as a function of the distance from the last pixel edge is presented. The method allows to recover the resolution even in the distance 1.5-3 mm from the last pixel edge ($x_{edge} = -32.4$ cm) corresponding to about 99 % of the geometrical active area. In spite of this, applying the corrections to beam test data, only small part of energy resolution is recovered (see Fig. 3.9 (b)). This effect is mainly due to the poor knowledge of the particle's impact position, which is known with a precision of one pixel: indeed within the last pixel the correction coefficients change by even 50 % between the external and internal edge.

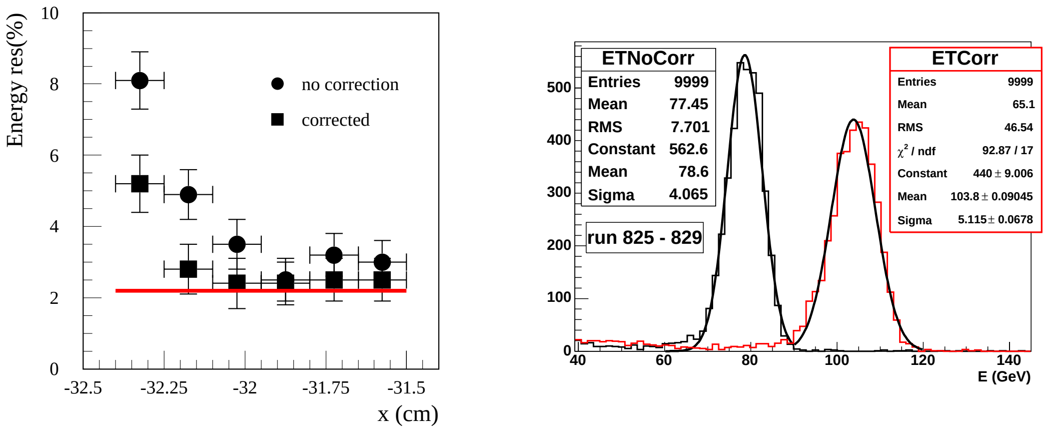

(a) (b)

Figure 3.9: Lateral leakage recovery. (a) Energy resolution as a functon of position within the last pixel for 120 GeV MC simulated electrons. Squares represent corrected measurements while red line corresponds to energy resolution as measured in beam test. (b) Energy distribution for 120 GeV electrons from beam test data, with and without leakage correction (no real leakage correction applied).

3.2.4 Energy and Angular resolution

The calorimeter energy resolution is shown in Fig. 3.10 (a), where the fractional uncertainty on the energy measurment $\sigma(E)/E$ is plotted as a function of the nominal beam energy:

$$\frac{\sigma(E)}{E} = \frac{(10.2 \pm 0.3)\,\%}{\sqrt{E[GeV]}} \oplus (2.3 \pm 0.1)\,\% \tag{3.9}$$

The angular resolution at a fixed energy is studied by using electrons impinging on ECAL at normal incidence. For each event the shower axis is calculated by means of standard center of gravity methods. The angular resolution $\sigma_{68\,\%}$ is defined by the angular distance between the reconstructed θ angle and the beam incidence angle that contains 68 % of the events(see Fig. 3.11 (a)). The dependency of the angular

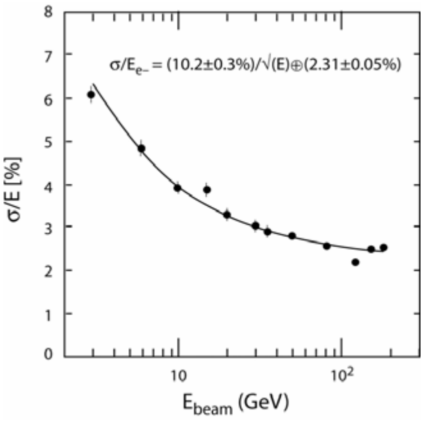

Figure 3.10: Resolution.

resolution from beam energy resulted to be:

$$\Delta\sigma_{68\,\%}(E) = \frac{8.6 \pm 0.1}{\sqrt{E[GeV]}} \oplus (0.57 \pm 0.4) \quad \text{(in degrees)} \tag{3.10}$$

The angular resolution was also measured at fixed energy as a function of the incidence angle of the e^- beam on the ECAL surface (see Fig. 3.11 (b)). The improvement seen is due to the larger number of radiation lenghts traversed by a tilted shower crossing ECAL with respect to a normal one.

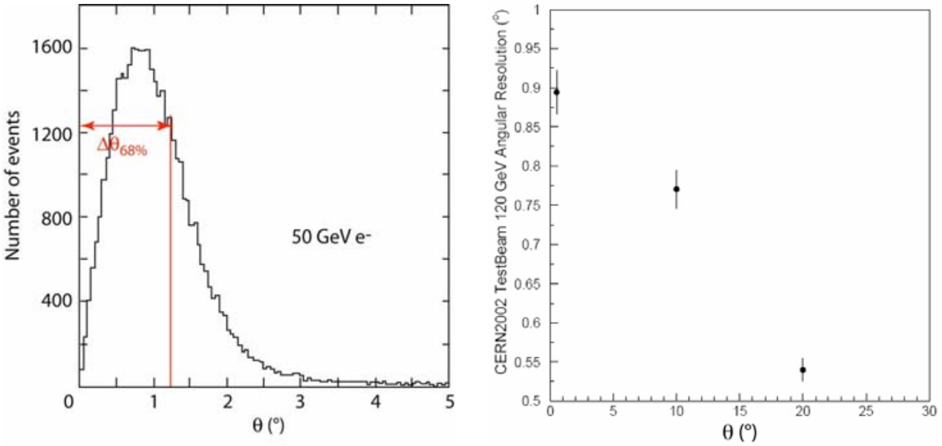

(a) (b)

Figure 3.11: Angular resolution. (a) Distribution of residuals between the reconstructed θ angle and the beam incidence angle for 50 GeV electrons. (b) Angular resolution for 120 GeV electrons as a function of the beam incidence angle.

Chapter 4

Gamma rays detection with AMS-02

To detect photons in the AMS-02 experiment two complementary methods were explored. The first method is the *conversion mode*. It consists in the identification and reconstruction of $e^+ e^-$ pairs from γ conversions happened somewhere in the material upstream of the first silicon tracker layer. The second method, which is main argument of the present work, is the *single photon mode*: it is based on the direct detection of photons in the electromagnetic calorimeter.

4.1 Specifications of a gamma ray detector

The performances of a gamma ray detector are primarily related to its geometric dimensions, to the field-of-view (FOV), and to the capability to identify photons from other background events.

The number of detected photons of a certain energy can be expressed, in a general way, as:

$$N^{\gamma}(E) = \int \frac{d\Phi(E,S,\Omega,t)}{dE dS d\Omega dt} \varepsilon(E,S,\Omega,t) d\Omega \boldsymbol{u} \cdot d\boldsymbol{S} dt \tag{4.1}$$

where $\Phi(E,S,\Omega,t)$ is the integral gamma flux in general function of energy E, solid angle Ω, surface S and time t; $\varepsilon(E,S,\Omega,t)$ is the detector efficiency; $d\Omega = sin\theta \, d\theta \, d\phi$ is the differential solid angle; $\boldsymbol{u} \cdot d\boldsymbol{S}$ is the dot product of the differential area and the gamma incidence direction unit vector.

Assuming the efficiency and the flux both time-indipendent, the Eq. 4.1 can be rewritten as:

$$N^{\gamma}(E) = T_{obs} \cdot \int \frac{d\Phi(E,S,\Omega)}{dE dS d\Omega} \varepsilon(E,S,\Omega) d\Omega \boldsymbol{u} \cdot d\boldsymbol{S} \tag{4.2}$$

where T_{obs} is the time of observation of the source of photons. Starting from Eq. 4.2, the two main figures of merit of a gamma rays telescope are defined as follows:

Dynamic acceptance. It is a measure of the geometrical acceptance to incoming gamma rays, modulated by the efficiency which in general depends on the energy and incidence angle. Assuming the flux is isotropic and homogeneous, it depends only on the energy, so:

$$N^{\gamma}(E) = T_{obs}\frac{d\Phi(E)}{dE}\int \varepsilon(E,S,\Omega)d\Omega\boldsymbol{u}\cdot d\boldsymbol{S} \tag{4.3}$$

where the integral over the whole field of view and the surface is defined as the detector's dynamic acceptance at energy E, measured in $m^2 sr$.

$$Acc(E) = \int \varepsilon(E,S,\Omega)d\Omega\boldsymbol{u}\cdot d\boldsymbol{S} \tag{4.4}$$

This magnitude, together with the exposure time, sets the limit of the sensitivity achievable by any γ-rays experiment.

Effective area. It is defined as the derivative of the dynamic acceptance with respect to the solid angle at a certain energy and incident direction.

$$A_{eff}(E,\Omega) = \int \varepsilon(E,S,\Omega,t)d\boldsymbol{u}\cdot d\boldsymbol{S} \tag{4.5}$$

The effective area allows us to evaluate the dependence of the acceptance at a certain energy on fixed directions measured from the detector axis, i.e. it is a measure of the projected area of the instrument. It is measured in m^2.

Direct detection of charged cosmic rays or detection of products of the interactions between CR and the experiment itself are the main sources of background in space enviroment.

Let $\Phi_s(P,S,\Omega,t)$ be the i-th particle specie flux as a function of momentum P, solid angle Ω, surface S and time t; the total number of background events collected during an exposition time T_{obs} is:

$$N_{bkg}(P) = \sum_i \int \frac{d\Phi_i(P,S,\Omega,t)}{dPdSd\Omega dt}\eta_i(P,S,\Omega,t)d\Omega\boldsymbol{u}\cdot d\boldsymbol{S}dt \tag{4.6}$$

summed over species index i. In Eq. 4.6, $\eta_i(P,S,\Omega,t)$ is called the background contamination and describes the detector's capability in discriminating gamma rays from incoming particles of the i-th specie. For protons, the particles with highest abundancy, the flux can be assumed isotropic and time indipendent. Thus, the number of proton events misinterpreted as photons becomes:

$$N^p_{bkg}(P) = T_{obs}\frac{d\Phi_p(P)}{dP}\int \eta_p(P,S,\Omega)d\Omega\boldsymbol{u}\cdot d\boldsymbol{S} \tag{4.7}$$

In an electromagnetic calorimeter like ECAL, the energy deposit of a proton is usually not much related to its initial momentum. Among several reasons, there can happen very large event-to-event fluctuations in the visible energy fraction of the hadronic shower or the production of highly penetrating particles like μ or ν from pions' decay that may escape the calorimeter carrying away energy. From an analytical point of view, we can assume that the probability for a proton to release an energy E is governed by a detector-dependent distribution, $\mathcal{F}_p(P,S,\Omega,E)$, that is function of the proton momentum, of the trajectory direction and of the impact point. Using this notation, the number of events resulted as background to photons with reconstructed energy E, will be:

$$N^p_{bkg}(E) = T_{obs}\int \frac{d\Phi_p(P)}{dP}\cdot\Big(\int \mathcal{F}_p(P,S,\Omega,E)\eta_p(P,S,\Omega)d\Omega\boldsymbol{u}\cdot d\boldsymbol{S}\Big)dP \tag{4.8}$$

The performances of the detector about background rejection issue are described by another foundamental parameter:

Rejection power. It is defined as follows:

$$R(E) = \frac{Acc^{\gamma}(E)}{Acc^{p}(E)} \tag{4.9}$$

where:

$$Acc^p(E) = Acc_{geo}\frac{\int \frac{d\Phi_p(P)}{dP}\int \mathcal{F}_p(P,S,\Omega,E)\eta_p(P,S,\Omega)d\Omega\boldsymbol{u}\cdot d\boldsymbol{S}dP}{\int \frac{d\Phi_p(P)}{dP}\int \mathcal{F}_p(P,S,\Omega,E)d\Omega\boldsymbol{u}\cdot d\boldsymbol{S}dP} \tag{4.10}$$

In describing the detector's specifications, it's often introduced a global rejection power (R) that doesn't depend on energy; by integrating over the whole accessible energy range:

$$R = \frac{\int N^{\gamma}(E)dE}{\int N^{\gamma}(E,\varepsilon(E)=1)dE}\Big/\frac{\int N^p_{bkg}(E)dE}{\int N^p_{bkg}(E,\eta_p(E)=1)dE} \tag{4.11}$$

where $\int N^{\gamma}(E,\varepsilon(E)=1)dE$ is the total number of γ-rays that would be collected with an ideal efficency of 100 % and $\int N^p_{bkg}(E,\eta_p(E)=1)dE$ are the background events before any signal identification procedure is applied.

Let us consider an ideal situation in which the proton energy deposit in the detector is related only to its momentum, i.e. $\mathcal{F}_p(P, S, \Omega, E) = \delta(P - E)$; then Eq. 4.10 becomes:

$$Acc^p(E) = \int \eta_p(E, S, \Omega) d\Omega \boldsymbol{u} \cdot d\boldsymbol{S} = \langle \eta_p(E) \rangle \cdot Acc_{geo} \tag{4.12}$$

where the contamination factor $\langle \eta_p(E) \rangle$ is averaged over the solid angle and the detector area. In this case, it's possible to calculate the rejection power as:

$$R(E) = \frac{\langle \varepsilon(E) \rangle}{\langle \eta_p(E) \rangle} \tag{4.13}$$

4.2 Conversion mode

A photon passing through matter may convert into an electron-positron pair. The probability of a γ-ray to interact in a particular material is

$$P(t) = 1 - e^{-\frac{7}{9}\frac{t}{X_0}} \tag{4.14}$$

where t is the thickness and X_0 is the radiation length of the material.

In AMS-02 pair production offers an opportunity for photons detection. The material in front of the first silicon tracker plane, consisting of the TRD, the first two layers of TOF scintillators, and mechanical supports, represents $\approx 0.3 X_0$ [64]. According to Eq. 4.14 the probability for pair production is about 20 %.

Once converted, the incident γ-ray energy and direction can be estimated by tracking the resulting $e^+ e^-$ pair. The reconstructed energy will be the sum of the e^+ and e^- energies, corrected for the energy loss in the instrument, while the incident direction is obtained by the momentum-weighted average of the e^+ and e^- directions. Accurate reconstruction of the particle tracks is, therefore, of great importance, however there are two limiting effects. The first is due to the bremsstrahlung radiation, higher order QED effects and multiple scattering of electrons, which become less important for thin radiator. The second limitation is the measurement precision. Given a set of strip addresses above a defined signal threshold, the electron tracks are reconstructed and the parameters of the incident gamma are determined: however noise and missing hits may lead to spurious or ambiguous tracks. Moreover the x and y oriented strips are read with different pitches: given a track in the y projection, there are multiple possibilities for the x coordinate due to the ambiguity in the readout. In particular for high energy gamma rays, the hits from both tracks can be extremely close in space. For the first tracker layers, this distance may be smaller than the double-hit resolution of the detector ($\sim 100\,\mu$m). Clearly the accurate estimation of the incident γ-ray direction much depends on the choice of the best method to find electron tracks and to fit the position of the interaction vertex.

Protons, interacting at the TRD top, originate the main source of background. Among the secondaries, π^0 particles undergo gamma radiation decay, which in turn might produce an e^+e^- pair not distinguishable from a γ-originated signal. The only way to identify this kind of background is to rely on the TRD, showing any activity in the upper layers; still, a highly inclined proton might produce its charged secondaries outside the TRD acceptance.

In a recent MC analysis [65], an algorithm for the identification of the $\mathrm{e}^+\,\mathrm{e}^-$ pairs from γ conversions in the material upstream of the first tracker plane, have been developed. To be considered in the reconstruction, a LV1 flag corresponding to a signal in at least three out of four TOF scintillators planes is required. Furthermore, for the reconstruction of vertices, the following event selection is made:

- exactly two tracks in STD are required;
- at least 5 tracker layers contain reconstructed hits for one track and at least 4 layers for the other;
- no more than 50·(number of used layers) reconstructed hits;
- loose χ^2 cut on the track fit;
- no signal on the uppermost TRD level (inactive the first 3 layers of tubes).

The dynamic acceptance values for the analyzed energies are shown in Fig. 4.1 (a). At low energies (up to $\sim 10\,\mathrm{GeV}$) the acceptance is severely limited by the loss of one or both the electron tracks because of the high curvature of their trajectories. On the contrary, at higher energies ($> 50\,\mathrm{GeV}$), the maximum value is reached ($\sim 0.07\,\mathrm{m}^2\mathrm{sr}$) and a drop is again present only at very high energies where the STD resolution is reached and the tracks cannot be distinguished any more.

The shape of the acceptance can be approximated by:

$$Acc(E) = 0.082 \cdot \left(1 - \frac{1}{(E+0.09)^{0.44}}\right) \tag{4.15}$$

with Acc measured in $\mathrm{m}^2\mathrm{sr}$ and E in GeV.

The effective area ((b) in Fig. 4.1) has been calculated for a 2π bin in the azimuthal angle ϕ and a 0.05 bin in cosine of the zenithal angle θ. Its value on-axis

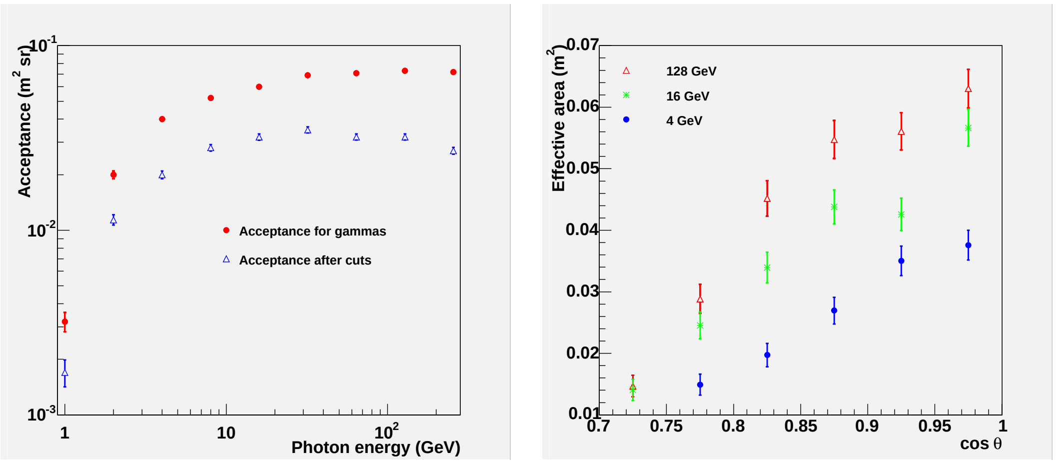

(a) (b)

Figure 4.1: AMS-02 *conversion mode.* (a) Dynamic acceptance before (dots) and after (triangles) background rejection cuts. (b) Effective area.

($cos\theta = 1$) ranges from $\sim 50\,\mathrm{cm}^2$ at 1 GeV to $\sim 600\,\mathrm{cm}^2$ at energies over 30 GeV; the shape, instead, resulted to be indipendent from energy.

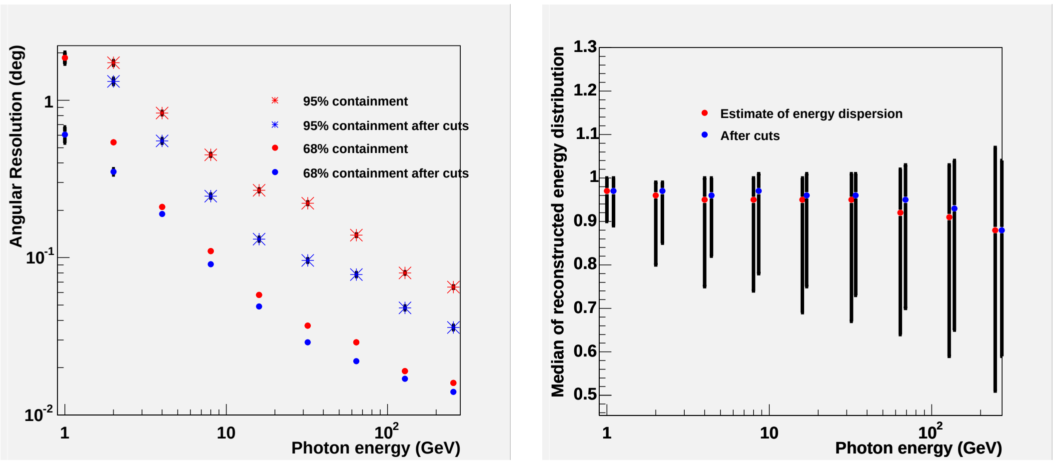

(a) (b)

Figure 4.2: Angular (a) and energy (b) resolution for the AMS-02 *conversion mode.* In both case results before and after background rejection cuts are reported.

The angular resolution, also indicated as the Point Spread Function (PSF) of the detector, was obtained by comparation between the reconstructed and the MC generated gamma ray direction (Fig. 4.2 (a)). It gradually improves with energy as the contribution from nucleus scattering and electron multiple scattering diminishes, until a minimum value is reached. The 68 % containment angular resolution is well described by:

$$\sigma_{68}(^\circ) = -0.71 + 0.73e^{1/E} \tag{4.16}$$

with the energy E expressed in GeV.

Finally in Fig. 4.2 (b) the median of the reconstructed gamma ray energy distribution, along with the 68 % containment dispersion, is shown.

Although the event statistics wasn't enough for a complete analysis, a first estimation of the total rejection power against protons was reached, applying further cuts to the basic data sample. The obtained lower limit is equal to $R > 2 \cdot 10^4$ at 90 % confidence level.

4.3 Single photon mode

The photons that doesn't convert before the first STD plane, about 80 % of the total, are not detected by the charged LV1 trigger. The ECAL, once provided with a "stand alone" trigger, can recover a big fraction of these events.

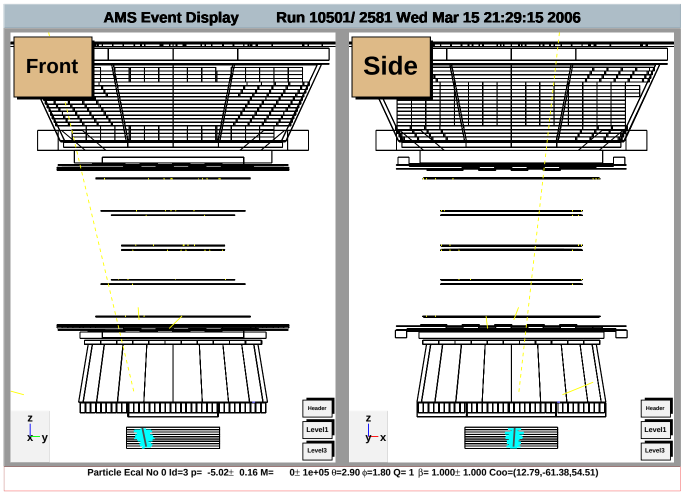

AMS Event Display Run 10501/ 2581 Wed Mar 15 21:29:15 2006

Particle Ecal No 0 Id=3 p= -5.02± 0.16 M= 0± 1e+05 θ=2.90 ϕ=1.80 Q= 1 β= 1.000± 1.000 Coo=(12.79,-61.38,54.51)

Figure 4.3: Signal event in *single photon mode*, as shown by AMS-02 MC simulation display. A photon that doesn't convert before the first STD plane, enters the electromagnetic calorimeter.

Thanks to the very wide dynamic range of the electromagnetic calorimeter, gamma rays spectrum measurements are possible up to ~ 1 TeV energy with good resolution. Despite the small FOV (about 20°), the dynamic acceptance, achievable in *single photon mode*, is comparable to the one obtained with the silicon tracker in *conversion mode*, while particle incoming direction is reconstructed with lower precision due to the worse angular resolution of ECAL.

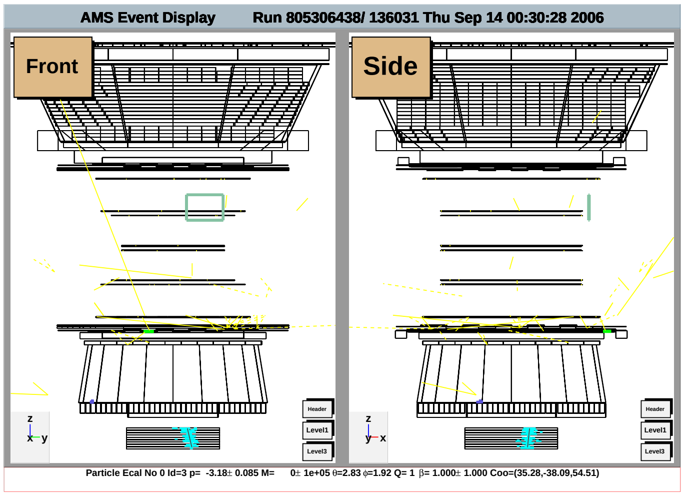

AMS Event Display Run 805306438/ 136031 Thu Sep 14 00:30:28 2006

Particle Ecal No 0 Id=3 p= -3.18± 0.085 M= 0± 1e+05 θ=2.83 ϕ=1.92 Q= 1 β= 1.000± 1.000 Coo=(35.28,-38.09,54.51)

Figure 4.4: Background event in *single photon mode*, as shown by MC simulation display. A proton produces secondary particles interacting with the lower TOF plane and, consecutively, an hadronic cascade in the electromagnetic calorimeter. Its incoming direction is reconstructed in a wrong manner as inside the TOF acceptance. Since the proton is not tagged by charged LV1 trigger, it could be identified as a photon.

The dominant background to the tiny γ-rays signal is produced by the most abundant cosmic rays components (p, He, C, e^-). They can reach the calorimeter from any directions, directly or indirectly producing secondaries in interactions with the rest of the apparatus (e.g. with the superconducting magnet vessel). Only a small fraction[1] of charged particles that enters the TOF acceptance is easily rejected: they generate a charged LV1 trigger signal, hitting the TOF planes. To get rid of the remaining background, it's necessary to look for a specific signature, corresponding to the presence of an electromagnetic shower in the ECAL and to a reconstructed incoming direction inside the TOF acceptance (while almost nothing is found in the other AMS-02 sub-detectors).

4.3.1 Cosmic rays fluxes

Fig. 4.5 shows how small is the flux of gamma rays, if compared to the fluxes of the main sources of background. The reported spectra are computed for primary

---

[1] About 5 % of the total, assuming an ECAL FOV of 20°.

cosmic rays. For a better estimate of backgrounds, one must refers, instead, to fluxes measuread in near earth orbit, i.e. in the space enviroment where AMS-02 will operate.

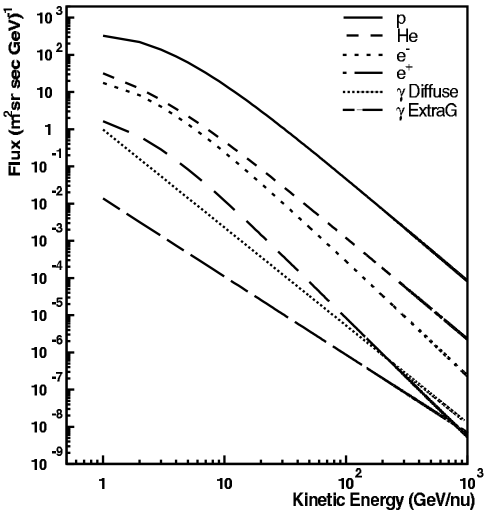

Figure 4.5: Primary cosmic rays composition, adapted from [69]. Diffuse γ-rays spectrums come from [10] and [32].

The fluxes of cosmic rays for near earth orbits are taken from [66], [67] and [68]. These fluxes correspond to the ones measured by AMS-01 mission on STS-91 Space Shuttle flight. That 10-day long precursor flight took place in June 1998 on Space Shuttle Discovery.

From these data one can see that for momenta above $\sim$ 8 GeV proton flux does not depend on the position along the orbit. The high energy protons are of cosmic origin (i.e. they are downward-going in AMS reference frame). Protons with energies below 8 GeV behave differently, in various positions of the orbit. In equatorial region protons are trapped by the magnetic field of the Earth, so they arrive, with the same probability, from the upper and the down directions. For high latitudes, the low energy proton flux is not affected by geomagnetic cutoff, which is below 1 GeV for $\Theta_M \simeq 1$ rad. So the flux of upward-going (i.e. trapped) protons is negligible for energies above 1 GeV, but the flux of low energy downward-going protons is much higher than in equatorial region.

Helium and electrons fluxes are about 2 orders of magnitude smaller than the proton one, but their behavior changes with latitude in the same way.

4.3.2 Monte Carlo simulation

In this study all the MC samples analyzed were generated by means of the dedicated AMS-02 simulation and reconstruction program, based on the GEANT package [70]. The simulated performance of the AMS subdetectors was checked against test flight data (AMS-01) and beam test data and found in good agreement with them. Nevertheless, being AMS-02 under construction, modifications, mainly to the description of the surronding support structure, will still be possible in future versions of the software.

The Monte Carlo code computes the path of the particles starting from a cubic volume of 3.9 m side (the so called "standard box"), which surrounds the detector. This choice allows an accurate tracing of charged particles through the magnetic field of the superconducting magnet and a description of the interactions eventually occurred in the subdetectors and in the support structures.

The particles are generated isotropically on the surface of the "standard box" around the detector. The initial direction is randomly extracted from a flat distribution in ϕ between 0° and 360°, and in $cos\theta$ between -1 and +1 (here and after the zenith of the detector corresponds to $cos\theta = 1$). Most of the particles generated in this way do not reach ECAL. To keep the generation efficency at reliable level, events are stored in the n-tuple only if they deposit a minimal energy in the calorimeter (a deposit of at least 120 MeV, referred as *minimum bias* ECAL Monte Carlo trigger, is required). In good approximation this generates non-biased samples of particles seen by the calorimeter, automatically fulfilling the ECAL trigger.

4.3.3 Monte Carlo data samples

In producing data samples, other selections were applied depending on the particle's component, in order to increase even more the generation efficiency.

Photons, with fixed energies from 1 to 300 GeV were generated on the top face of the "standard box" within a rectangular area of $140 \times 140\,\mathrm{cm}^2$ with $cos\theta < -0.85$, enough to fully cover the calorimeter FOV. Among all the simulated γ-ray events, the signal has been defined as photons that don't convert before ECAL (about 70 % of the total detectable in *single photon mode*) and are almost vertical, i.e. within a θ angle greater than 160° with respect to the detector z axis. They must cross the upper TOF plane and the fourth calorimeter superlayer, excluding the region read by the most external PMTs. This last requirement allows to avoid electromagnetic showers near the side of ECAL, where the transverse leakage may spoil the γ reconstruction.

In Table 4.1 the statistic of the photon samples is reported, before and after applying the preselection cuts.

ID	Energy [GeV]	N_{gen}	N_{presel}
γ	1	$1 \cdot 10^6$	3600
γ	1.5	$1 \cdot 10^6$	3500
γ	2	$1 \cdot 10^6$	3400
γ	3	$1 \cdot 10^6$	3400
γ	4	$1 \cdot 10^6$	3400
γ	5	$1 \cdot 10^6$	3400
γ	10	$0.7 \cdot 10^6$	2500
γ	20	$1 \cdot 10^6$	3500
γ	50	$0.7 \cdot 10^6$	2500
γ	100	$0.5 \cdot 10^6$	1700
γ	300	$0.5 \cdot 10^6$	1900

Table 4.1: Monte Carlo generated photon samples.

Background particles were generated uniformly on the 6 faces of the "standard box" since they can enter the calorimeter from any direction. The particles have an energy spectrum flat in the logarithm of momentum between 0.5 and $\sim 1900\,\mathrm{GeV/c}^2$.

Data samples, made up of protons, helium and electrons (see Tab. 4.2), were used to study trigger algorithms. To not increase too much time consumption for the MC generation time, in the diffuse gamma ray detection analysis, downward going protons only were taken into account.

ID	Momentum [GeV/c]	N_{gen}
p	$0.5 - 10$	$71 \cdot 10^6$
p	$10 - 200$	$61 \cdot 10^6$
p	$200 - 1890$	$90 \cdot 10^6$
He	$0.75 - 200$	$15 \cdot 10^6$
e^-	$0.2 - 30$	$\sim 2.3 \cdot 10^6$

Table 4.2: Monte Carlo generated background samples.

---

[2] In this way the statistical significance of the sample is closer to the real one (e.g. $\propto E_{KIN}^{-2.78}$ in case of protons) and the energy spectrum can still be easily reconducted to any user defined spectrum.

Chapter 5

ECAL stand alone trigger

The electromagnetic calorimeter "stand alone" trigger has been set up in order to recover the photons not acquired by the standard AMS-02 trigger based on the TOF counters. The same trigger will be useful to switch off the ACC system in case of high energy electrons or positron interactions, solving in this way the problem of the backsplash from the calorimeter.

In this chapter a description of the ECAL trigger system is reported, starting from the Monte Carlo simulation.

5.1 Project goals and basic ideas

In ECAL trigger designing, major efforts were spent to recover efficiency down to the lowest possible photon energy, while preserving the compatiblity with the rest of AMS-02 trigger in terms of timing, acquisition rate and power consumption.

In particular the system is required to satisfy the following specifications:

- efficiency: almost 100 % at high energies (above 10 GeV); as high as possible down to the lowest possible energies;

- timing: generation of a Fast trigger signal within 180 ns; its time walk below 20 ns to switch AC counters off, while preserving TOF time resolution; the level 1 signal has to be produced less than 650 ns after the Fast trigger.

- rate: a Fast trigger rate below 10 KHz (1 % dead time) and LV1 trigger below 100 Hz ($\sim 5\,\%$ of total rate);

- stability: low sensitivity to external condition (temperature, solar activity ...);

- robustness: good rate and efficency also in case of broken PMT's (firing or dead) or of global gain fluctuations; redundancy of all electronic devices;
- power consumption: $\leq 15\,\mathrm{W}$;
- weight (cables and boards): $< 5\,\mathrm{Kg}$.

The basic idea to fulfill all these requirements is to build up a trigger with a granularity of 1 PMT ($1.8 \times 1.8\,\mathrm{cm}^2$). This choice is a compromise between the request of a high energy deposit on a single readout channel (better signal/noise ratio) and the request of a good shower image reconstruction giving a good angular information. The choice of 1 PMT has also the great advantage to allow to use the *last dynode* signal, which is very fast and comes out directly from the PMT.

In the present MC study the last dynode is naturally assumed to be proportional to the sum of the 4 anodes. The same proportionality constant is taken for all the PMT's. In the following the ECAL superlayers will be referenced according to the scheme of Fig. 5.1.

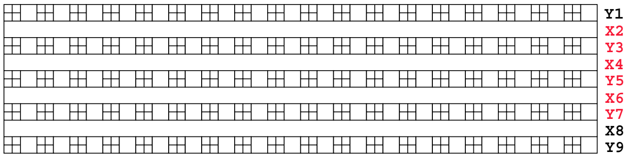

Figure 5.1: The ECAL superlayers numeration used in the MC simulation. In red the superlayers utilized for the trigger decision.

5.2 Signal efficiency and background rate

The efficiency in detecting signal and the total background rate are the two key parameters to check the factor of merit of the trigger system during the designing process.

The γ-rays efficiency as a function of energy is computed as:

$$\epsilon(E_i) = \frac{N^{\gamma}_{trig}(E_i)}{N^{\gamma}_{presel}(E_i)} \tag{5.1}$$

where $N^{\gamma}_{presel}(E_i)$ is the total numbers of events of fixed energy E_i, representing the signal in the Monte Carlo data sample (see Tab. 4.1) and $N^{\gamma}_{trig}(E_i)$ is the number of events which the trigger algorithm identifies as photons.

The background rate is computed by dividing the momentum spectrum of the incoming particles in bins. For the l-th particle CR component, the contribution of the single i-bin to the total rate is:

$$R^l(\Delta P_i) = \frac{N^l_{trig}(\Delta P_i)}{N^l_{gen}(\Delta P_i)} \times A_{box} \times \Phi^l(\Delta P_i) \tag{5.2}$$

where A_{box} is the geometrical acceptance of the *standard box*, $\Phi^l(\Delta P_i)$ is the l-th component flux integrated over the i-th bin (measured in $\mathrm{Hz\,m^{-2}\,sr^{-1}}$), $N^l_{gen}(\Delta P_i)$ is the initial number of events generated in the ΔP_i momentum range and $N^l_{trig}(\Delta P_i)$ is the number of background candidates. The total background rate on ECAL is equal to the sum of the contributions of all the momentum bins.

In general the initial kinetic energy of background CR components is not well reconstructed in ECAL, mostly due to the different behaviour of the hadronic shower respect to the electromagnetic one. To better understand the contribution of the background respect to the signal, it is therefore much helpful to estimate the rate as a function of the deposited energy in the ECAL. This can be obtained by entering each bin of a histogram with:

$$N^l_{cor}(\Delta E_i) = N^l_{trig}(\Delta E_i) \times \frac{log\ P^{max}_{gen} - log\ P^{min}_{gen}}{log\ P^{max}_{i} - log\ P^{min}_{i}} \times \Phi^l(\Delta P_i) \tag{5.3}$$

where the number of MC events passing the trigger and resulting in an energy deposit within the i-th bin, $N^l_{trig}(\Delta E_i)$, is corrected by a factor which converts the initial MC generated spectrum (flat in the logarithm of momentum between P^{max}_{gen} and P^{min}_{gen}) to the real measured one. Once filled, the histogram is normalized to the l-th CR component total rate.

For all background samples, the TOF trigger conditions were required before applying ECAL trigger. This procedure removes 5 % of proton candidates accepted by the γ trigger algorithm. All numbers quoted in this study are therefore corrected for the charged trigger selections.

5.3 Trigger Strategy

The initial ratio between photons and background particles rate is extremely small.

For cosmic protons the initial rate is reported in Fig. 5.2 (a) and 5.2 (b), where it is compared to the rate of gamma rays emitted by the galactic center. Events are collected when they pass the selection criteria described in Par. 4.3.3. The proton flux corresponds to a quasi polar orbit (from [66]) and represents the worst case in terms of low energy particle rate. The total initial rate for protons is about 2000 Hz, about $3 \cdot 10^4$ times more than the rate for photons.

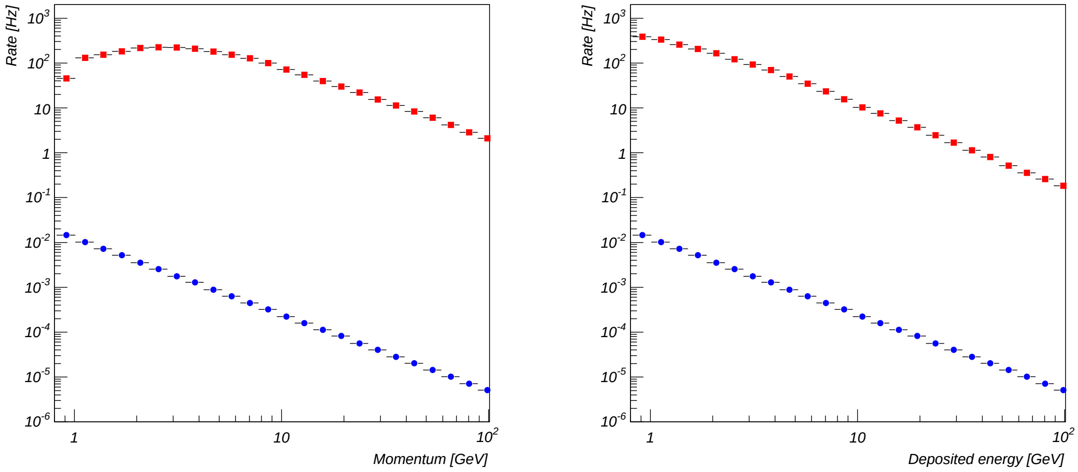

(a) (b)

Figure 5.2: Spectrum as a function of the particle momentum (a) and as a function of the deposited energy in ECAL (b) for downward going protons (squares) and photons (dots). The "minimum bias" MC trigger, i.e. a minimum energy deposit of 120 MeV, is required. For the protons, fluxes are taken from a quasi polar orbit (AMS-01) and events with TOF trigger flag are subtracted. The total rate is about 2000 Hz. For the photons the rate is less than 0.1 Hz.

To reduce the background rate and create a relatively clean trigger is very important to exploit at the best all the signal characteristics. The large difference between the radiation length ($X_0 \simeq 0.9\,\text{cm}$) and the interaction length ($\lambda_I \simeq 32\,\text{cm}$) in ECAL can be used to separate photons from protons: the low energy photons release all their energy in the calorimeter, while for the small fraction of interacting protons, their hadronic shower is generally not contained in the calorimeter. Fig. 5.3 (a) shows the rate of protons releasing a total energy deposit[1] in the calorimeter above a certain threshold. One sees that a simple cut at 5 GeV on the total deposited energy in the calorimeter could already reduce to 100 Hz the total trigger rate.

However total energy is only one of the informations of the electromagnetic

---

[1] It must be noticed that, according to Monte Carlo, the fraction of visibile energy in the scintillating fibers, respect to the total deposited energy (lead + fibers) is 2 times larger for protons and helium than for the electromagnetic particles. The energy deposit is evaluated applying to the visible energy the calibration constants obtained for electrons. Thus, the energy deposit for non-electromagnetic particles appears to be double of what it is in reality. Fig. 5.3 (b) show that for He stopped particles the energy deposit is twice their kinetic energy.

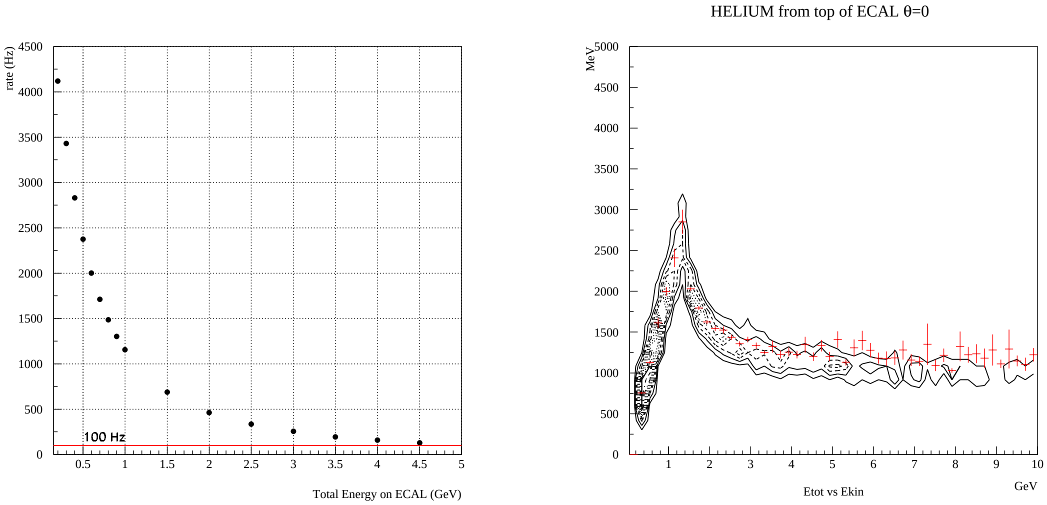

(a) (b)

Figure 5.3: (a) Rate of protons as a function of a threshold on the total energy deposit in the calorimter. (b) Electron-calibrated energy deposit of vertical α particles generated on the top of calorimeter versus their kinetic energy. Crosses correspond to the average value.

shower. In fact a finer selection can be obtained by looking at how the energy deposit is distributed between the different superlayers (i.e. by taking into account the longitudinal shower shape). For 2 GeV photons, the energy deposit in the superlayers is quite inhomogeneous with a maximum in the 3^{rd} superlayer (Fig. 5.4 top). The information of the first superlayer is useless for most photons, because some of them do not convert or convert too late in it. Also the energy deposit in the last two superlayers is very low because the shower is already almost completely absorbed. So the only useful superlayers for the 2 GeV photons are the ones from X2 to Y7.

On the contrary for an isotropic flux of downgoing protons the shape of the energy deposit is the same on all the superlayers (Fig. 5.4 bottom). Nonetheless, a cut on the total energy deposit in the superlayer requires an analogic sum of 36 channels that is not an easy task due to the tight requirements on timing and power consumption.

The problem can be solved using the lateral shape of the electromagnetic shower: since the Moliere radius of the ECAL is of the order of 1 PMT, most of the shower energy is concentrated in 1 or 2 PMT's. On the contrary, the hadronic shower is, on average, much larger. Therefore the maximum energy deposited on a single PMT is also an excellent variable to separate photons from protons (Fig. 5.5).

For Helium (Fig. 5.6), the separation is harder because energy deposit is higher:

ionization is 4 times larger and particles with less than 1.5 GeV of kinetic energy are completely stopped inside the calorimeter (Fig. 5.3 (b)).

Furthermore, the use of this variable (maximum energy in a single PMT) simplifies the technical realization of a trigger: a threshold is imposed on the last dynode signal of each PMT without any logic operation involving different PMT's. The value of this threshold is the same for all the PMT's in the same superlayer but is different from superlayer to superlayer, in order to exploit the longitudinal shape of the electromagnetic shower.

5.4 Fast trigger logic

The ECAL Fast trigger is realized just imposing a threshold on each PMT of the 6 relevant superlayers (from X2 to Y7) and requiring at least 2 (out of 3) superlayers for each view with at least one PMT above threshold. This request guarantees a good robustness with respect to single PMT failures and an high efficiency also on lately converting photons.

The threshold settings have been studied in view to obtain a 90 % efficiency on 2 GeV photons[2]. For low energy deposit such as the ones obtained from 2 GeV photons, the two views (X and Y) can be considered as uncorrelated[3]. Therefore the efficiency can be written as:

$$\epsilon^{Fast} = \epsilon_X^{Fast} \cdot \epsilon_Y^{Fast} \tag{5.4}$$

and, therefore, the efficiency on each single view must then be 95 %.

For each view, it's possible to set the thresholds for the first two superlayers, the ones with the higher energy deposit, looking at the correspondent contour plot (Fig. 5.7, 2^{nd} and 4^{th} rows on the left). The threshold on the third superlayer is obtained looking at the correspondent energy deposit when only one of the previous two is above threshold and asking for a global efficiency of 95 %. For the protons (Fig. 5.7, 1^{nd} and 3^{th} rows on the left) the curves of isoprobability coincide with $E_i^{max} + E_j^{max}$ = constant: this indicates that the background rate depends on the sum of the thresholds, rather than on each threshold separately.

The resulting thresholds are reported in Table 5.1.

---

[2] This is *a posteriori* compatible with the request of a total trigger rate below 100 Hz and with the lower limits on the values of the thresholds imposed by the electronics.

[3] Actually, the two energy deposit are not uncorrelated. However this hypothesis is assumed since the use of the correlation will complicate significantly the hardware required for the trigger implementation

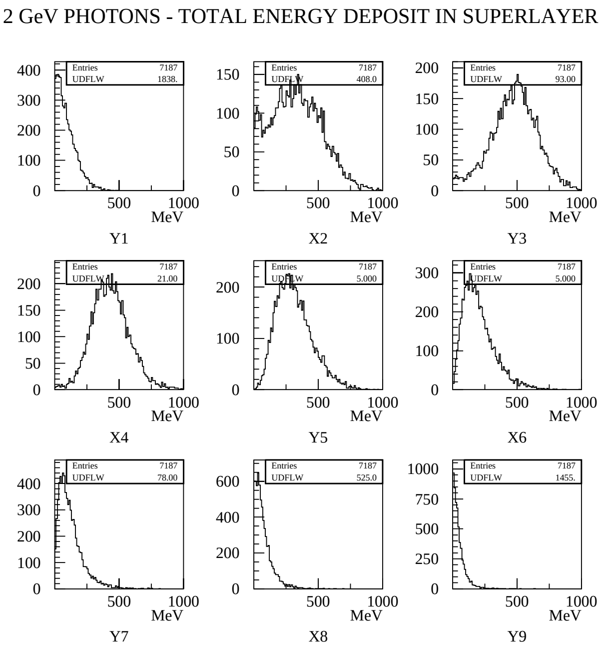
2 GeV PHOTONS - TOTAL ENERGY DEPOSIT IN SUPERLAYER

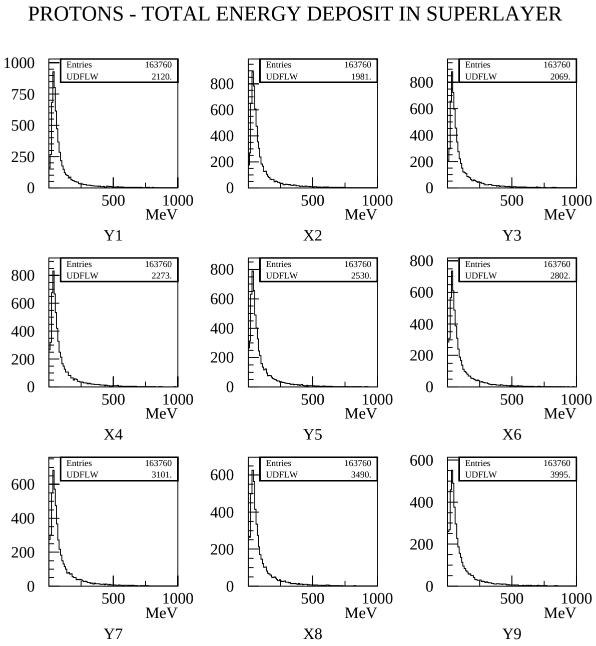
PROTONS - TOTAL ENERGY DEPOSIT IN SUPERLAYER

Figure 5.4: Energy deposited in the ECAL superlayers. (top) 2 GeV vertical photons. (bottom) Downward going protons. In both case underflows indicate the events with null energy deposit.

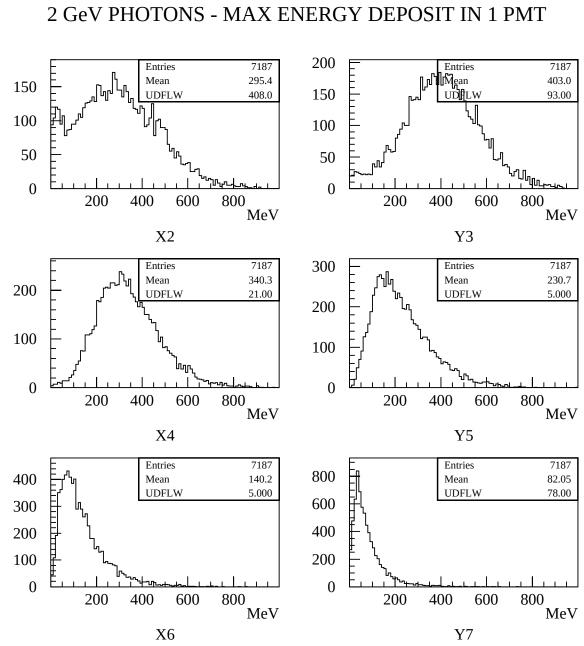

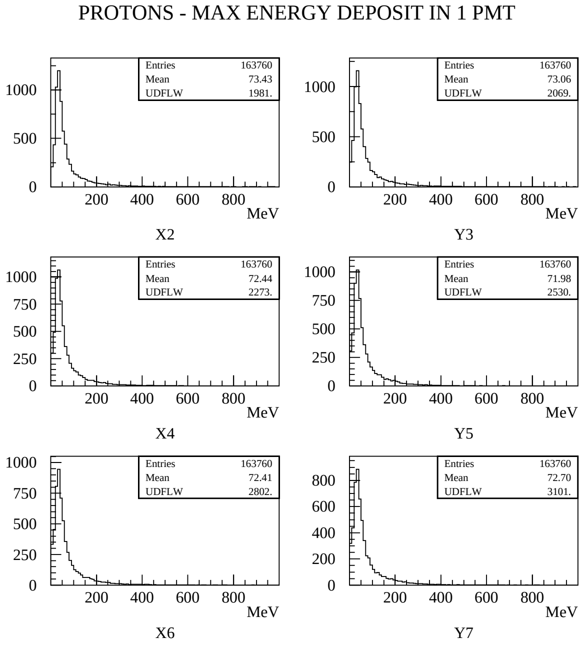

Figure 5.5: Maximum energy deposited in a single PMT for each superlayer. (top) 2 GeV vertical photons. (bottom) Downward going protons. In both case underflows indicate the events with null energy deposit.

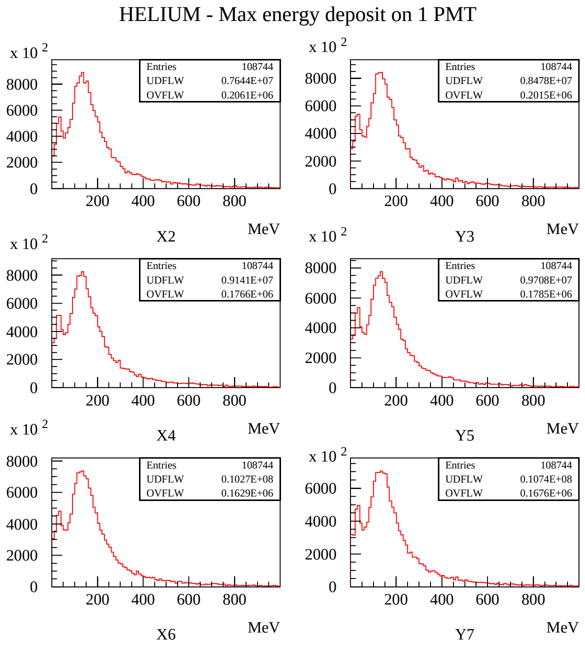

Figure 5.6: Maximum energy deposited in a single PMT for each superlayer by α particles. The underflows indicate the events with null energy deposit.

Superlayer	X2	Y3	X4	Y5	X6	Y7
Thresholds [MeV]	80	180	140	60	100	100

Table 5.1: Thresholds in MeV for each superlayer.

The Fast trigger efficency for different photon energies with incident angle greater then 170° and 160° is reported in Table 5.2.

E^γ [GeV]	1	1.5	2	3	4	5	10	20	50	100	300
$170^\circ \div 180^\circ$	20	66	91	98	98	98	99	99.5	99.5	99.7	99.7
$160^\circ \div 170^\circ$	19	66	91	98	99	99	99	99.4	99.6	99.5	99.2

Table 5.2: Fast trigger efficiency (in %) for photons.

At the quasi polar orbit the most relevant backgrounds are: downward going protons (240 Hz), downward going α (160 Hz), downward going electrons (24 Hz).

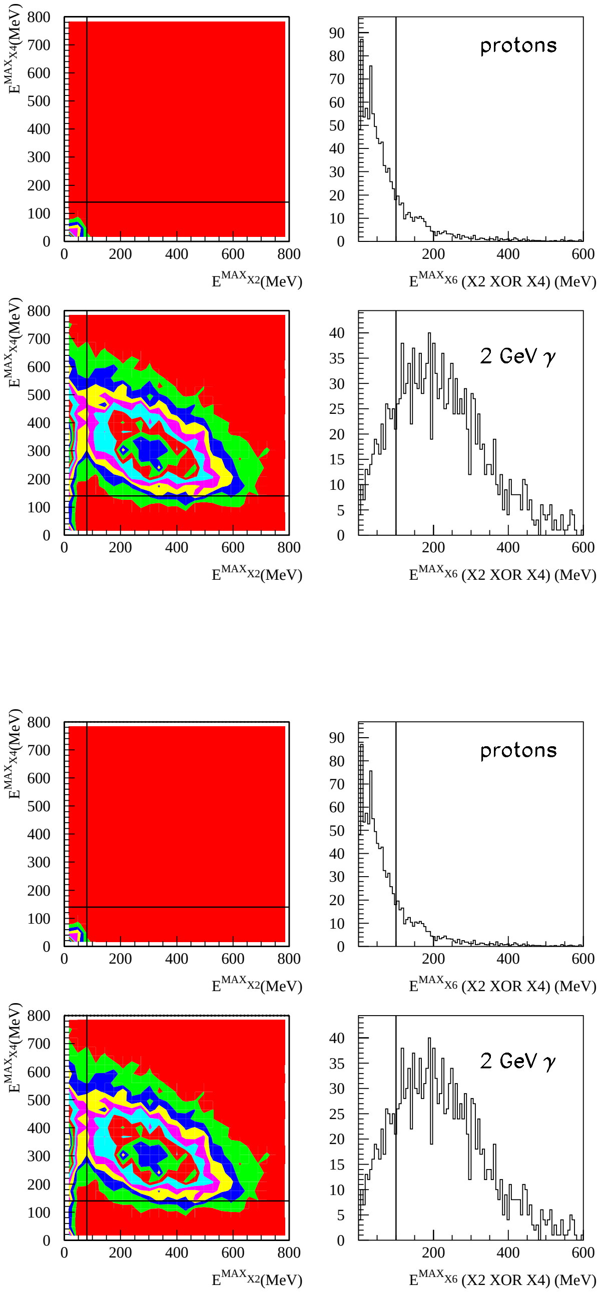

Figure 5.7: Maximum energy deposited in a single PMT for the X (top) and Y (bottom) superlayer by protons and 2 GeV photons. Left: X4 vs X2 (Y5 vs Y3) without cuts. Right: X6 (Y7) when only one between X2 (Y3) and X4 (Y5) is above threshold. The lines show the thresholds.

5.5 Angular cut

The photon trajectory interacts the tracker planes and the calorimeter when its angle is greater than ∼ 160°. That corresponds to a difference in the impact point on two consecutive superlayers for the same view (X or Y) of less than 1 PMT. This information is included in the first level trigger as a selection criterium on the incoming particle direction.

The particle direction is evaluated by taking, for each superlayer, the average position of the PMT's above threshold (Fig. 5.8), that will be called from now on *center of gravity* and indicated with b. The cut on the photon direction is imposed using the distances between centers of gravity in the superlayers belonging to the same view:

$$\Delta b_{24} = |b_2 - b_4|; \quad \Delta b_{46} = |b_4 - b_6|; \quad \Delta b_{26} = \frac{|b_2 - b_6|}{2}; \tag{5.5}$$

$$\Delta b_{35} = |b_3 - b_5|; \quad \Delta b_{57} = |b_5 - b_7|; \quad \Delta b_{37} = \frac{|b_3 - b_7|}{2}; \tag{5.6}$$

If there are no PMT's above threshold in one superlayer, the corresponding center of gravity is not defined and the distances including it are set to 0 as default. Since the Fast trigger requires a PMT above threshold in at least 2 superlayers per view, at least one distance per view is always defined.

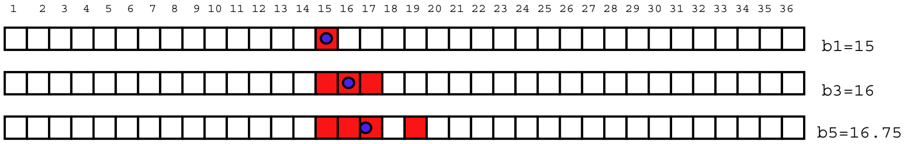

Figure 5.8: Example of *centers of gravity*: the average position of PMT's above threshold in a superlayer.

The distances Δb_{26} and Δb_{37} are more accurate and must be preferred when imposing the angular cut. The variables used for the angular cut are therefore:

$$\Delta {b_X}^{max} = \begin{cases} \Delta b_{26} & \text{if defined,} \\ max(\Delta b_{24}, \Delta b_{46}) & \text{otherwise} \end{cases} \tag{5.7}$$

$$\Delta {b_Y}^{max} = \begin{cases} \Delta b_{37} & \text{if defined,} \\ max(\Delta b_{35}, \Delta b_{57}) & \text{otherwise} \end{cases} \tag{5.8}$$

Fig.5.9 (top) shows $\Delta {b_X}^{max}$ and $\Delta {b_Y}^{max}$ for photons of 2,5,10,100 and 300 GeV with $160° < \theta < 170°$ and satisfying the Fast trigger condition. For higher energy photons the number of events with Δb larger than 1 is higher. A simple cut at 1.15 PMT's for both ${\Delta b_X}^{max}$ ${\Delta b_Y}^{max}$ (*hard angular cut*) would produce undesired inefficiency at very high energies. Fig.5.9 (bottom) shows how it's possible to recover efficency at high energies by imposing a cut depending on the total number of PMT's above threshold ($Nhit$) in the last 4 superlayers(*soft angular cut*):

$$ {\Delta b_X}^{max} < \begin{cases} 1.15 & \text{if } (Nhit_{X4} + Nhit_{X6}) < 5, \\ 2.15 & \text{if } (Nhit_{X4} + Nhit_{X6}) \geq 5, \end{cases} \tag{5.9} $$

$$ {\Delta b_Y}^{max} < \begin{cases} 1.15 & \text{if } (Nhit_{Y5} + Nhit_{Y7}) < 6, \\ 2.15 & \text{if } (Nhit_{Y5} + Nhit_{Y7}) \geq 6, \end{cases} \tag{5.10} $$

The efficiency of this cut for the different photon energies and direction is shown in Fig. 5.10 (top). Fig. 5.10 (bottom) shows the distribution of ${\Delta b_X}^{max}$ ${\Delta b_Y}^{max}$ for the protons passing the Fast trigger. The soft angular cut guarantees an additional total rejection factor of 3.5 with respect to the Fast trigger.

5.6 Level 1 trigger efficiency and rate

The efficiency for photons passing the thresholds and angular cuts is shown in the Tab. 5.3. It's larger than 99 % starting from 5 GeV. Also the efficiency at 1 GeV is appreciable (∼ 20 %).

E^γ [GeV]	1	1.5	2	3	4	5	10	20	50	100	300
170° ÷ 180°	20	66	90	97	98	98	99	99.3	99.0	99.7	99.7
160° ÷ 170°	18	65	89	97	98	98	99	99.3	99.5	99.5	99.2

Table 5.3: Level 1 trigger efficiency (in %) for photons.

At the polar orbit the most relevant backgrounds are: downgoing protons (70 Hz), downgoing α (39 Hz), downgoing electrons (9 Hz). The total Level 1 trigger rate is ∼ 115 Hz. The rate from upgoing electrons at the equatorial orbit (the worst case) is instead only 0.6 Hz, because the bottom of the calorimeter absorbs the low energy particles and furthermore the thresholds are chosen in such a way to follow the longitudinal development of an electromagnetic shower coming from top (lower thresholds on the upper superlayers).

Fig. 5.11 shows the Level 1 trigger dynamic acceptance for protons and helium as a function of the kinetic energy. The peak at 1.2 GeV in the helium distribution

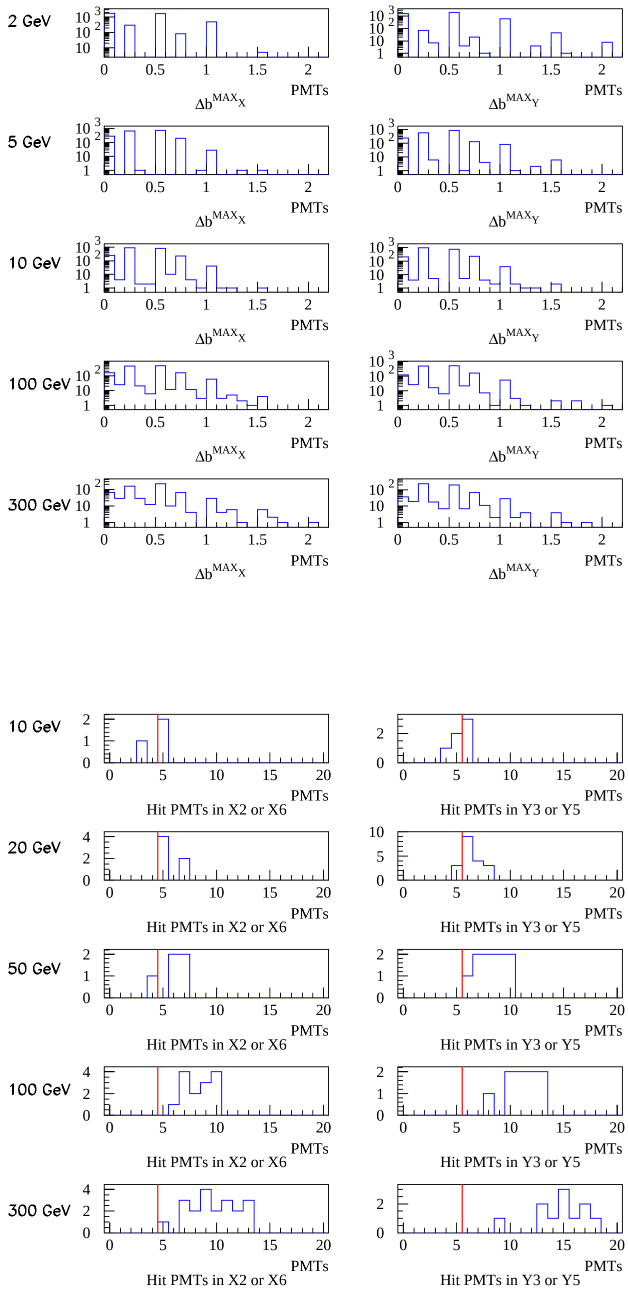

Figure 5.9: (top) Maximum distance between centers of gravity for the two views for different photon energies. The Fast trigger has been applied as preselection. (bottom) Number of PMT's above threshold in the last 2 superlayers in X and Y view for photon passing the Fast trigger but rejected by the hard angular cut. In both pictures photon angles are in 10° ÷ 20° range.

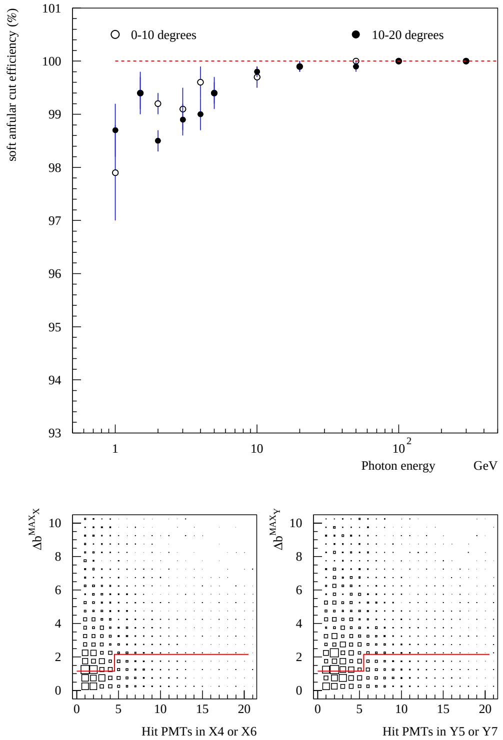

Figure 5.10: (top) Efficiency of the soft angular cut for different photon energies and angles. (bottom) Maximum distance between centers of gravity vs number of hits in the last 2 used superlayers in the two views for the protons passing the Fast trigger selection. The continuos line indicates the soft angular cut.

is due to the stopped particles. The cut is not sharp but, in both cases, no particle with energy deposit lower than 600 MeV is accepted.

In Fig. 5.12 the contamination (left) and the rate as function of the zenithal angle (θ) respect to the AMS main axis, are reported for protons, before and after the “stand alone” trigger request. Fig. 5.13 shows the final trigger rate from the main background sources (cosmic protons, α particles and electronts) compared with the rate of two possible signals: galactic photons from the center of the galaxy and extragalactic photons.

5.7 Robustness studies

The robustness of the ECAL trigger has been studied by looking at the variation of the photon efficiency and of total rate in case of techincal failures in the PMT’s, in

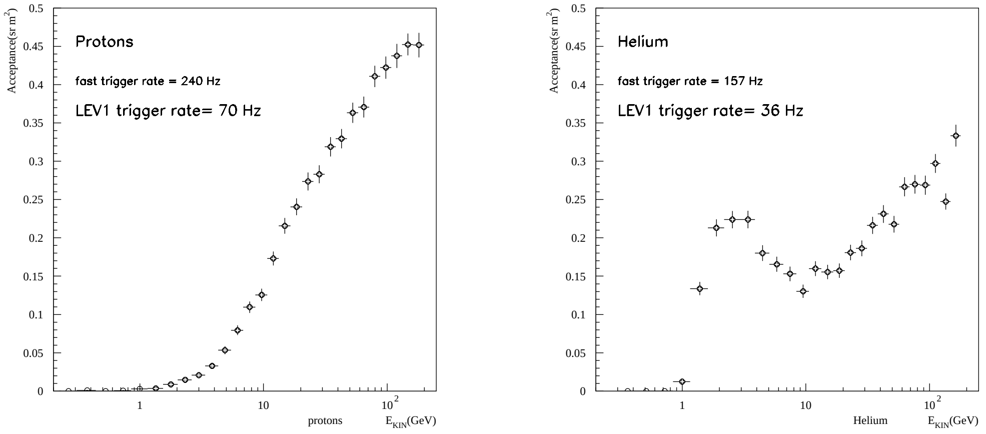

(a) (b)

Figure 5.11: Proton (a) and Helium (b) acceptance as function of kinetic energy for Level 1 trigger.

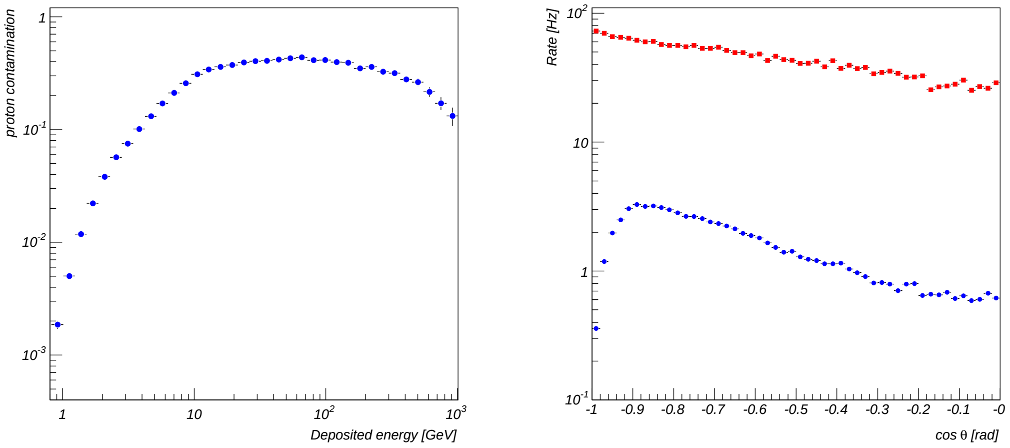

(a) (b)

Figure 5.12: (a) Proton contamination after ECAL trigger as a function of deposited energy. (b) Proton rate distribution for $90° < \theta < 180°$ before (squares) and after (dots) the trigger; both distributions are flat in ϕ.

HV channels or in electronics in general.

The study has been performed using 20 random configurations for 10 PMT's, spread out over the whole calorimeter. In addition 2 specially unlucky configuration have been investigated: one with all the bad PMT's in the superlayers Y3 and X4

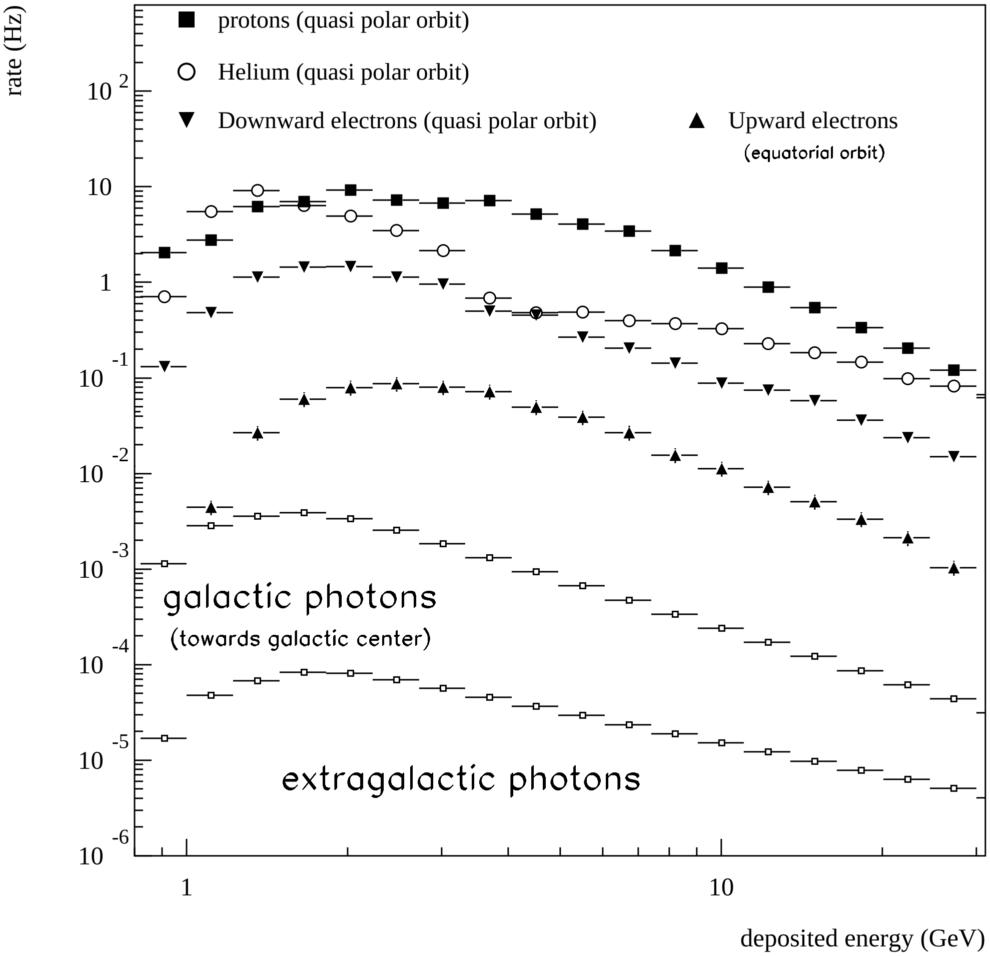

Figure 5.13: Rate of backgrounds (flux measured by AMS-01) and non-converted photons (flux adapted from [10], [32]) after level 1 ECAL stand alone trigger.

and one with all the bad PMT's in two adiacent columns.

5.7.1 Dead PMT's

The efficiency for photons in case of 10 dead PMT's is shown in Fig. 5.14 (a). The white crosses show the efficiency without any bad PMT; the error bars indicate the efficiency range for the 20 random configurations with the black circle as average; the white circles show the case of 10 dead PMT's in two adiacent columns; the white

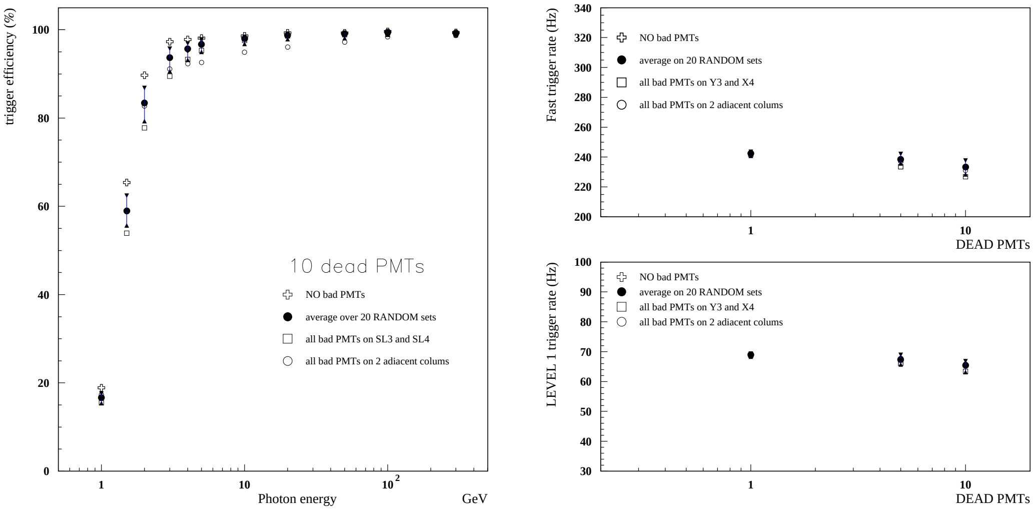

(a) (b)

Figure 5.14: (a) Efficiency for photons in case of 0 (white cross) or 10 dead channels: range (error bars) and average (black circles) over 20 random configurations; configurations with all the bad PMT's in two adiacent columns (white circle) or in superlayers Y3 and Y4 (white squares). (b) Fast trigger and level 1 trigger proton rates in case of 1, 5 or 10 dead channels. Reference symbols as for picture (a).

squares correspond to the case of 10 dead PMT's all in the superlayer Y3 and Y4, where the maximum of the electromagnetic shower is expected.

As expected, the low energy photons are the most sensitive, having, usually, only one PMT per superlayer above threshold. The total rate for protons slightly decreases and is in general quite stable. The rate in case of 1,5 or 10 dead PMT's is presented in Fig. 5.14 (b). The meaning of the symbols is the same as above.

5.7.2 Hot PMT's

The study on "hot" PMT's has been performed by increasing the gain of the PMT's by a factor 10. The PMT's are chosen according to the same 20 random sets and the 2 special sets used for the dead PMT's analysis.

In this case the efficiency for the photon is not a problem: it's stable for the higher energies and even better for the very low energies (Fig. 5.15 (a)). A priori this was not obvious, since the presence of bad PMT's could affect the angular cut: the picture shows that the effect is really small.

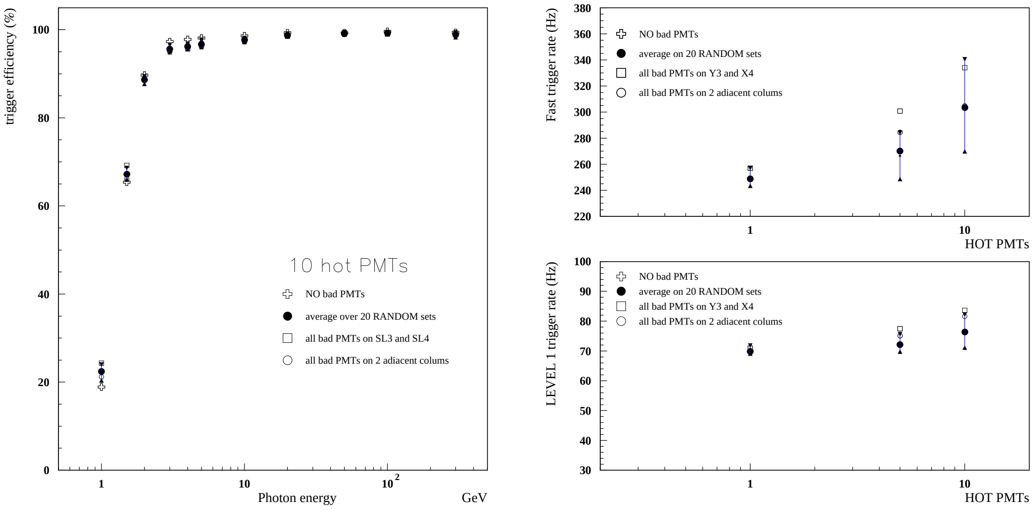

(a) (b)

Figure 5.15: (a) Efficiency for photons in case of 0 (white cross) or 10 hot PMT's: range (error bars) and average (black circles) over 20 random configurations; configurations with all the bad PMT's in two adiacent columns (white circle) or in superlayers Y3 and Y4 (white squares). (b) Fast trigger and level 1 trigger proton rates in case of 1, 5 or 10 hot channels. Reference symbols as for picture (a).

The rate for protons changes significantly, but not dramatically in case of many hot channels (Fig. 5.15 (b)): in the worst case with 10 hot PMT's, the Level 1 trigger rate raises to 84 Hz for cosmic protons.

5.8 Stability

5.8.1 Global gain variation

Due to the temperature fluctuation, the PMT gain can move coherently in one direction. In case of global gain fluctuation of $-30\,\%$, the efficiency for energies up to 2 GeV changes significantly. The effect is negligible for higher energy photons (Fig. 5.16).

Also the proton rate changes in a significative way, moving from 40 Hz (when the gain is decreased to $-30\,\%$) to 100 Hz (gain $+30\,\%$). The Fast trigger rate correspondetly moves from 150 to 400 Hz. If instead, the gain fluctuations are uncorrelated among PMT's, the net effect is negligible.

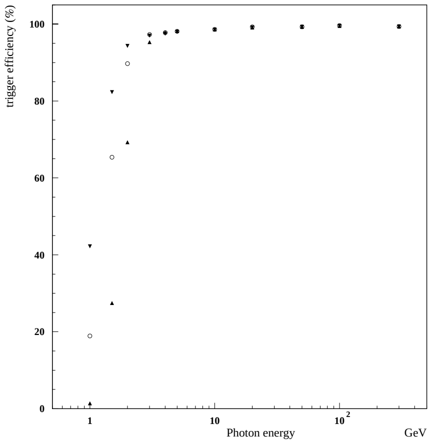

Figure 5.16: Effect of a coherent gain variation of $-30\,\%$ (lower triangles) and $+30\,\%$ (upper triangles) on LV1 photon efficiency.

5.8.2 Decreased solar activity

The presented proton rates correspond to the flux measured by AMS-01, i.e. during a pretty low solar activity ($\Phi \sim 500\,\mathrm{MV}$). In the period when AMS-02 is expected to take data (from 2007 to 2010) the solar activity is expected to be higher.

Nevertheless, even for a modulation parameter as low as $\Phi = 400\,\mathrm{MV}$[4], the trigger proton rate rises only up to 75 Hz.

5.9 Backsplash recovering

A high energy electrons or positrons entering the calorimeter, produces many upward going backsplash particles. These particles may fire the anticoincidence counters, causing an inefficiency in the charged LV1 trigger. The ECAL Fast trigger turned out to be very useful in recovering this inefficiency.

The MC sample used in this study is made up of positrons of fixed energy that trigger the TOF counters (at least 3 planes out of 4) and do not intersect directly the ACC. Like for the photon samples, they must intersect the fourth calorimeter superlayer, excluding the region read by the most external PMT's.

Fig. 5.17 shows the percentage of positrons triggering the TOF's without firing the veto counters, with respect to all the ones that trigger the TOF's. The effect

---

[4] The corresponding proton flux has been obtained using the Gleeson-Axford parametrization for the cosmic ray modulation due to solar activity [71].

of the backsplash is evident: the ratio quickly decreases with the increase of the positron energy. The ECAL Fast trigger can be used to recognize electromagnetic showers in the calorimeter and to inihibit the ACC veto. As shown in the picture, the inefficiency due to backsplash is completely recovered including the Fast ECAL signal in the charged LV1 trigger logic.

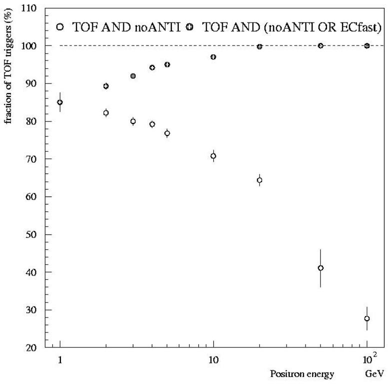

Figure 5.17: Ratio of positrons triggering the TOFs without switching on the veto counters with respect to the ones that trigger the TOFs (white dots). Ratio of positrons triggering the TOFs without switching on the veto counters or firing the ECAL Fast trigger with respect to the ones that trigger the TOFs (black dots).

5.10 Realization of the trigger system

As described above, the ECAL trigger must analyze the pulse generated by the last dynode of each PMT of 6 superlayers, for a total of 216 PMT's (108 for each X, Y view). The designed scheme foresees two separated sections, one made up of analog devices and located on EIB's, one purely digital lodged in the ECAL electronics crates.

In the EIBs involved in the trigger, the analog section (Fig. 5.18 (a)) amplifies the signals of the last dynode from the 9 linked PMT's by a factor of 10. It also compares these signals with a given threshold set by a digital to analog converter (DAC). If the signal is above threshold, the output of the comparator is shaped by means of a flipflop to form a 100 ns pulse and sent to the ECAL crate. Many configurations with different electrical components were tested for timing and power consumption; as a result the best was the one with the AD8014 operational amplifier, the comparator MAX976 and the flipflop SNJ54HC74.

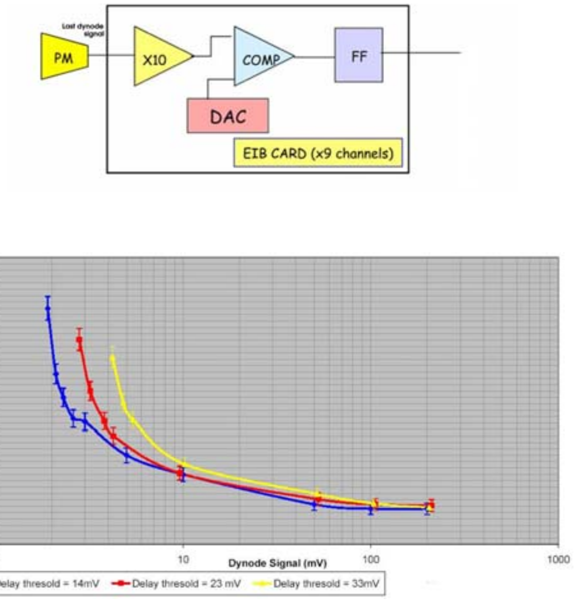

Figure 5.18: (top) Building blocks diagram of the trigger system analog section, installed on EIBs. (bottom) Measurements of the delay between dynode signal and comparator front for different thresholds.

The delay time from the input signal to the comparator front depends on the height of the signal with respect to the threshold. For a signal height comparable to the threshold the delay is independent from the threshold itself within reasonable limits and it is $\sim$ 65 ns. On the other hand, for very high signals the delay time becomes $\sim$ 30 ns due to the OPA slewing rate (see Fig. 5.18 (b)). According to these data the digitalization process is completed after about 70 ns and introduces a maximum time spread 35 ns long, including also the transit time spread inside the scintillanting fibers. On each EIB, the measured supply currents for the trigger part are 50 mA on +3.5 V and 10 mA on −2.5 V, giving a power consumption of 200 mW. Considering all the 216 dynode channels (24 EIBs), the expected total power consumption is about 4.8 W.

The trigger digital section performs all the trigger algorithm computations and sends the final decision to the global AMS-02 trigger card (JLV1). Two cards called ETRGs (Fig. 5.19), each one processing the signal related to either the X or the Y projection, collect flipflop pulses coming out from three superlayers. They generate both the Fast and the LV1 signals and include the input data in the event data stream, using the standard common digital part (CDP) to comunicate with the JINF card.

The trigger algorithm has been implemented in an Actel FPGA provided with a

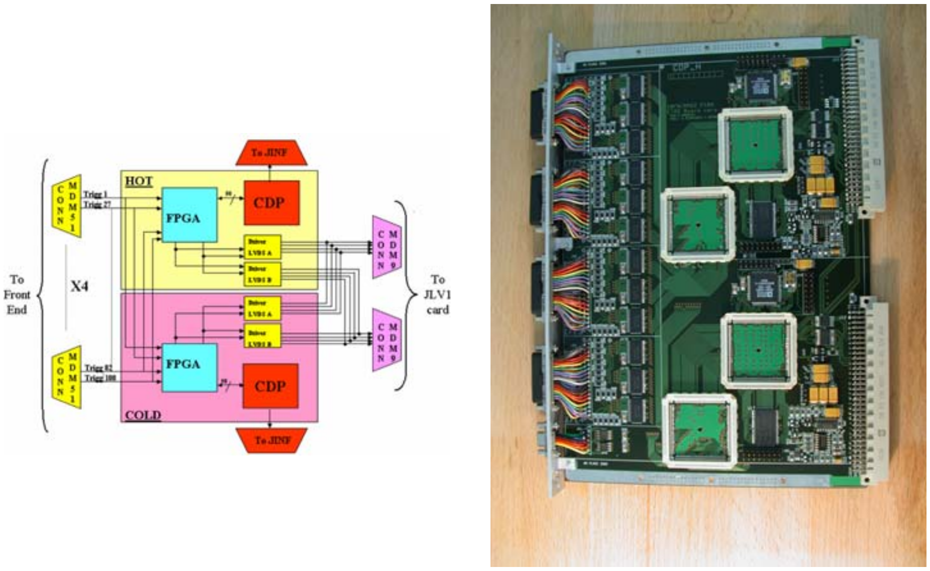

(a) (b)

Figure 5.19: ETRG card. (a) The two identical redundant parts are provided of a FPGA to compute the trigger algorithm and a common digital part to comunicate with the main AMS-02 DAQ system. (b) The engineering module used in functional tests.

50 MHz clock. According to the scheme presented in Fig. 5.20, the digitalized dynode signals are continuosly sampled and stored in the FF1 registers. If some pulses arrive, the Fast algorithm is applied by means of combinatorial logic calculations and the result sent to FF2. When the Fast trigger is passed, the output of FF2, shaped as a 260 ns pulse (XF), is immediately sent to the JLV1 card. The same output is also used to start the next phase of the trigger decision, the ECAL level 1 signal generation (XA). This kind of system architecture prevents problems linked to noisy channels: if FF1 registers are set "high" by few uncorrelated pulses, they are again put down to zero in few clock cycles.

After a programmable delay (DELAY1), inserted to wait the late-comer dynode signals (to overcome the time spread problem), the FF1s' status is frozen and a finite state machine (FSM) can begin data processing. The FSM is required to the COG for superlayers in serialized mode, to combine the information through combinatorial logic and finally to generate the XA signal. This is sent as a 300 ns pulse to JLV1, where the informations of the two ECAL view are combined to form the not-charged LV1 trigger.

The board reset is obtained in two ways depending on the value of XF and gloabal AMS-02 LV1. When only XF is generated and no LV1 signal arrives from

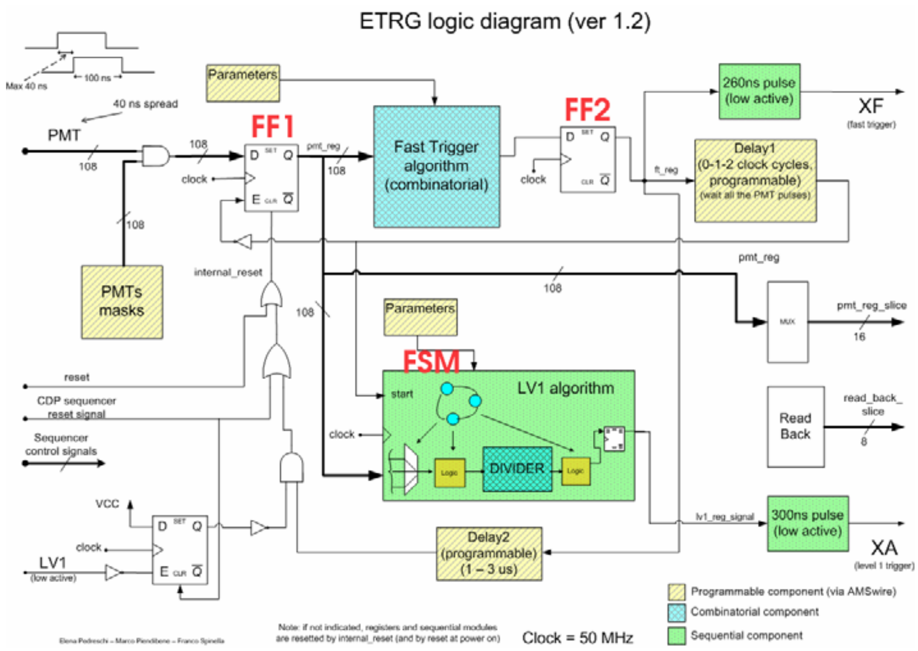

Figure 5.20: Logic scheme implemented in the FPGA of the trigger board.

the main DAQ in the time interval "DELAY2", the FF2 output clears all the FF1 registers and the ETRG is again ready for acquisition. Otherwise the reset signal is given by the CDP sequencer after all data have been transferred.

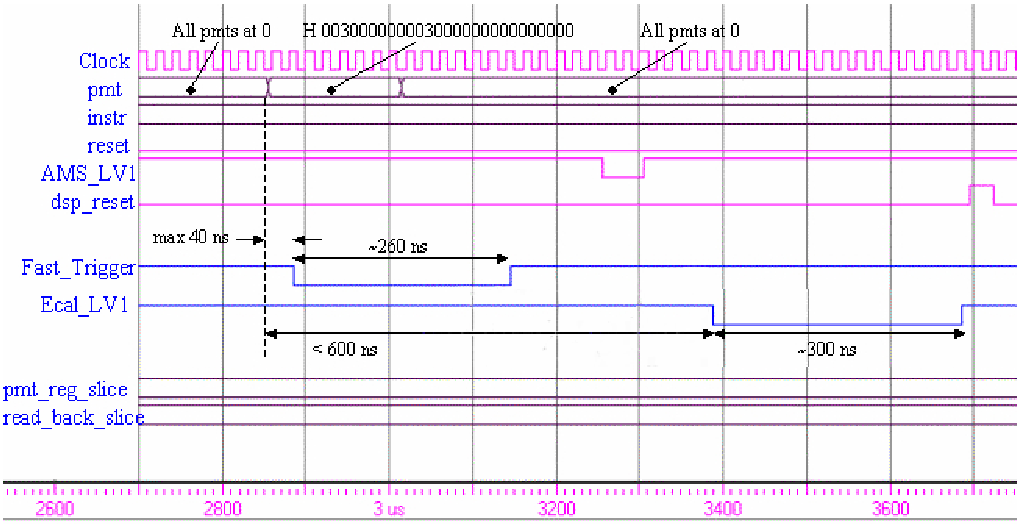

Figure 5.21: ETRG timing simulation. The XF signal is produced within 40 ns while XA requires ∼ 600 to be generated.

According to the timing simulations (Fig. 5.21), the XF signal is produced with a maximum delay of 40 ns. Adding 40 ns delay generated bycables, the time interval between the photon transit in ECAL and the arrival of the Fast trigger in JLV1 is estimated to be $\sim$ 170 ns. The XA follows after less than 560 ns, well within the 650 ns budget.

Chapter 6

Background rejection

A quantitative study of the background rejection power achievable with the AMS-02 *single photon* detection mode, is presented in this chapter. The identification of γ-rays is performed following a procedure organized in four steps:

1. a dedicated analysis software reconstructs the events in ECAL and measures the foundamental parameters of the shower;
2. an angular cut on the trajectory direction selects only events that pass inside the AMS-02 sensitive volume;
3. in the calorimeter, the Fisher analysis is used to classify particles according to the values of a set of four variables describing the shape of the shower. Events whose shower doesn't match the characteristics of an electromagnetic one, are not allowed to go on;
4. events are rejected if the signature of a charged particle is found somewhere in the subdetectors other than the calorimeter.

6.1 Definition of efficiency and contamination

Let N^{γ} be the number of events in a Monte Carlo sample representing the signal to be studied and N_C^{γ} be the number of events out of N^{γ} identified as clean signal by a certain set of selection cuts, C. Then the efficiency on a MC photon sample of energy E_i is defined as:

$$\varepsilon_C(E_i) = \frac{N_C^{\gamma}(E_i)}{N^{\gamma}(E_i)} \tag{6.1}$$

The rejection power of the selection criteria was evaluated calculating both the residual fraction of MC events survived to the cuts, N_C^p/N^p, and the mean proton contamination, η^p_C. In particular the latter quantity provides a more detailed information about the amount of background that will affect the signal detection, since it is related to the real cosmic proton spectrum and it doesn't depend on the spectrum of the MC proton samples. The mean contamination is defined as follows:

$$\eta^p_C = \frac{\sum\limits_i R^p_C(\Delta P_i)}{\sum\limits_i R^p(\Delta P_i)} \tag{6.2}$$

where, using the same notation of Eq. 5.3, $R^p(\Delta P_i)$ is the contribution of the i-th bin in momentum to the background rate; R^p_C is the contribution of the $N^p_C(\Delta P_i)$ events out of $N^p(\Delta P_i)$, i.e. events misinterpreted as signal events.

Note that, wherever non differently specified, the performance of each cut in terms of $\varepsilon_C(E_i)$, N^p_C/N^p and η^p_C, are always referred to the distribution of events survived to all the previous selections.

6.2 Analysis software

The "EcalHit" block, provided by the official AMS-02 reconstruction program, gives the lowest level description of the interaction of an incident particle with the calorimeter. When a cell is involved in the interaction process, its coordinates and an estimate of the amount of energy released by the particle are stored in a EcalHit. The signal read-out chain of the calorimeter is fully simulated. The energy deposited in the scintillanting fibers of the cell, given as output by the Monte Carlo code, is first converted into a light signal and corrected for the attenuation length of the fibers measured on beam test data; then it is transformed into a charge signal considering the quantum efficiency and the gain of the PMTs; finally it is digitalized, selecting one of the two amplification channels of the FE electronics. All the read-out channels are considered as perfectly equalized. The conversion from the digital output (called "visible energy") to the real amount of energy lost by the particle is obtained by a calibration factor suitable for leptonic events.

Starting from the EcalHits, an analysis software was developped reconstructing the events by grouping the calorimeter hits in showers. The ECAL "stand alone" trigger algorithm is implemented in the code, simulating the last dynode signal of each PMT as the sum of the outputs of the four anodes. Only events that pass the trigger are analyzed.

The code applies a cluster searching algorithm among all the fired cells of the calorimeter. At the beginning the cells of each layer are clustered around those points where the highest energy deposits are occurred. Then the clusters of the layers belonging to the same view are paired together using both a criterion of proximity and a criterion of least difference in energy; in addition the alignment of the centrum of gravity of the clusters is checked by a linear fit. At the end, the results for the X and the Y view are combined using again a criterion of the least difference in energy and the clusters are grouped together to form a 3-dimensional shower.

Only events producing one and only one shower in the ECAL are selected for the next steps of the analysis. This is done either to eliminate events with a too small amounts of energy depositions to reconstruct a shower, either to reject hadrons that, unlike leptons, can produce various subshowers. Fig. 6.1 shows how the single shower request affects the efficiency for photons. At 1 GeV energy it falls down to about 85 %. The 77 % of protons, accepted by the LV1 trigger, survive to the selection criterion.

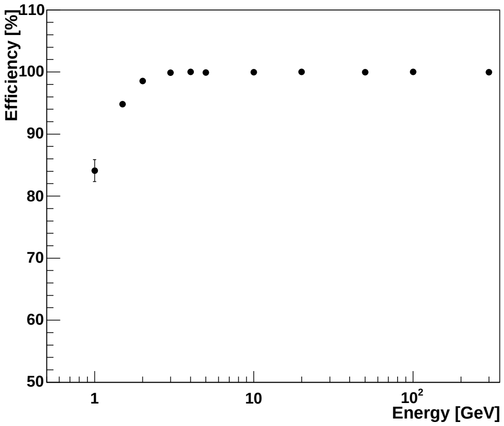

Figure 6.1: Clustering algorithm efficiency for photons.

Whenever a shower is found in ECAL, its relevant parameters are measured. Among these, the analysis software looks for the center of gravity of the energy deposit (COG), the coordinates of the impact point, the direction of the axis of the shower and calculates the total amount of released energy eventually applying corrections for lateral and rear leakages.

6.3 Particle incoming cone: the $A_{TOF/Cone}$ cut

A precise determination of the incoming direction of the particles, based on the good tracking capability of ECAL, can be very useful to eliminate those events that enter the calorimeter outside the TOF acceptance. A raw estimation of the particle direction is already done as selection criterion in LV1 “stand alone” ECAL trigger. Nonetheless the full reconstruction program, elaborating data from all the fired cells, gives a finer description of the electromagnetic shower structure allowing to achieve a much better angular resolution.

In the present analysis the complex geometrical layout of the TOF paddles is schemed as two 70 cm side square surfaces located above ($z = +65.5\,\mathrm{cm}$ in the AMS-02 reference frame) and below the superconducting magnet ($z = -65.5\,\mathrm{cm}$).

Due to the finite angular resolution of the instrument, more than one trajectory direction is allowed for the incident particle. Under the assumption of negligible errors on the reconstruction of the impact point, the set of all the possible directions is confined in a “incoming cone”. The vertex of this cone corresponds to the impact point of the particle, while the opening angle is individuated as two times the value of the angular resolution of the detector evaluated at the energy of the particle. For each event, the analysis code sets the parameters of the incoming cone and computes its intersection area with the upper and the lower TOF planes. Once normalized to the cone cross section for $z = \pm 65.5\,\mathrm{cm}$, the fraction of intersecting area ($A_{TOF/Cone}$) is used to identify photons: only events with a percentage of intersection above a certain threshold are selected.

The efficiency and the fraction of protons passing the angular cut are shown in Fig. 6.2 as a function of the value of the applied threshold; the efficiency is evaluated for photon samples of different energies. An intersection percentage with the upper TOF plane $> 95\,\%$ ensures an efficiency $> 90\,\%$ for photons at energies above 50 GeV, with a residual fraction of protons of about 15 %. Below 50 GeV, the photon efficiency goes rapidly down. To avoid this effect and try to recover efficiency also at low energies, a slight dependence of the cut value on energy was introduced, as show in Fig. 6.3 (a). The parametrization of the cut value applied to the $A^{up}_{TOF/Cone}$ as a function of energy was:

$$A^{up}_{TOF/cone}\,\mathrm{cut} = 97.7(1 - 0.95e^{-0.092E}) \tag{6.3}$$

For the lower TOF, there is no sensible dependency on energy. A cut on the intersection $A^{low}_{TOF/cone} > 90\,\%$ ensures an efficiency of 98 % at all the energy, while more than 50 % of the protons are eliminated.

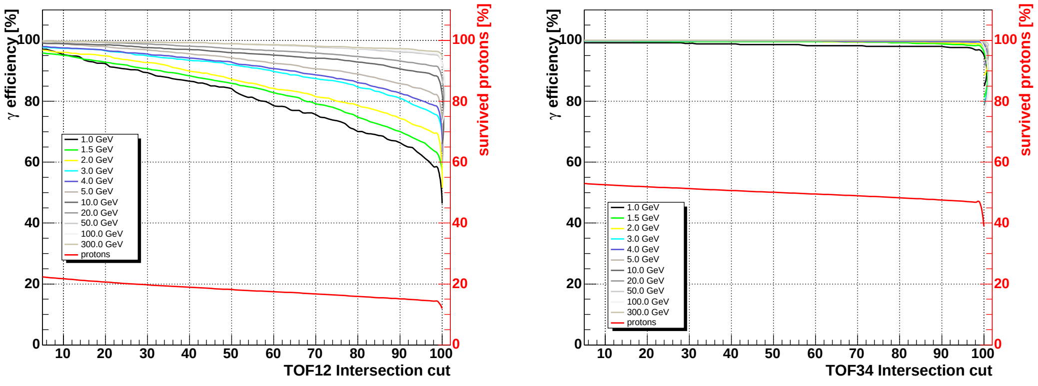

(a) (b)

Figure 6.2: Efficiency and N_C^p/N^p ratio for the $A_{TOF/Cone}$ selection criterion. A cut is applied on the intersection percentage between the “incoming cone” and the TOF planes; results for the upper (a) and for the lower (b) TOF are shown.

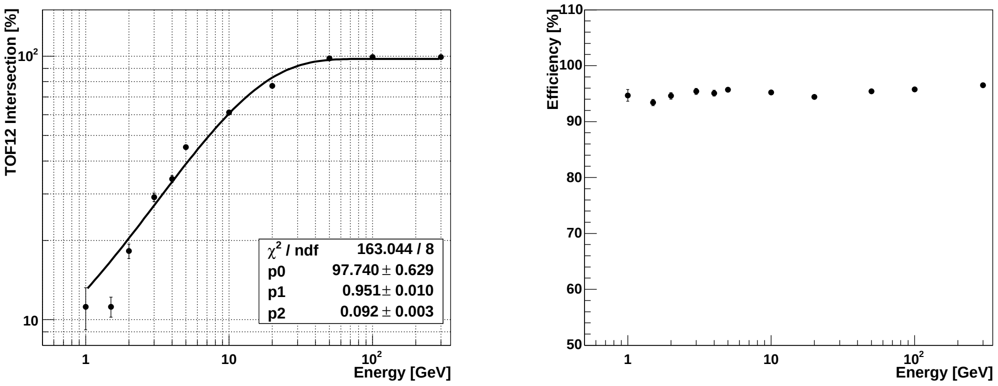

(a) (b)

Figure 6.3: (a) Energy dependence chosen for the upper TOF intersection cut. (b) Efficiency of the angular cuts on lower and upper TOF planes, applied sequentially on photon samples.

In the background rejection study, proton and photon samples were selected applying sequentially both the previous cuts. Fig. 6.3 (b) shows the final γ efficiency given by the two sequential cuts which is about 95 % for all the energy. The proton contamination is 27 %.

6.4 ECAL selection criteria

The purpose of these cuts is the exploitation of the difference between hadronic cascades and electromagnetic showers. These differences rely on the different energy loss mechanisms occuring inside the two kind of showers.

A high energy photon impinging on a thick absorber, gives rise to a cascade of electrons, positrons and photons generated by an iterative sequence of bremsstrahlung and pair production processes. The shower developes and reaches its maximum, characterized by the largest number of particles, when the average energy per particle becomes low enough to suppress further multiplication. From this point, the shower decays slowly through inonization losses for $e^{\pm}$, or by Compton scattering for photons. The high energy part of the cascade determines both the longitudinal and the lateral profile of the shower, therefore, the length characterising it is the radiation length of the medium (X_0).Theoretical models can predict the properties of a e.m. shower with a high degree of accuracy just in terms of the energy of the initial particle and of the number of crossed radiation lengths. This is much less likely to happen with the hadronic showers.

The hadronic showering process is dominated by a succession of inelastic hadronic interactions between the cascade's particles and the nucleons in the material. Since these interactions have many different final states, a great variety of secondaries, like pions and nucleos, and many kind of interaction processes are possible. Moreover, most of the detectable energy arises from π^0's that rapidly decay into photons. A fraction of the incident energy is converted into an electromagnetic core inside the hadronic shower, but, in extreme cases, the large statistical fluctuations of the number of π^0's lead to hadronic showers which develop in a way indistinguishable from electromagnetic showers or, on the opposite extreme, with a negligible electromagnetic component. For these reasons, it's extremely difficult to give a precise parametrization of the shape of the hadronic shower. The 95 % longitudinal containment, on the average, occurs at a depth:

$$t_{95\,\%} = t_{max} + 4E^{0.15}\lambda, \text{ with E in GeV} \tag{6.4}$$

where $t_{max} \approx [0.6log(E) - 0.2]\lambda$ and λ, called the interaction length, is the mean free path of the incident particle for inelastic nuclear interactions in the medium. The 95% radial containment is reached in a cylinder of radius $R_{95\%} \simeq \lambda$. Again, both these values are subjected to a large fluctuations.

Since λ and X_0 are the characteristic length scales of the hadronic and the e.m. showers, the best way to amplify the differences is to choose a material that maximizes the ratio λ/X_0. In ECAL, where the lead is used as passive absorber, the interaction length for the protons is more than 30 times longer than the radiation length, being $X_0 \sim 1\,\mathrm{cm}$ and $\lambda \sim 33\,\mathrm{cm}$[1]; this implies that e.m. showers are narrow and contained over a short distance, while protons tend to interact in the rear part of the calorimeter and their cascades have a wide lateral spread (Fig. 6.4).

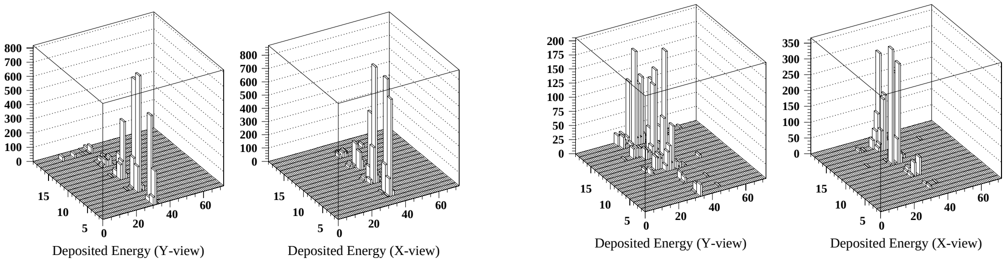

(a) (b)

Figure 6.4: Electromagnetic vs hadronic shower shape in ECAL: a shower generated by a 10 GeV electron impinging perpendicularly on the calorimeter (a) and by a 120 GeV proton (b). Data collected at 2002 CERN beam test.

Taking advantage of the very good imaging capability of the detector, that allows a detailed description of the shape of the showers, it is possible to set four efficient selection criteria, related to the lateral and the longitudinal dimesions of the showers.

6.4.1 Shower transverse profile: the $\mathrm{E}_{2MR}/\mathrm{E}_{tot}$ cut

The transverse development of the electromagnetic showers in different materials scales fairly accurately with the *Molière radius* R_M, given by:

$$R_M \simeq X_0 \frac{21\ MeV}{E_C\ [MeV]} \tag{6.5}$$

where, for ECAL, $E_C \simeq 9.6\ MeV$, so that $R_M \simeq 2\ cm$. On average, only 10% of the energy lies outside a cylinder with radius R_M [72].

For each event the fraction of energy ($\mathrm{E}_{\mathrm{2MR}}$) deposited in a cylinder with $2R_M$ radius centered around the reconstructed shower axis respect to the total energy deposit $\mathrm{E}_{\mathrm{TOT}}$. In ECAL, 1 Moliere radius corresponds to about 2 cells.

---

[1] The probability of interaction for perpendicular protons in ECAL has been measured as $P = 1 - e^{-T/\lambda_I} \sim 40\,\%$, where T is the thickness of the calorimeter.

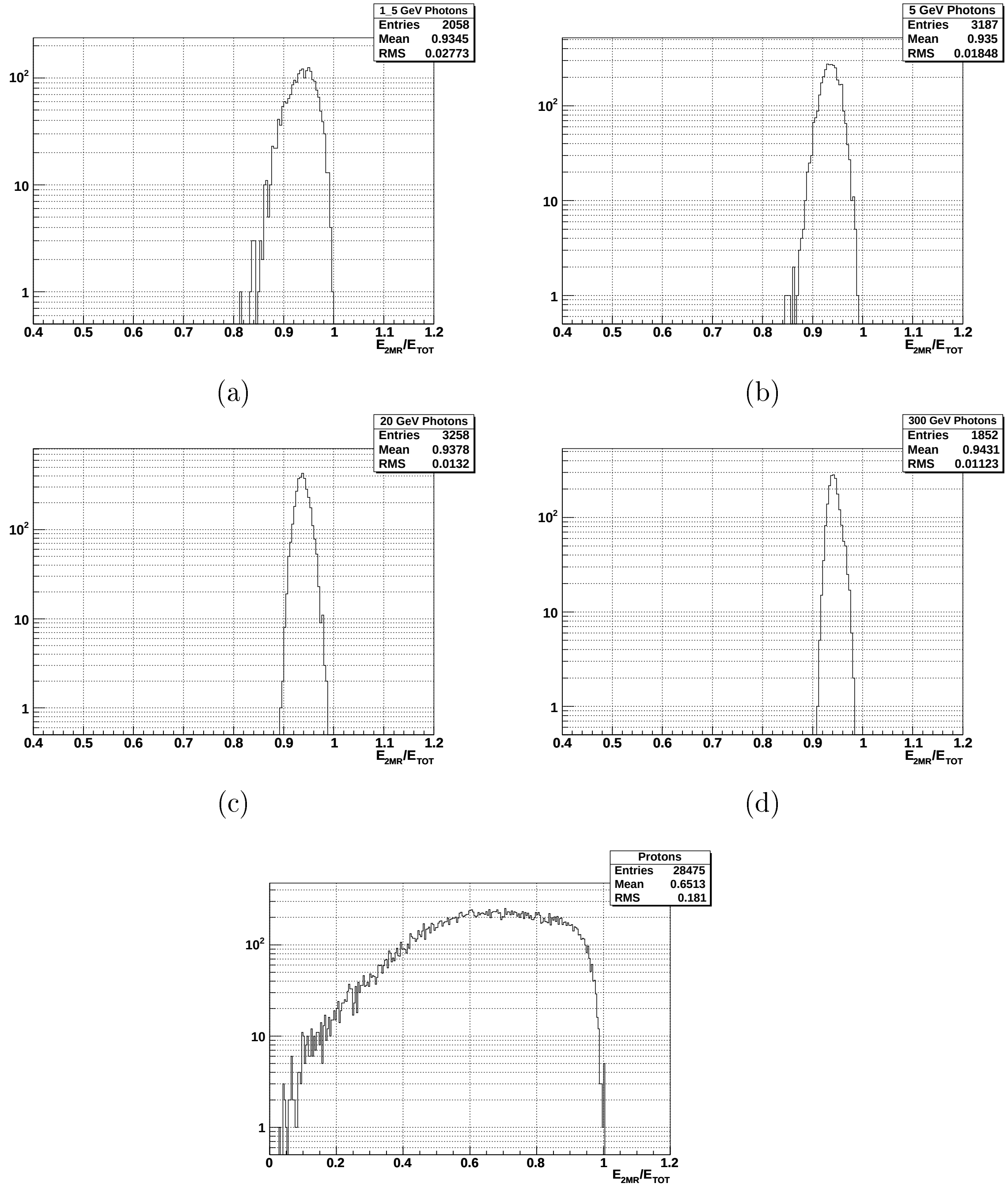

(a) (b) (c) (d) (e)

Figure 6.5: Distribution of fraction of energy contained in a 2 Molier Radius cylinder for 1.5 (a), 5 (b), 20 (c), 300 GeV (d) photons and protons (e).

The distributions of the $\mathrm{E_{2MR}/E_{TOT}}$ fraction for photons at 1, 5, 20, 300 GeV and protons are shown in Fig. 6.5. The broader distribution for protons reflects the different mechanism of interaction as well as the less accurate reconstruction of the direction of the axis of the hadronic showers with respect to the e.m. showers.

The signal identification is obtained requiring the ratio $\mathrm{E_{2MR}/E_{TOT}}$ to be above a certain threshold percentage. In Fig.6.6 (a) the efficiency and the contamination of protons in the photon sample are evaluated as a function of the applied cut. A threshold at 91 % ensures a photon efficiency > 90 % with a N^p_C/N^p fraction of about 8 %.

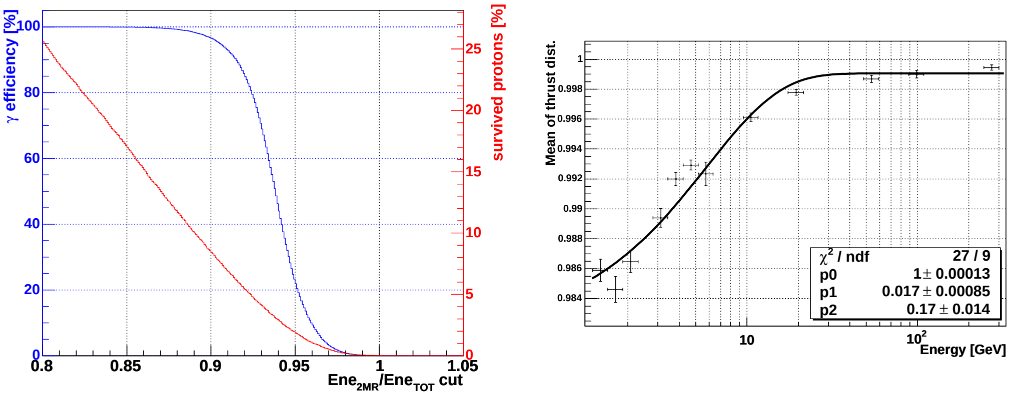

(a) (b)

Figure 6.6: (a) Efficiency (red line) and N^p_C/N^p ratio (blue) of the $\mathrm{E_{2MR}/E_{TOT}}$ selection criterion as a function of the threshold percentage. (b) Fit of the mean values of T, over the photon samples, as a function of the total energy deposited in ECAL.

6.4.2 Shower collimation: the thrust cut

Of the various event shape estimators, the thrust (T) is one of the most widely-used to determine jets direction and collimation in accelerator physics experiments. The thrust is defined as:

$$\mathrm{T} = \mathrm{Max}\frac{\sum_i |\hat{\boldsymbol{n}} \cdot \boldsymbol{p}_i|}{\sum_i |\boldsymbol{p}_i|} \tag{6.6}$$

where the sum is over all final-state particles i with momentum $\boldsymbol{p}_i$ and the maximum is with respect to the direction of the versor $\hat{\boldsymbol{n}}$ (the thrust axis). The allowed range is $1/2 \leq \mathrm{T} \leq 1$, with highly forward collimated events corresponding to Thrust$\simeq 1$ and broad events to Thrust$\simeq 1/2$.

In an electromagnetic shower, particles are distributed with axial symmetry around the primary particle direction. Starting from this idea, in [48] the original thrust method was adapted to the ECAL analysis. In Eq. 6.6 the sum is over the hitted cells and the momentum $\boldsymbol{p}_i$ is replaced by the "pseudo-momentum" $\boldsymbol{v}_i$ with direction given by the line joining the shower impact point to the cell i and magnitude equal to the energy deposited in the cell.

Fig. 6.6 (b) shows the average values of the thrust distributions for the photons sample as a function of the total energy deposit in ECAL. The dependency from the energy was removed introducing a new variable:

$$\hat{\mathrm{T}} = \frac{\mathrm{T}}{0.99 - 0.017e^{-0.18\mathrm{E}_{\mathrm{TOT}}}} \tag{6.7}$$

The distributions of $\hat{\mathrm{T}}$ for photons at 1, 5, 20, 300 GeV and protons are shown in Fig. 6.7. As expected, due to the higher collimation around the axis of the e.m. showers, respect to the hadronic cascades, the thrust takes values close to 1 for photons and to lower values for protons. The selection power of the thrust is shown in Fig. 6.8 (a). Requiring $\hat{\mathrm{T}} \geq 0.98$, the photon efficiency is about 90 % and the residual proton fraction is 10 %.

6.4.3 Shower transverse profile: the footprint cut

The surface covered by the "footprint" of an electromagnetic shower is smaller than for a hadronic shower. In ECAL it's possible to obtain a measure of the area of the footprint by computing the determinant of the "inertia tensor" of the deposited energy relative to the shower COG. For each orthogonal view of the calorimeter, the tensor is defined as:

$$I_j = \begin{bmatrix} \sigma_j^2 & \sigma_{jz} \\ \sigma_{jz} & \sigma_z^2 \end{bmatrix} \tag{6.8}$$

where $j = x, y$. Let $\boldsymbol{c}_i = [c_x^i, c_y^i, c_z^i]$ be the coordinates of the i-th cell in the AMS-02 reference frame, and $\boldsymbol{b} = [b_x, b_y, b_z]$ the coordinates of the centrum of gravity; then the matrix elements are computed as:

$$\sigma_j^2 = \frac{\sum\limits_{i=1}^{ncell} (c_j^i - b_j)^2 E_i}{\sum\limits_i E_i} \quad , \sigma_{jz} = \frac{\sum\limits_{i=1}^{ncell} (c_j^i - b_j)(c_z^i - b_z) E_i}{\sum\limits_i E_i} \tag{6.9}$$

where E_i is the energy deposit in the i-th cell and the sum is made on all the cells associated to the shower according to the clustering algorithm.

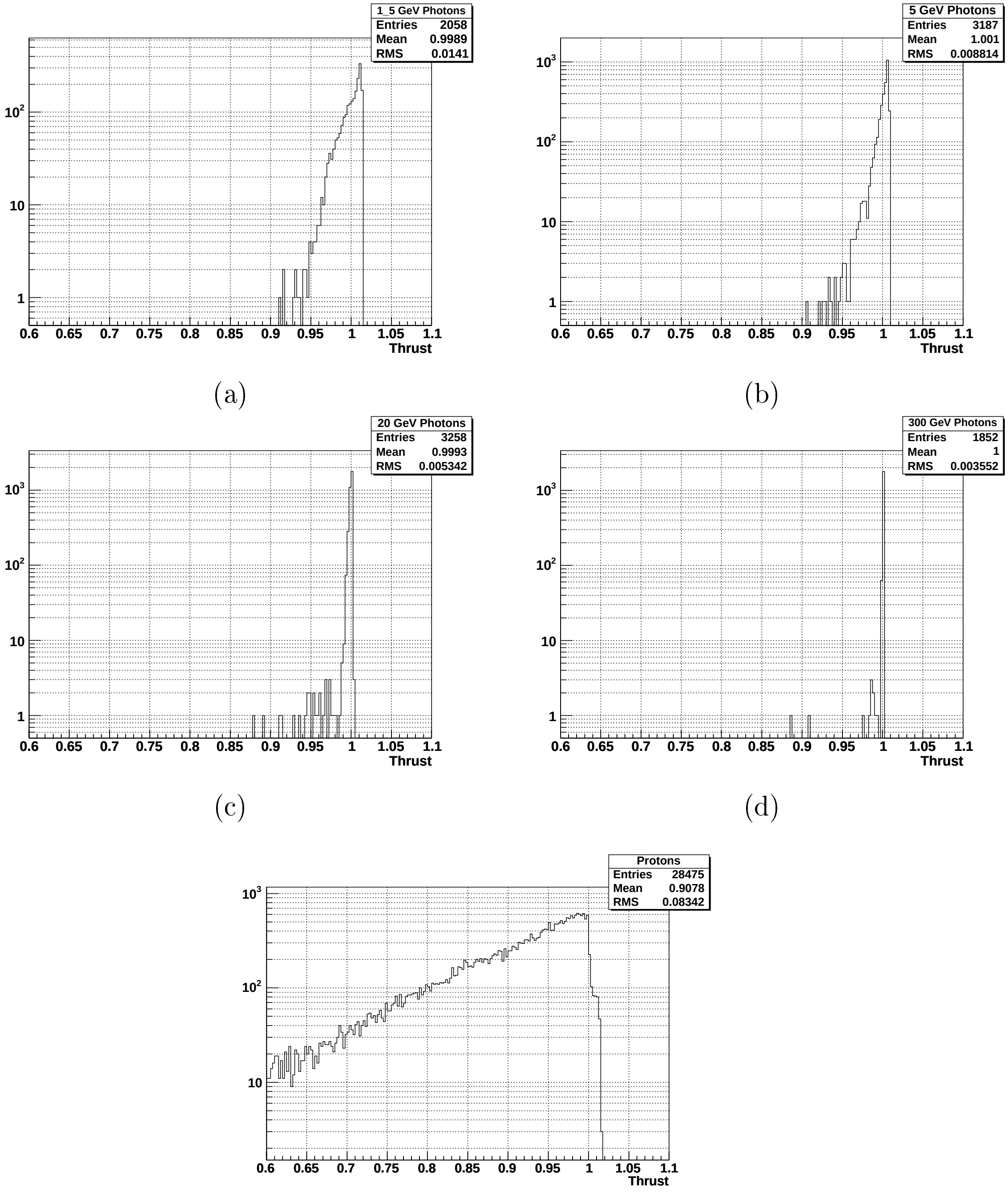

(a) (b)

(c) (d)

(e)

Figure 6.7: Distribution of the thrust ($\hat{T}$) estimator for 1.5 (a), 5 (b), 20 (c), 300 GeV (d) photons and protons (e).

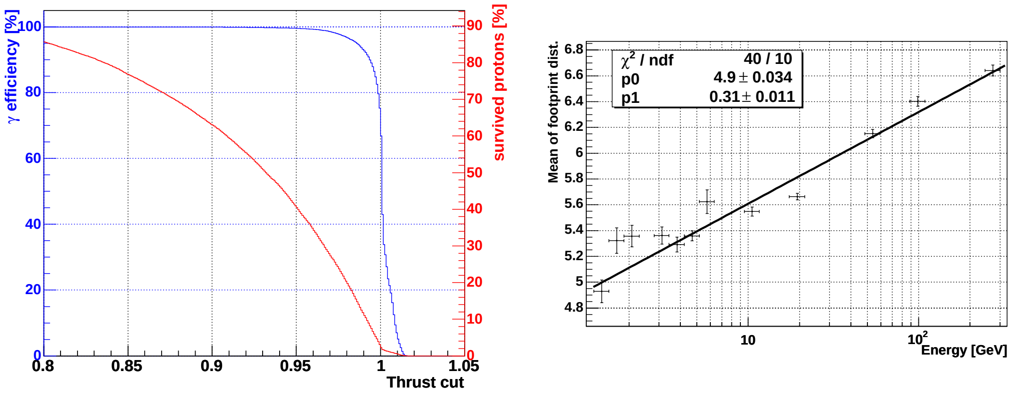

(a) (b)

Figure 6.8: (a) Efficiency (red) and N_C^p/N^p ratio (blue) of the $\hat{\mathrm{T}}$ selection criterion as a function of the applied cut. (b) Fit of the mean values of $\mathrm{S_{FP}(E)}$, over the photon samples, as a function of the total energy deposited in ECAL.

Combining the information of both X and Y view, a measure of the area covered by the shower can be estimated as:

$$\mathrm{S_{FP}(E)} = \sqrt{\det(I_x)} + \sqrt{\det(I_y)} \tag{6.10}$$

This quantity shows a logarithmic dependecy from energy (Fig. 6.8 (b)). The average values of the shower footprint for photons were fitted and the energy dependency removed:

$$\hat{\mathrm{S}}_{\mathrm{FP}} = \frac{\mathrm{S_{FP}(E)}}{4.9 + 0.31 \cdot Log(x)} \tag{6.11}$$

In Fig. 6.9, the distributions of $\hat{\mathrm{S}}_{\mathrm{FP}}$ for photons of 1.5, 5, 20 and 300 GeV are compared to the proton distribution. As expected the electromagnetic showers footprint is narrower than for the hadronic showers. An idea of the discrimination power of the variable is given in Fig. 6.10, where the fractions of events with an area below a fixed threshold are reported.

6.4.4 Shower longitudinal profile: the longitudinal χ^2 cut

For photons having the same energy, the mean of the distribution of the energy signal collected in each layer is almost univocally set by the position in depth of the layer relative and by the energy of the particle. The main source of dispersion relies on the differences in the incident direction of the photons. For a fixed z coordinate, as the angle between the trajectory and the calorimeter changes, the length of the

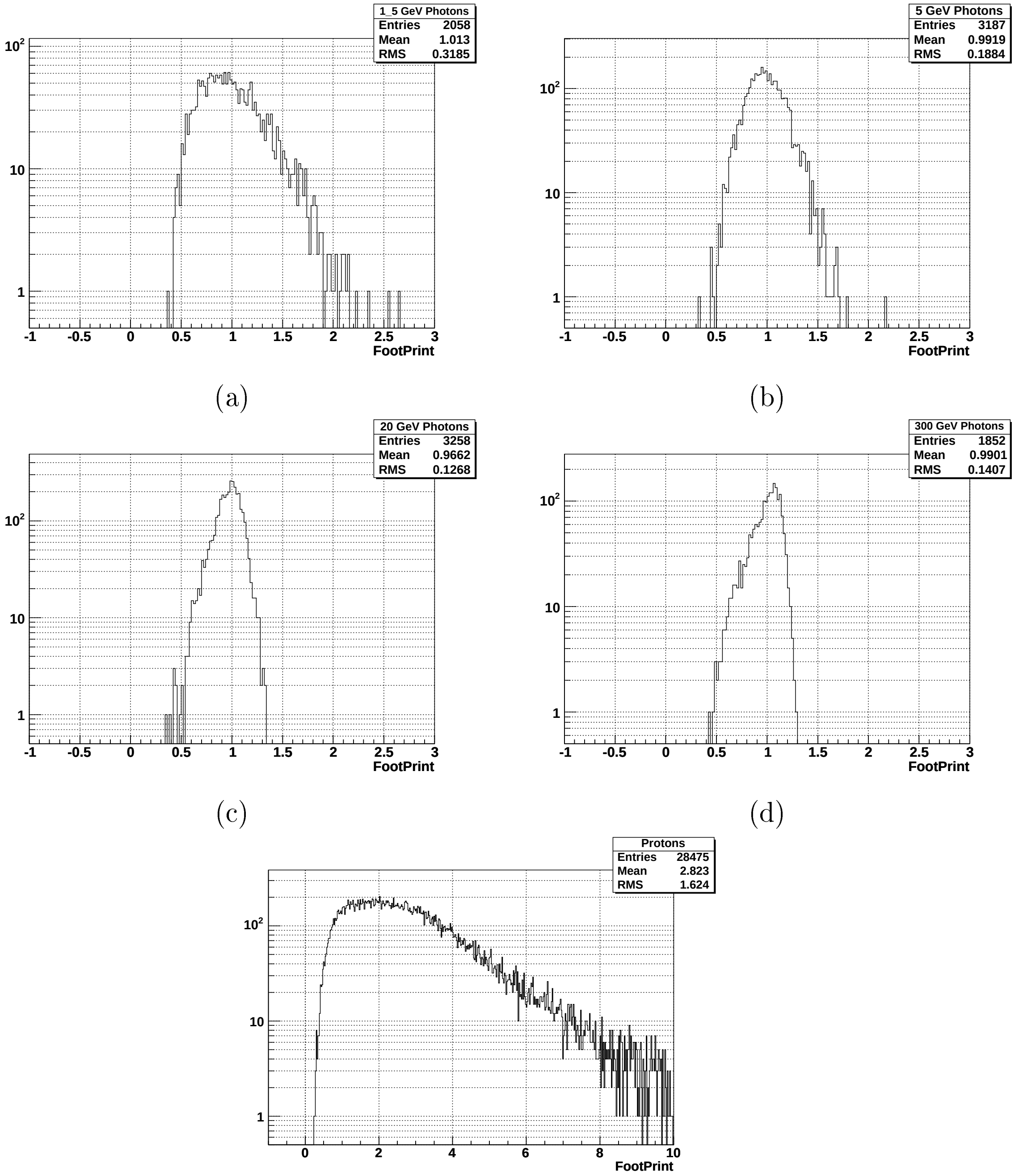

(a) (b) (c) (d) (e)

Figure 6.9: "Footprint" distribution for 1.5, 5, 20, 300 GeV photons.

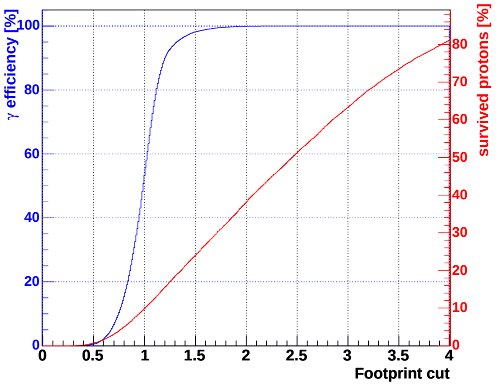

Figure 6.10: Efficiency (blue) and N^p_C/N^p ratio (red) of the $\hat{\mathrm{S}}_{\mathrm{FP}}$ selection criterion as a function of the applied cut.

path of the particle in the detector changes too and so does the number of crossed X_0. Since the ECAL aperture angle is limited to ∼ 20°, the distribution of the energy deposited in each ECAL layer is expected to be strongly peaked around the mean value (see Fig. 6.11). On the contrary, hadronic showers show very large fluctuations in energy deposition, resulting in much wider distributed signals.

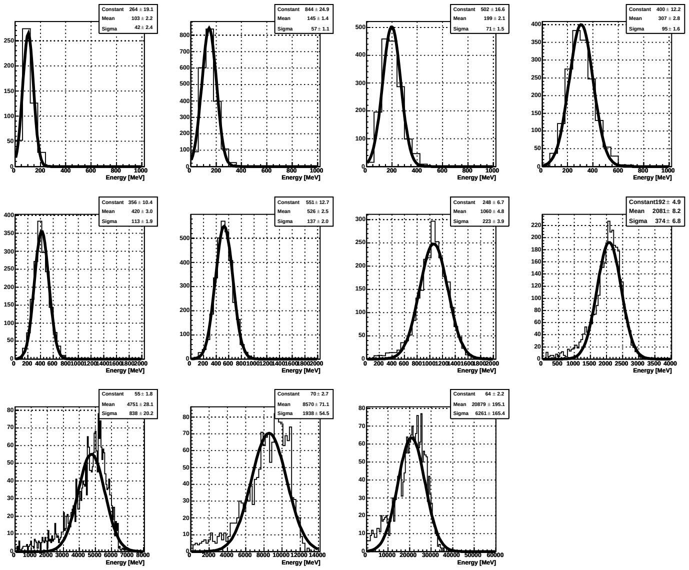

Figure 6.11: Distributions of the deposited energy in the 8-th layer by samples of photons between 1 and 300 GeV. The gaussian fit is used to extract the values of mean and the standard deviation utilized in the χ^2_{long} cut.

The estimator, that better describes this property of the e.m. shower, is a sort of χ^2 of the longitudinal profile. It is defined as follows:

1. for each MC photon sample of energy E_i, the mean $(\langle E^l_{lay}(E_i)\rangle)$ and the standard deviation $(\sigma^l_{lay}(E_i))$ of the energy deposition in the l-th ECAL layer is estimated by a gaussian fit;
2. $\langle E^l_{lay}(E_i)\rangle$ and $\sigma^l_{lay}(E_i)$ were parametrized by fitting their values as a function of the total amount of energy deposited in the calorimeter, E_{TOT} (see Fig. 6.12 (a)). Both the two parametrization functions have the following form:

$$[0] + [1]E_{TOT} + [2]log(E_{TOT}) \tag{6.12}$$

3. event by event, the value χ^2_{long} is obtained comparing the signal in each layer to the mean value $\langle E_{lay}(E_{TOT})\rangle^l$ of the distribution:

$$\chi^2_{long} = \frac{1}{15}\frac{\sum_{l=1}^{18}(E^l_{lay} - \langle E^l_{lay}(E_{TOT})\rangle)^2}{\sigma^l_{lay}(E_{TOT})} \tag{6.13}$$

4. the dependency of χ^2_{long} from the energy of the photons, is removed defining a new estimator $\hat{\chi}^2_{long}$:

$$\hat{\chi}^2_{long} = \frac{\chi^2_{long}}{23.4 + 22.7 \cdot \mathrm{E_{TOT}}^{1.05}} \tag{6.14}$$

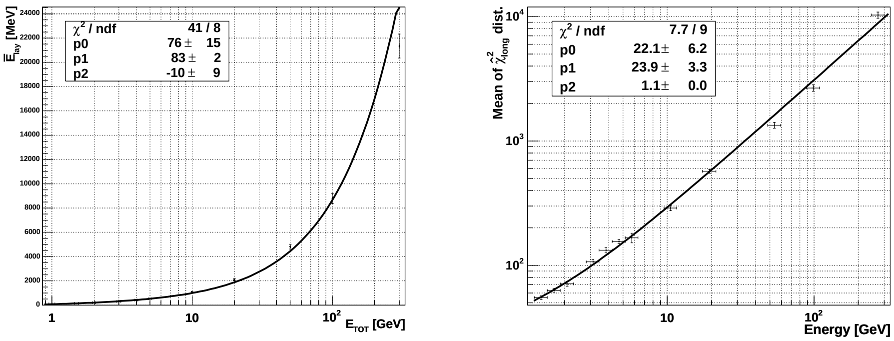

(a) (b)

Figure 6.12: (a) The fit of the $\langle E_{lay}(E_{TOT})\rangle$ function for the 8-th ECAL layer. (b) Fit of the mean values of χ^2_{long}, over the photon samples, as a function of the total energy deposit.

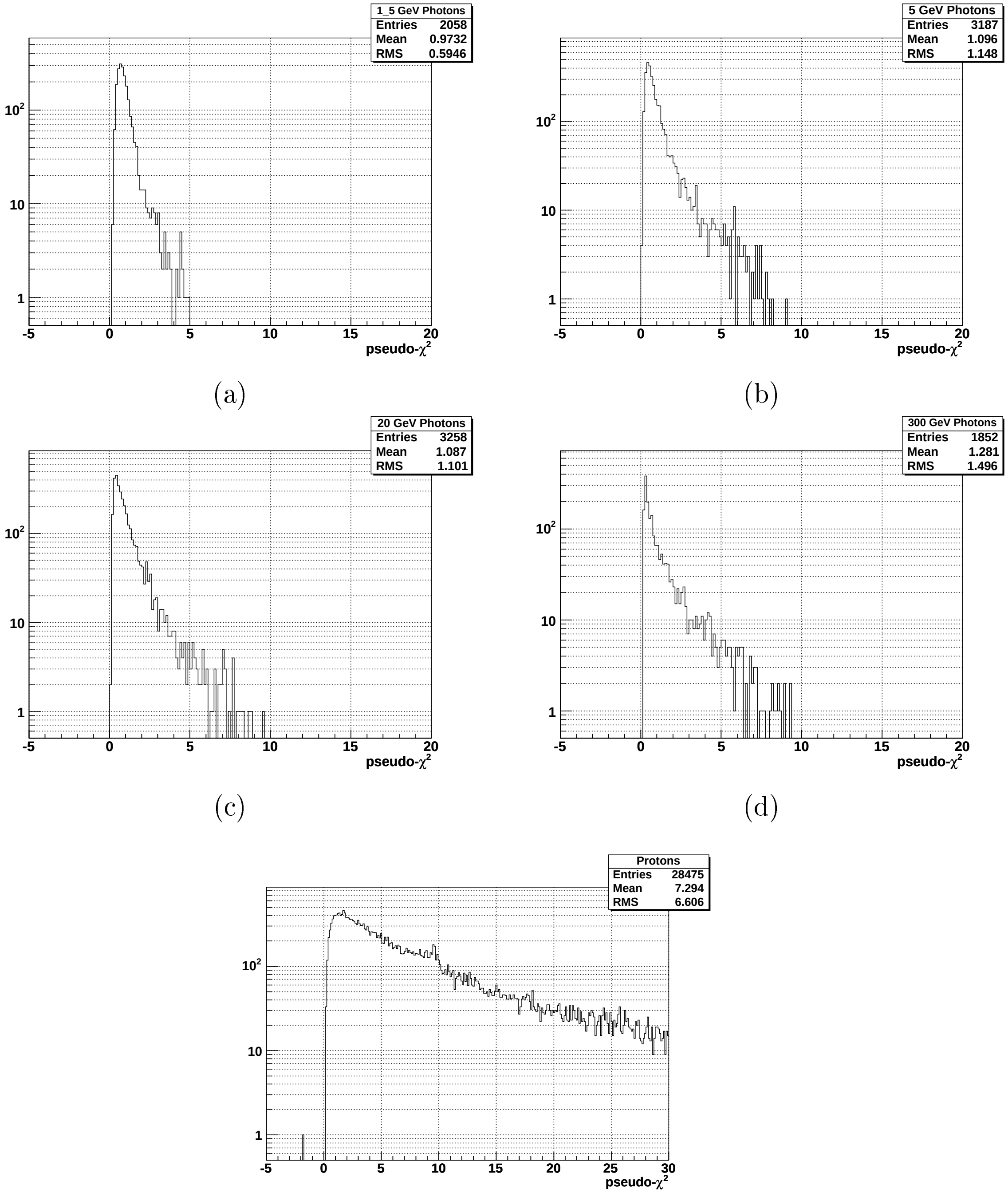

(a) (b) (c) (d) (e)

Figure 6.13: Distribution of $\hat{\chi}^2_{long}$ for 1.5 (a), 5 (b), 20 (c), 300 GeV (d) photons and protons (e).

In Fig. 6.13, the distributions of $\hat{\chi}^2_{long}$ for photons of 1.5, 5, 20 and 300 GeV are compared to the proton distribution. As expected, the values of $\hat{\chi}^2_{long}$ for the protons are higher, since the energy deposited in each ECAL layer is less correlated to the layer position. In Fig. 6.14 the discriminant power of the variable is evaluated applying a cut on the upper values: a $\hat{\chi}^2_{long} < 2.5$ gives an efficiency on the signal of 90 %, while about 70 % of the protons are rejected.

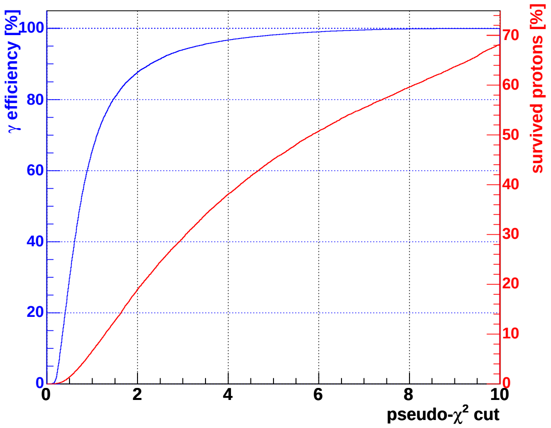

Figure 6.14: Efficiency (blue) and N^p_C/N^p ratio (red) as a function of the cut on the χ^2_{long}.

6.5 e/h discrimination with ECAL selection criteria

A way to employ the estimators described in the previous section, is to carry out the identification of the photons through standard sequential cuts. This method, obviously, doesn't exhaust all the information contained in the four variables, because at least the correlation terms are not taken into account. A possible alternative is given by the application of one of the techniques provided by the multivariate analysis.

A comparison between the performances of the two alternatives is here presented.

6.5.1 Sequential cuts analysis

An event is identified as a photon if the following conditions are simultaneously satisfied:

$$\mathrm{E_{2MR}/E_{TOT}} \geq 0.91 \quad \& \quad \hat{\mathrm{T}} \geq 0.98 \quad \& \quad \hat{\mathrm{S}}_{\mathrm{FP}} \leq 1.2 \quad \& \quad \hat{\chi}^2_{long} \leq 2.5 \tag{6.15}$$

For each discriminating variable, the value of the cut was chosen requiring a photon efficiency of about 90 %. The resulting global efficiency is shown in Fig.6.15; the mean proton contamination, η^p_C, is $3.6 \pm 0.3\,\%$ ($N^p_C/N^p \simeq 6.4 \pm 0.2\,\%$).

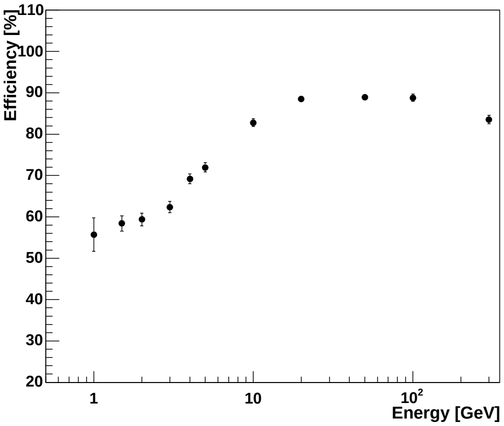

Figure 6.15: Efficiency on signal obtained applying sequentially the ECAL selection criteria.

6.5.2 Multivariate analysis

The problem of distinguishing particles as photons or protons were reduced to a two populations, Π_1 (photons) and Π_2 (protons), multivariate analysis, where the set of the four ECAL selection criteria ($\mathrm{E_{2MR}/E_{TOT}}$, $\hat{\mathrm{T}}$, $\hat{\mathrm{S}}_{\mathrm{FP}}$, $\hat{\chi}^2_{long}$) are treated as the predictor variables $\boldsymbol{x}$.

An a priori choice of the best method, among those used to distinguish between groups of populations in discriminating analysis, is not an easy task since the discriminating power of each tecniques much depends on the shape and on the value of the parameters of the predictors distributions. To get rid of these difficulties, an approch was followed so to firstly select the subset of techniques more suitable for our specific problem, then to optimize each analysis method and finally to choose the one assuring the highest performances.

A summary description of the multivariate analysis tools used in this study is presented in Appendix A. Further information is available in [73], [74]. In general the Fisher linear discriminant analysis and the logistic regression seem to better accomplish the present framework because no assumptions of multinormality of the populations or equality of the covariance matrix are required as for the other linear and quadratic discriminant analysis methods.

In order to tune the analysis algorithms, a subsample of the MC data was used as training sample. About 10000 events among protons and photons were selected randomly, clipping out few events very far out on the tails of distributions ($x > 5\sigma$). At the end of the optimization process, we derived three different discriminating function:

Fisher discriminant analysis. In general the Fisher's prescriptions suggest to compute the discriminant function that maximizes the separation of Π_1 and Π_2 by means of the pooled covariance matrix, defined as the mean of the covariance matrixs of the two populations weighted with the number of observations for each population (Eq. A.10). For the present task, where the signal rate is very low respect to the background, i.e. the cost $C(1|2)$ of a proton recognized as a photon is much higher than the opposite cost $C(2|1)$, the best discrimination was obtained, instead, by replacing the pooled matrix with the photon covariance matrix.

Inserting in Eq. A.15 the mean values $\bar{\boldsymbol{x}}_1$, $\bar{\boldsymbol{x}}_2$ and the covariance matrix S_1, a linear combination of the observed variables was found giving the highest separation:

$$y_F = \boldsymbol{b}_F^\top \boldsymbol{x}$$

where

$$\boldsymbol{b}_F^\top = (760.68, 1079.47, -21.78, -13.15, 3023.07) \tag{6.16}$$

Quadratic discriminant analysis. This rule can be preferred to LDA approach, since it does't require the covariance matrixs to be equal. The mean values $\bar{\boldsymbol{x}}_1$, $\bar{\boldsymbol{x}}_1$ and the covariance matrixs S_1, S_2 were employed in Eq. A.11 to calculate the following discriminant function y_{QDA}:

$$y_{QDA} = -\frac{1}{2}x^T(\Sigma_1^{-1} - \Sigma^{-2})x + (\bar{x}_1^T\Sigma_1^{-1} - \bar{x}_2^T\Sigma_2^{-1})x - \\ \frac{1}{2}\ln(\frac{|\Sigma_1|}{|\Sigma_2|}) - \frac{1}{2}(\bar{x}_1^T\Sigma_1^{-1}\bar{x}_1 - \bar{x}_2^T\Sigma_2^{-1}\bar{x}_1)$$

where

$$-\frac{1}{2}(\Sigma_1^{-1} - \Sigma^{-2}) = \begin{pmatrix} 1981.08 & 36.38 & 88.38 & 0.29 \\ 36.38 & -8179.03 & -78.36 & -10.93 \\ 88.38 & -78.36 & -17.17 & -1.00 \\ 0.29 & -17.17 & -1.00 & -0.58 \end{pmatrix},$$

$$(\bar{x}_1^T\Sigma_1^{-1} - \bar{x}_2^T\Sigma_2^{-1}) = (3835.07, 16483.85, 361.01, 24.65)\,,$$

$$\frac{1}{2}\ln\left(\frac{|\Sigma_1|}{|\Sigma_2|}\right) - \frac{1}{2}(\bar{x}_1^T\Sigma_1^{-1}\bar{x}_1 - \bar{x}_2^T\Sigma_2^{-1}\bar{x}_1) = -10238.73$$

Logistic regression. A dichotomus variable y, dependent on $\boldsymbol{x}$, is defined to be 0 if the particle is a photon and 1 if it is a proton. According to Eq. A.24, fixing $\boldsymbol{x}$ for a specific event, the probability function $\hat{p}$ to have $y = 1$ is given by:

$$\hat{p} = \frac{e^{\boldsymbol{b}_{LR}^{\top}\boldsymbol{x}}}{1 + e^{\boldsymbol{b}_{LR}^{\top}\boldsymbol{x}}}$$

Using the training samples, it was found:

$$\boldsymbol{b}_{LR}^{\top} = (64.13, -39.65, -30.96, 0.72, 0.55) \tag{6.17}$$

The power of the discriminating functions was tested on the whole set of data by classifying each event on the grounds of the $\boldsymbol{x}$ value and comparing the predicted allocation to a group with its true placement. Fig. 6.16 shows the distributions obtained for y_F, y_{QDA} and $\hat{p}_{LR}$ on the protons (red) and photons samples (blue), that passed the $A_{TOF/Cone}$ cut. The mean efficiency on gammas (blue-dot line) and the mean proton contamination (red-dot line), as a function of the threshold value applied, are also reported.

In addition to the efficiency and the contamination, in order to help fixing the values of the cuts, a rough estimate of the signal over square root of the background ratio was also calculated (black-dot line in Fig. 6.16). We supposed, in a non-realistic manner, that AMS-02 will point for a 1 year period the Galaxy inner part from where we expect a γ-rays rate R^{γ}_{cone} of $\sim 6 \cdot 10^{-4}$ Hz after the $A_{TOF/Cone}$ angular cut. As the rate of the background protons R^{p}_{cone} will be ~ 15 Hz, the ratio $S/\sqrt{N}$ can be estimated as:

$$\frac{S}{\sqrt{N}} = \frac{\varepsilon \cdot R^{\gamma}_{cone}\sqrt{T_{obs}}}{\sqrt{\eta^p \cdot R^p_{cone}}} \simeq \frac{0.87\varepsilon}{\sqrt{\eta^p}} \tag{6.18}$$

In Tab. 6.1 the values of ε_C, η^p_C and $S/\sqrt{N}$ for two different sets of cuts are presented: one set was chosen corresponding to the maximum value of the $S/\sqrt{N}$

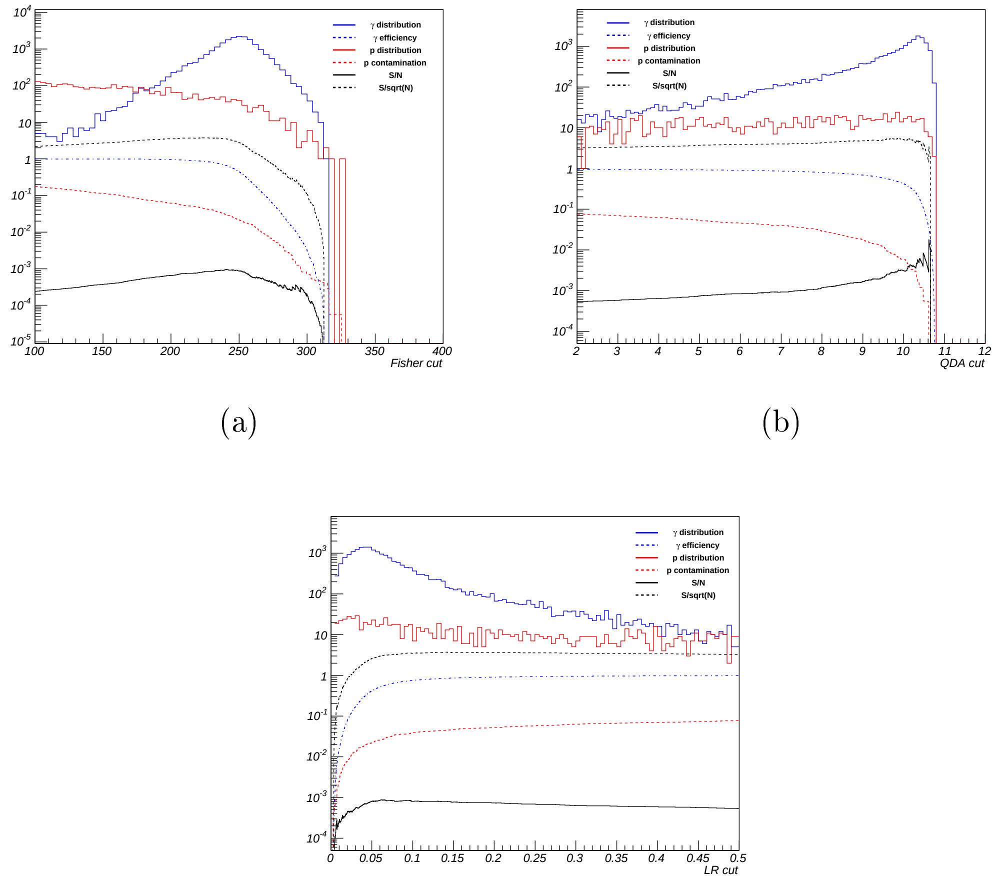

(a)

(b)

(c)

Figure 6.16: Multivariate analysis. Distributions of y_F (a), y_{QDA} (b) and $\hat{p}_{LR}$ (c) for photons (blue) and protons (red). Efficiencies (blue-dot line), contaminations (red-dot), signal to background (black-solid) and signal to square root of background (black-dot) ratios are computed as function of the applied cuts values.

ratio; the other set was obtained requiring a mean photon efficiency of 75 %, i.e. an efficiency comparable to the value of the sequential cuts analysis. According to the results, the y_{QDA} estimator shows the highest rejection power. However, it's easy to understand from Fig. 6.17 that the very low contamination level is achieved by cutting out a big fraction of the events with small energy deposit in ECAL, independently whether or not the particles are photons. Since the background is mostly generated by protons releasing small amount of energy in the calorimeter, their contribution to the total rate, $R_C^p(\Delta E_i)$, becomes very small and so the mean contamination η_C^p. For this reason, the Fisher's estimator must be preferred above the other two variables, since it keeps the efficiency to a reliable level over the whole energy spectrum.

	y_F	y_{QDA}	$\hat{p}_{LR}$
cut	224.7	9.88	0.14
ε_C [%]	85.13	46.99	84.92
η_C^p [%]	4.3	0.6	4.5
$(S/\sqrt{N})_{max}$	3.8	5.5	3.7
cut	234.3	8.54	0.8
ε_C [%]	75	75	75
η_C^p [%]	3.5	2.2	4.0
$(S/\sqrt{N})$	3.7	4.6	3.5

Table 6.1: Discriminating power of y_F, y_{QDA} and $\hat{p}_{LR}$. For each estimator, two different values of cut are reported: the first cut is set equal to the value that maximizes the $S/\sqrt{N}$ ratio, the second is obtained requiring a mean photon efficiency of 75 %.

Compared to the estimated performances for the sequential cuts analysis, the values of $\varepsilon_C(E_i)$, resulting from the application of the Fisher's rule, are similar with only a small increase below 5 GeV and above 100 GeV and a decrease for the points at 10 and 20 GeV. The proton contamination of $3.5 \pm 0.3\,\%$ ($N_C^p/N^p \simeq 6.0 \pm 0.2\,\%$) is compatible inside the errors with the one obtained with sequential cuts.

In conclusion, the Fisher's estimator and the sequential cuts are to be considered equivalent in the present framework. The former tecniques was used to select the events for the next step of our analysis procedure.

6.6 Sub-detectors selection criteria

Beside analysing 3-dimensional shower in ECAL, charged particles can be also identified by rejecting events with a significant signal in the other AMS-02 subdetectors.

Even if non-converted photons cannot give signals in the AMS-02 detector before reaching the calorimeter, other phenomena like noisy channels and backsplash particles may lead to spurious signals. In particular, most of the secondary particles bounced back during the development of the shower in the ECAL, reach the lower planes of the TOF and the tracker; their number decreases when moving move up the whole detector, due to the bending effect of the magnetic field. Apart from that, the amount of backsplash particles increases with the energy of the primary incident on the ECAL.

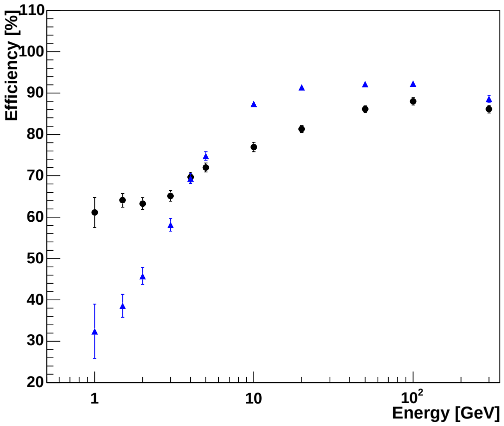

Figure 6.17: Signal efficiency as a function of the MC sample energy for the Fisher's selection criterion (black dots) and for the quadratic discriminant analysis (blue triangles). Both the results are obtained requiring a mean efficiency of 75 %.

In some situations, the spurious signals may confuse the event identification process that would recognize the signature of a charged particle in those signals. A good compromise that allows to solve this problem, consists in limiting the search of hits to an area around the reconstructed trajectory of the incident particle. In our study only signals are taken into account if inside the volume of the "incoming" cone (following for this volume the same definition given in the section 6.3). The trajectory of the particle is obtained by extending the shower reconstructed direction up to the height of each subdetector; the information on the fired channels in the subdetectors is included in the analysis directly from the official AMS-02 reconstruction program without any modifications.

All in all, we defined four variables:

- Cl_{TRD}, the number of clusters that lie within the intersection region between the "incoming" cone and the TRD;
- H_{STD}, the number of hits that lie within the intersection region between the "incoming" cone and the eight planes of the STD;
- H_{TOF}, the number of hits inside the intersection region between the "incoming" cone and the TOF planes;
- H_{RICH}, the number of hits that lie within the intersection region between the Čherenkov light cone and the plane of the PMTs array of the RICH; the vertex of the Čherenkov light cone coincides with the intersection point between the

trajectory of the particle and the Aerogels plane, while the half opening angle is given by $cos\theta = 1/\beta n$, where $\beta = 1$ and $n = 1.04$.

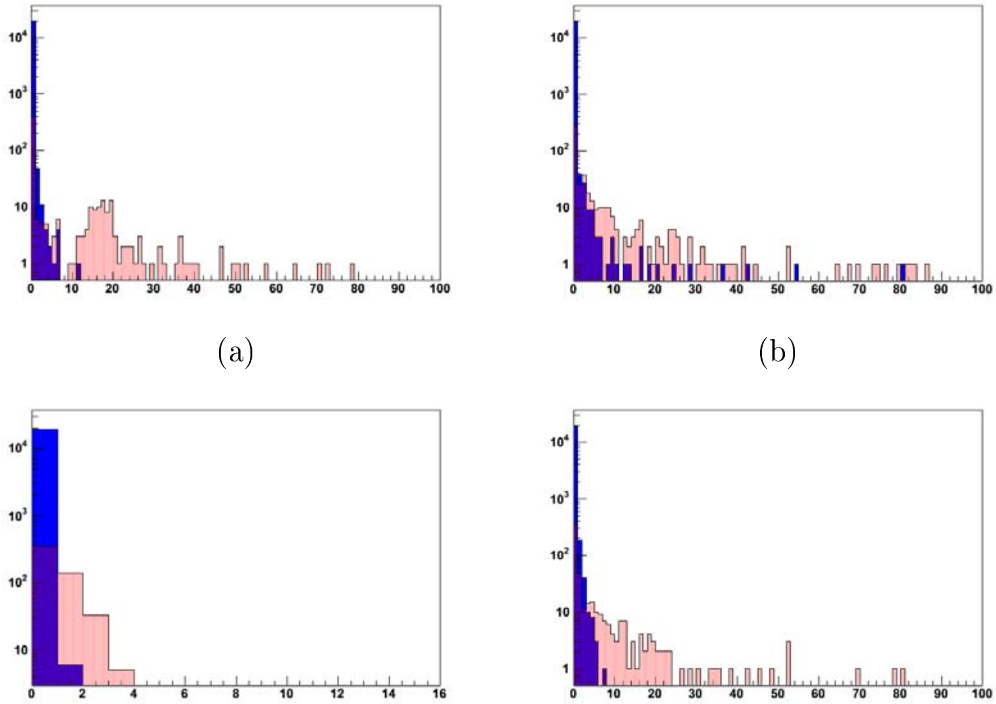

(a) (b)

(c) (d)

Figure 6.18: Distributions of the number of hits collected inside the intersection region between the "incoming" cone and the TRD (a), the TOF (b), the tracker (c) and the RICH (d) for photons (blue) and protons (red).

The distributions of H_{TOF}, Cl_{TRD}, H_{STD}, H_{RICH} for photons and protons are shown in Fig. 6.18. In rejecting protons, all the information given by the four variables was combined in one unique estimator $N_{TOT} = H_{TOF} + ClTRD + H_{STD} + H_{RICH}$. Requiring $N_{TOT} < 1$, we obtained an efficiency greater then $90\,\%$ at all the energies (see Fig. 6.19) and a contamination $\eta_C^p \simeq 42\,\%$ ($N_C/N \simeq 20\,\%$).

6.7 Final results on background rejection

The full procedure for the identification of gamma ray events has been tested on the MC samples. An event passing the ECAL trigger is recognized as a photon if its reconstructed direction is well inside the TOF acceptance, its shower in the e.m. calorimeter satisfies the selection cut applied to the Fisher's discriminating

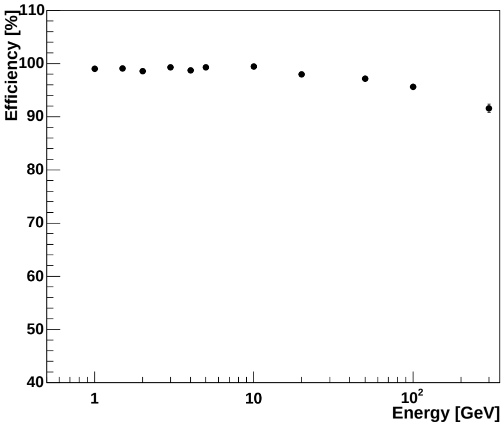

Figure 6.19: Total hits efficiency for photons.

variable and no other signals are detected in the AMS-02 subdetectors in a region around the particle trajectory. The γ efficienies of the final combined selections for incident azimuthal angle θ in the ranges $160° \div 170°$ and $170° \div 180°$ are shown in Tab. 6.2. In Fig. 6.20 (a) is reported the proton contamination as a function of the reconstructed energy. The errors on the points are calculated according to the so far collected MC statistics. A global contamination factor of $3.2 \pm 0.5 \cdot 10^{-3}$ is estimated over the energy range $1 \div 1000\,\text{GeV}$. Note that all the results are referred to event distributions in presence of the ECAL trigger cut.

E^γ [GeV]	1	1.5	2	3	4	5	10	20	50	100	300
$170° \div 180°$	51	62	62	64	68	71	78	82	86	87	74
$160° \div 170°$	47	54	58	62	68	69	73	76	81	82	77

Table 6.2: Efficiency (in %) of the gamma rays identification procedure for incident angles in the ranges $160° \div 170°$ and $170° \div 180°$. The normalization sample consists of photons accepted by the ECAL stand alone trigger.

After all the selections, protons generated on the standard box with a large azimuthal angle θ have been almost completely removed (see Fig. 6.20 (b)). Nevertheless also almost vertical particles can be sources of background, especially at low energy. They can undergo hadronic interaction in the upper parts of the AMS-02 detector and produce secondaries that hit the calorimeter. Since the secondaries don't conserve memory of the initial direction of the parent particle, they can be

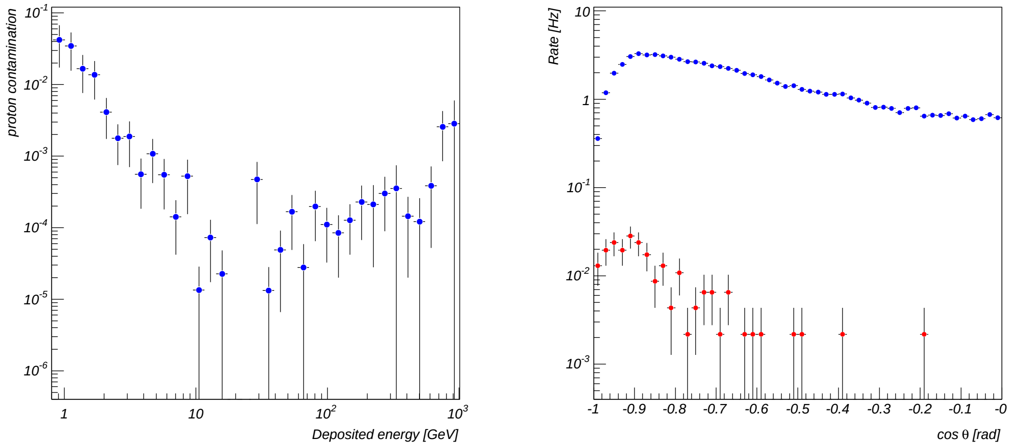

(a) (b)

Figure 6.20: (a) Proton contamination, η_C^p, as a function of deposited energy after the e/p discrimination analysis. The values are referred only to events that pass the LV1 "stand-alone" trigger. (b) Proton rate distribution for $90° < \theta < 180°$ after the trigger (squares) and after all the background rejection cuts are applied (dots); both distributions are flat in ϕ.

reconstructed as inside the TOF acceptance. Moreover, among secondaries, photons from π^0 decay can produce e.m. showers in ECAL, that are indistinguishable from those produced by cosmic γ-rays: in these cases the selection criteria on the shape of the shower is useless. A way to get rid of this irreducible background may consist in developing an analysis tool able to reconstruct the position of interaction vertexes inside the other AMS-02 subdectors. This would lead the rejection power of the instrument to a significative improvement.

Chapter 7

Diffuse gamma rays spectrum reconstruction with ECAL

The results of the analysis of the previous chapter can be applied to estimate the precision expected in the measurement of the galactic diffuse continuum emission, using the AMS-02 electromagnetic calorimeter in *single photon mode*.

In this kind of calculations a major problem derives from the uncertainty about the gamma rays flux to be used as input. The unambiguous detection of diffuse γ radiation is a hard task, due to its very low intensity and the large background of cosmic rays. The available measurements of the spectrum and of the spatial distribution in the GeV to TeV interval are solely based on EGRET data, with reliable precision only below 10 GeV. Above this energy, the accuracy of the measures is limited not only by the bad performances of the detector, but also by the number of collected photons, which is very small; estimates of the flux, although affected by large experimental errors, are possible only in the galactic center region, where the γ-rays intensity reaches its maximum[1].

As extensively treated in chapter 1, the theoretical model of diffuse gamma rays emission that, at present, better fits EGRET data (both in terms of spatial distribution and intensity), is the one proposed in [20], elaborated by means of the GALPROP numerical computer code. In the present simulation, the skymaps derived from this model is used to calculate the input fluxes for photons. In particular, only the emission of the inner Galaxy region (i.e. the sky region delimited

---

[1] For extended sky region, like the inner Galaxy region, the statistical errors on the EGRET data point are very small; the systematic erros dominates and an error bar of ±15 % is usually adopted up to 10 GeV. Above this limit, it is necessary to account for additional uncertainties, because the instrument response is less known: an additional ±5 % systematic error has to be added.

by $-30^\circ < b < 30^\circ$ and $-5^\circ < l < 5^\circ$) is considered where the highest signal over background ratio is expected. Only the background generated by cosmic protons, expected to be about 90 % of the total, was simulated.

7.1 The fast simulator code (AMSFS)

AMS-02 is not a pointed instrument; it will be rigidly attached to the ISS mounted on its long truss. For a precise prediction of the AMS-02 sensitivity to a non-isotropic radiation, like diffuse gamma rays, it is, therefore, necessary to know the region of sky viewed by the detector during its revolutions around the Earth. This can be obtained by simulating the position and the pointing vector of AMS-02, during the ISS evolution in its orbit.

The full AMS-02 Monte Carlo program, combined with the orbital simulation, may become a too heavy tool to estimate the instrument performances in fast and efficient way. For this reason a so called "fast simulation" (AMSFS) was developped, where the complete description of the detector is replaced by a parametrization of the most critical aspects, e.g. the angular resolution, the acceptance, the rejection factors. The AMSFS code [75] allows, once combined with the orbital simulation presented in [76], to determine the number of photons collected from a γ-rays point-like source $\mathbb{S}$, defined by its galactic coordinate and its differential flux.

Let $F_{\mathbb{S}}(E) = d\Phi_{\mathbb{S}}(E)/dE$ be the time-independent differential flux of $\mathbb{S}$, expressed in ph. cm^{-2} s^{-1} GeV^{-1}. According to Eq. 4.1, the number of photons collected by the instruments over an observational period T_{obs}, is:

$$N_{\mathbb{S}}^{\gamma}(E) = \frac{d\Phi_{\mathbb{S}}(E)}{dE} \int \varepsilon(E, S, \Omega, t) d\Omega \boldsymbol{u} \cdot d\boldsymbol{S} dt \tag{7.1}$$

For fixed angle of view Ω and instant t, the integral function $\int \varepsilon(E, S, \Omega, t) \boldsymbol{u} \cdot d\boldsymbol{S}$ determines whether the source is in the detection cone of the detector or not, and gives a measure of the effective area of the detector. Under valid approximation, the photon efficiency ε can be assumed to have a cylindrical symmetry, i.e. $\varepsilon(E, S, \Omega, t) = \varepsilon(E, S, \theta, t)$. Moreover, it's useful to factorize ε as:

$$\varepsilon(E, S, \theta, t) = T_{\mathbb{S}}(\theta, t) \cdot \epsilon(E, S, \theta)$$

where ϵ is the time independent detector efficiency and $T(\theta, t)$ is the so called exposure function. This function specifies how much time is spent observing a celestial source in its detection cone by AMS-02 and how the angle varies between the AMS-

02 zenith and the source; in this specific case, it's equal to 1 if $\mathbb{S}$ is seen under the angle θ at instant t, to 0 otherwise.

Inserting the new parametrization, the Eq. 7.1 becomes:

$$\begin{aligned} N^{\gamma}_{\mathbb{S}}(E) &= \frac{d\Phi(E)}{dE}\int T_{\mathbb{S}}(\theta,t)\Big[\int \epsilon(E,S,\theta)\boldsymbol{u}\cdot d\boldsymbol{S}d\Omega\Big]dt \\ &= \frac{d\Phi(E)}{dE}\int T_{\mathbb{S}}(\theta,t)A_{eff}(E,\theta)d\Omega dt \\ &= \frac{d\Phi(E)}{dE}\int_{FoV} A_{eff}(E,\theta)\int_{T_{obs}} T_{\mathbb{S}}(\theta,t)dtd\Omega \\ &= \frac{d\Phi(E)}{dE}\sum_{I}\langle A_{eff}(E,\theta)\rangle_I \int_I\int_{T_{obs}} T_{\mathbb{S}}(\theta,t)dtd\Omega \\ &= \frac{d\Phi(E)}{dE}\sum_{I}\langle A_{eff}(E,\theta)\rangle_I \, t_I(\mathbb{S}) \end{aligned} \tag{7.2}$$

where $A_{eff}(E,\theta)$ is the time-independent effective area of the detector (as a function of the γ-ray energy and of the incident angle). In Eq. 7.2 the integral over the whole field of view has been substituted by a sum of integrals over intervals I of $\psi = cos\theta$. For each interval, the effective area is replaced by its averaged value:

$$\langle A(E,\psi)\rangle_I = \frac{1}{\Delta\psi_I}\int_{\Delta\psi_I} A(E,\theta)d\psi \tag{7.3}$$

The values of $t_I(\mathbb{S})$ are extracted from the AMS-02 exposition maps, that were computed by the orbital simulation code. In this code, the field of view of the detector is supposed to be restricted to an angular interval of about 2° ($\Delta\psi_I = 0.03$) around the zenithal angle θ_I. The region of sky covered by the instrument is found for each 30-second step as the ISS progresses in its simulated orbit. This is done for a full Space Station precession period ($T_{pre} \sim 2.26$ months). At the end, the code returns a skymap containing the exposition time, $t_I(l,b)$, of each $2^\circ \times 2^\circ$ pixel centered around the point of galactic coordinates (l,b).

The set of maps used in the present study, consisting of 10 skymaps, was realized assuming a total detector field of view of $\sim 45^\circ$ (ψ in the range $-1 \div -0.7$). Fig. 7.1 shows the exposure time for the whole sky, obtained adding up all the 10 skymaps.

If $(l_{\mathbb{S}}, b_{\mathbb{S}})$ are the galactic coordinates of the γ source $\mathbb{S}$, then the exposure time $t_I(\mathbb{S})$ corresponding to an observational period T_{obs}, is $t_I(\mathbb{S}) = (T_{obs}/T_{pre})t_I(l_{\mathbb{S}}, b_{\mathbb{S}})$ and the Eq. 7.2 finally becomes:

$$N^{\gamma}_{\mathbb{S}}(E) = \frac{F_{\mathbb{S}}(E)T_{obs}}{T_{pre}}\cdot\sum_I \langle A(E,\psi)\rangle_I t_I(l_{\mathbb{S}}, b_{\mathbb{S}}) \tag{7.4}$$

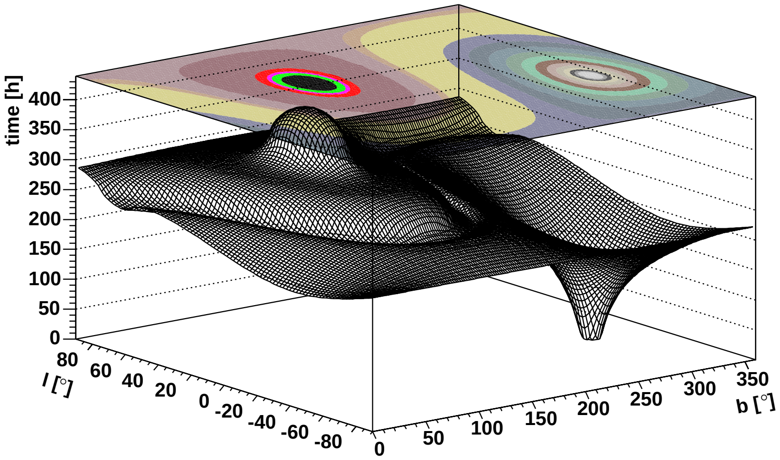

Figure 7.1: All-sky coverage corresponding to a full Space Station precession period (about 70 days). A 2° binning is used for the galactic coordinates axes.

7.2 Detected gamma rays in one year mission

The $AMSFS$ code numerical solves Eq. 7.4 for every point-like gamma rays sources. To study the signals coming from an extended source, like diffuse galactic gamma rays, some implementations in the code are needed.

The whole sky is simulated as divided into pixels of $1^\circ \times 1^\circ$ angular dimensions; each pixel is a source of γ-rays, whose flux is taken from the all-sky emission map produced by the GALPROP code. The total number of photons, $N^{\gamma}_{diffuse}(E)$, detected when AMS-02 will point the inner Galaxy region, is calculated summing the contributions of all the pixels with coordinates inside the range $-30^\circ < l < 30^\circ$ and $-5^\circ < b < 5^\circ$:

$$N^{\gamma}_{diffuse}(E) \quad = \quad \sum_{l,b} F(E,l,b) \cdot \sum_{I} \langle A(E,\psi)\rangle_I t_I(l,b) \tag{7.5}$$

As all the data will be grouped into energy bands, the number of expected γ-rays integrated over intervals K of energy can be calculate:

$$N^{\gamma}_{diffuse}(K) \quad = \quad \sum_{l,b} \langle F(E,l,b)\rangle_{\Delta E_K} \cdot \sum_{I} t_I(l,b) \int_{\Delta E_K} \langle A(E,\psi)\rangle_I dE \tag{7.6}$$

where $\langle F(E,l,b)\rangle_{\Delta E_K}$ is the averaged flux over the energy interval:

$$\langle F(E,l,b)\rangle_{\Delta E_K} = \frac{1}{\Delta E_K} \int_{\Delta E_K} F(E,l,b) dE$$

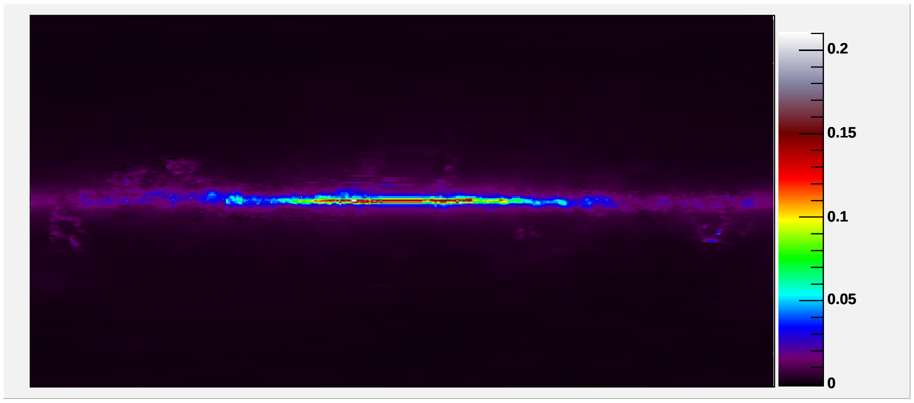

Figure 7.2: Galactic γ-rays emission skymap in $2.2 \div 3.3\,\text{GeV}$ energy range. Intensity as a function of $-180° < l < 180°$ and $-90° < b < 90°$. FITS files adapted from [20].

All-sky emission map

All the output data of GALPROP are recorded as Flexible Image Transport System (FITS) files, a standard computer data format widely used by astronomers to transport, analyze, and archive scientific data files. The FITS file format is more complex than formats for images, like JPEG and GIF. Hence, a specific software is required to manage these files. The skymaps utilised in our study were computed by AstroROOT, a package useful to analyze and display astronomical data in the ROOT framework [78].

GALPROP produces three-dimensional maps of the sky, where the first two parameters of the coordinate system define the longitude and the latitude of the pixel seen from the Sun, the last sets the energy band of the emission. Three different images are available. One takes into account only the γ-rays emission due to inverse-compton scattering, one the bremsstrahlung emission and one refers to π^0 decay. In Fig. 7.2, the image of the galactic diffuse emission, obtained as superimposition of the three before mentioned maps, is shown for energies in $2.2 \div 3.3\,\text{GeV}$ range. The extragalactic γ-ray component is not modelled by GALPROP; as a consequence, for the energy range covered by EGRET, a constant term set to reproduce the high latitude EGRET data is added "by hand" to the emission map.

From the skymaps, the spectrum of the γ-rays can be calculated by integration of the mean intensity, $\langle \mathfrak{I} \rangle$, over l and b. Over a spherical segment, $\langle \mathfrak{I} \rangle$ is defined as:

$$\langle \mathfrak{I} \rangle = \frac{1}{\Delta\Omega} \int_{\Delta\Omega} \mathfrak{I}\, d\Omega$$

where $\mathfrak{I}$ is the emission intensity and $\Delta\Omega$ is the angular dimension of the spherical segment. In Fig. 7.3 the spectrum for the inner Galaxy region is shown. A comparison with the spectrum reported in [20] was useful to verify the absence of errors in our procedure in computation of the all-sky emission map.

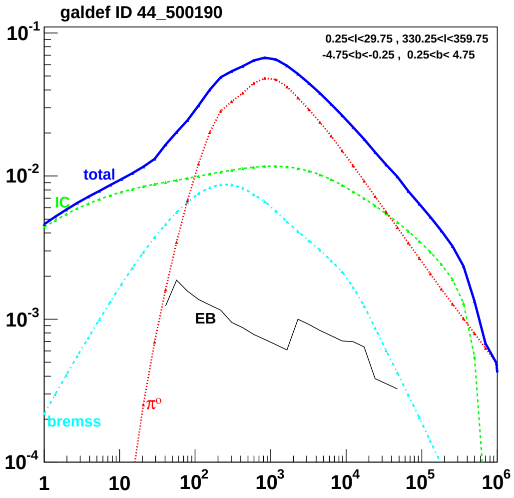

Figure 7.3: Gamma rays spectrum for inner Galaxy region. Fits files adapted from [20].

ECAL effective area

The ECAL effective area depends both on the energy and on the incident angle. In the AMSFS code, it was assumed that the angle and energy dependence can be factorized such that $A_{eff}(E, \psi) = f(E)\ g(\psi)$. This assumption was tested with the results of the present calcutations (see Fig. 7.4).

Following the AMSFS notation, the function, describing the dependence of the dynamic acceptance on the energy, will be referred as $A_1(x)$ (in $cm^2 sr$). The function, describing the dependence of the effective area on the angle, will be referred as $A_2(\psi)$ (in cm^2) (where the variable x is defined as $log_{10}(E)$). In terms of $A_1(E)$ and $A_2(\psi)$, the effective area can be written as:

$$A(x, \alpha) = \frac{A_1(x) A_2(\psi)}{A_1(x_0)} \tag{7.7}$$

where $E_0 = 10^{x_0}$ is the fixed energy for the $A_2(\psi)$ curve, i.e. 20 GeV in the present analysis.

The parametrizations used for $A_1(x)$ and $A_2(\psi)$ are obtained as follows. The function used for fitting the curve $A_1(x)$ is:

$$A_1(x) = 10^4 \cdot ([0]e^{[1]x} + [2]e^{-[3]x} + [4]) \tag{7.8}$$

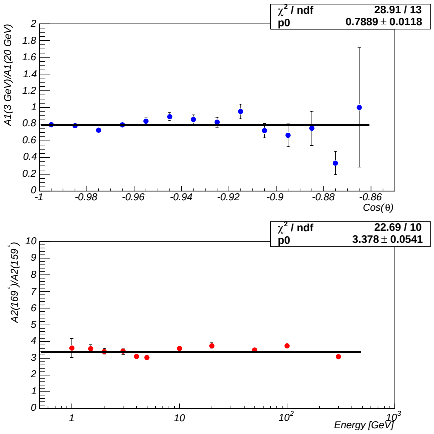

Figure 7.4: Ratio of the values of the effective area taken at fixed energies as a function of $\psi = cos\theta$ (top), or at fixed angles as a function of the energy (bottom). The results of a fit by a constant are shown.

The function used for fitting the curve $A_2(\psi)$ is:

$$A_2(\psi) = 10^4 \cdot \frac{[0]}{\left(1 + e^{\frac{(\psi+[1])}{[2]}}\right)} \tag{7.9}$$

The two fitted curves are shown in Fig. 7.5 (a), (b). The parameters calculated by the fit are the following:

	[0]	[1]	[2]	[3]	[4]
$A_1(x)$	0.08 ± 0.04	0.035 ± 0.025	-0.68 ± 0.34	3.3 ± 0.3	-0.02 ± 0.04
$A_2(\psi)$	0.23 ± 0.01	0.96 ± 0.002	0.02 ± 0.001		

The number of expected photons from the inner Galaxy region, computed by AMSFS for an observational time of 1 year, is reported in Table 7.1 and shown in Fig. 7.6 for energy bands I between 1 and 700 GeV.

7.3 The main background: cosmic protons

As stated in section 4.1, to give an estimate of the fraction of events generated by background, the probability distribution $\mathcal{F}_p(P, S, \phi, \theta, E)$ (i.e. the probability that a proton, with momentum P and direction (ϕ, θ), might be misinterpreted as a photon of energy E) is required. However, an analytically derivation of $\mathcal{F}_p$ turns

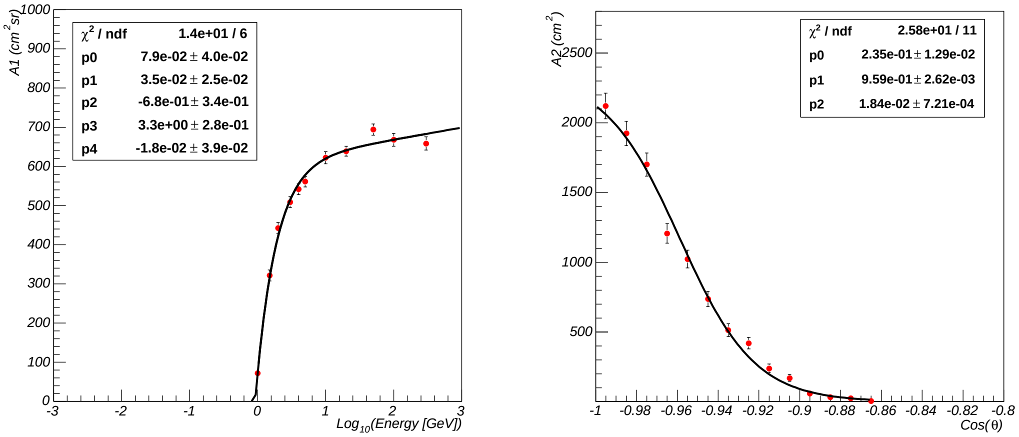

(a) (b)

Figure 7.5: Effective acceptance for the ECAL *single photon* mode. Fit of $A_1(x)$ (a) and $A_2(\psi)$ (b)

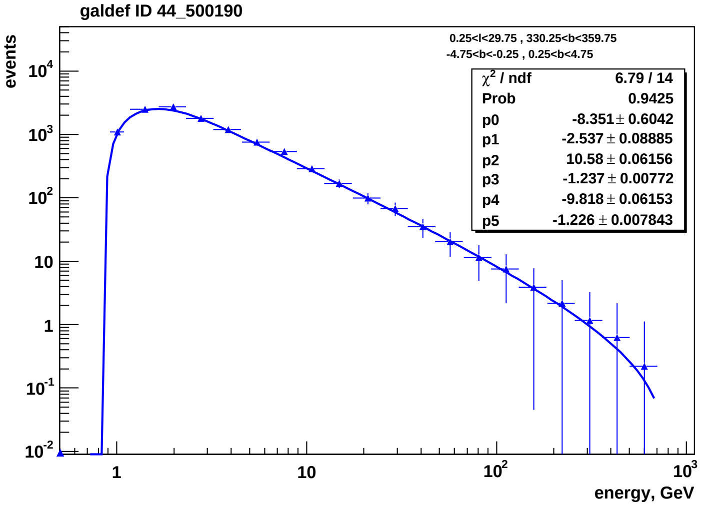

Figure 7.6: Expected photon signal from the inner Galaxy region in one year mission. The signal is integrated over the energy bins.

out to be very difficult in front of the complicated configuration of the AMS-02 experiment. The probability function doesn't depend only on the initial kinematic conditions, but, for example, it's related to the eventual particle interaction with other subdetectors before entering the calorimeter, to the kind and number of secondaries produced in these interactions, to the amount of e.m. core contained into

Energy band [GeV]	Events	Energy band [GeV]	Events
$1 \div 1.2$	1031	$24 \div 34$	63
$1.2 \div 1.6$	2321	$34 \div 47$	33
$1.6 \div 2.3$	2562	$66 \div 93$	11
$2.3 \div 3.2$	1689	$93 \div 130$	7
$3.2 \div 4.5$	1117	$130 \div 182$	4
$4.5 \div 6.3$	703	$182 \div 255$	2
$6.3 \div 8.8$	506	$255 \div 357$	1
$8.8 \div 12$	271	$357 \div 500$	< 1 (0.6)
$12 \div 17$	160	$500 \div 700$	< 1 (0.2)
$17 \div 24$	93		

Table 7.1: Expected number of photons collected in 1 year mission from the inner Galaxy region subdivided in energy bins.

the hadronic cascade.

Again, as in the trigger studies, the MC simulation allows to get rid of the problem. Let $N^p_{gen}(I,J)$ be the number of protons generated on the standard box with momentum in a ΔP_J interval and direction in a $\Delta\psi_I$interval. If $N^p_{sel}(I,J,K)$ is the number of events, among the $N^p_{gen}(I,J)$ ones, that are not rejected by selection criteria and are misinterpreted as photons with energy in the interval ΔE_K, then the ratio:

$$P(I,J,K) = \frac{N^p_{sel}(I,J,K)}{N^p_{gen}(I,J)}$$

can be interpreted as the probability that a proton, generated on the standard box under initial condition (I,J), may be counted as a photon in the K-th interval of the energy spectrum. Hence the number of expected background protons in the K-th bin, $N^p(K)$, is given by:

$$N^p(J) = \sum_{I,J} P(I,J,K) \cdot N^p_{StBox}(I,J) \tag{7.10}$$

where $N^p_{StBox}(I,J)$ is the number of cosmic protons (with an incident direction in $\Delta\psi_I$ and momentum in the interval ΔP_J), that will get into the standard box over the whole observational period.

Starting from Eq. 7.6, the same already used to estimate the signal, the number of protons hitting the standard box, $N^p_{StBox}(I,J)$ is calculated just replacing the flux of γ-rays by the flux of the cosmic protons and the effective area of the ECAL by the effective area of the standard box, A_{StBox}. Unlike photons, primary protons have an isotropic spatial distribution, i.e. $F(P,l,b)_J = F(P)_J$; moreover, A_{StBox} doesn't depend on the momentum of the incident particle, but only on the geometrical layout of the box. These characteristics allow to simplify the computation, reducing Eq. 7.6 to:

$$N^p_{StBox}(I,J) = \langle F(P)\rangle_J \cdot \Delta P_J \sum_I \langle A_{StBox}(\psi)\rangle_I \sum_{l,b} t_I(l,b) \tag{7.11}$$

where $\langle F(P)\rangle_J$ is the averaged value of the flux over the interval ΔP_J and $\langle A_{StBox}(P,\psi)\rangle_I$ is the averaged value of the effective area over the interval $\Delta\psi_I$. Its dependency from ψ was analitically derived as:

$$\begin{aligned} A_{StBox}(\psi) &= S_{StBox}\left(\frac{4}{\pi}|sen\theta| + |cos\theta|\right) \\ &= 15.21 \cdot 10^4 \left[|\psi| + 1.27(1-\psi^2)\right] \end{aligned} \tag{7.12}$$

Primary protons fluxes

According to the AMS-01 data [66], the flux of the cosmic protons of kinetic energy above $\sim 8\,\mathrm{GeV}$ will not depend on the geomagnetic latitude Θ. On the contrary, below this limit, protons will behave differently in various places of the ISS orbit. This effect can not be neglected, not to overestimate or underestimate the background contribution to the final spectrum.

In [76], a set of exposition maps, different from the one used for photons, was computed requiring the geomagnetic latitude of the ISS orbit to be inside a fixed interval M. Three different ranges were taken into account: $0° < \Theta_1 < 17°$, $17° < \Theta_2 < 46°$ and $46° < \Theta_3 < 90°$; in each of these bands, AMS-02 will spend respectively the 22 %, the 51 % and the 27 % of the total observational time.

Choosing the appropriate exposition maps $t_{I,M}(l,b)$, the number of background events, collected when the ISS orbit will have a geomagnetic latitude inside the interval M, are calculated:

$$N^p_{StBox}(I,J,M) = \langle F(P,\Theta)\rangle_{J,M} \cdot \Delta P_J \sum_I \langle A_{StBox}(\psi)\rangle_I \sum_{l,b} t_{I,M}(l,b) \tag{7.13}$$

where $\langle F(P,\Theta)\rangle_{J,M}$ was estimated from the AMS-01 results, averaging over the reported values inside the M interval (see Fig. 7.7). At the end, the estimate of the total number of cosmic protons, entering the standard box during the mission, was obtained as:

$$N^p_{Stbox}(I,J) = \sum_M N^p_{Stbox}(I,J,M) \tag{7.14}$$

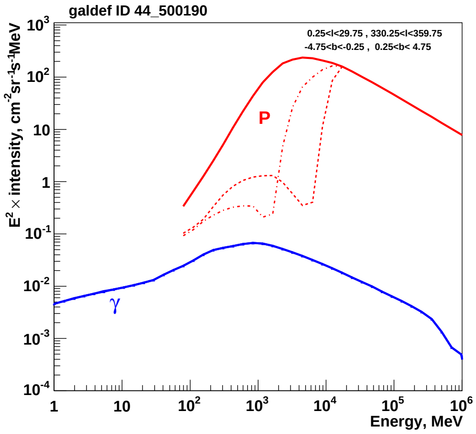

Figure 7.7: Cosmic proton fluxes (red lines) for three different geomagnetic latitude intervals: $0° < \Theta_1 < 17°$ (dot), $17° < \Theta_2 < 46°$ (dash-dot) and $46° < \Theta_3 < 90°$ (continuous). For comparison, the gamma rays flux from the galactic center is also shown. The proton fluxes are derived from AMS-01 data [66].

Fig. 7.8 shows the estimated amount of background events that AMS-02 will collect in 1 year period. The error bars reflect the uncertainty on the proton contamination factors calculated according to the so far collected MC statistics.

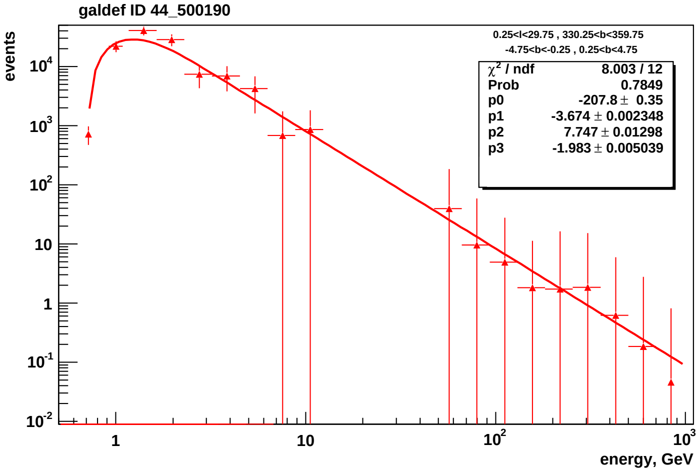

Figure 7.8: AMS-02 *single photon* mode: number of cosmic protons misinterpreted as gamma rays for different energy intervals between 0.7 and 1000 GeV. The observational time corresponds to 1 year.

7.4 Diffuse γ-rays spectrum reconstruction

To try the reconstruction of the γ-rays spectrum of the innner Galaxy region, a simulation of the total number of expected events (signal+background) for three years data taking is required. Both the signal, $N^{\gamma}(K)$, and the background, $N^{p}(K)$, were parametrized as a function of E_K, the central value of the K-th energy interval. This method was chosen as it allows to predict the background also where $N^{p}(K)$ resulted to be zero, due to the lack of MC statistic. The function used for fitting the curve $N^{\gamma}(E_K)$ was:

$$N^{\gamma}(E_K) = 10^4 \cdot ([0]e^{[1]E_K} + [2]{E_K}^{[3]} + [4]{E_K}^{[5]}) \tag{7.15}$$

For $N^{p}(E_K)$, only a single power law was used:

$$N^{p}(E_K) = 10^4 \cdot ([0]e^{[1]E_K} + [2]{E_K}^{[3]}) \tag{7.16}$$

The two fitted curves are shown in Fig. 7.6 and 7.8. The parameters calculated by the fit are:

	[0]	[1]	[2]	[3]
$N^{\gamma}(E_K)$	-8.3 ± 0.6	-2.535 ± 0.09	10.58 ± 0.06	-1.24 ± 0.01
$N^{p}(E_K)$	-207.8 ± 0.3	-3.67 ± 0.01	7.75 ± 0.01	-1.98 ± 0.01
	[4]	[5]		
$N^{\gamma}(E_K)$	-9.82 ± 0.06	-1.23 ± 0.01		

For each energy band, the expected events were simulated by a random extraction from a Poisson distribution with mean value equal to $N^{Tot}(E_K) = T_{obs} \cdot [N^{\gamma}(E_K) + N^{p}(E_K)]$. Fig. 7.9 (a) shows the results of one simulation; the statistical error associated to each point was estimated as the square root of the bin content. It's clear from the picture, that the extraction of the signal from the background is an hard task even in front of the fine $S/\sqrt{N}$ ratio, that was obtained after all the selection criteria (see Fig. 7.9 (b)). Both curves, describing $N^{\gamma}(E_K)$ and $N^{p}(E_K)$, have a very similar shape and the intensity of the signal is comparable to the background only at high energies, where the collected statistic is small.

The method used to successfully fit data, rely on the assumption that the shape of the background spectrum is known forehand and with good precision. This hypothesis is reasonable since, during the mission, this spectrum will be measured in

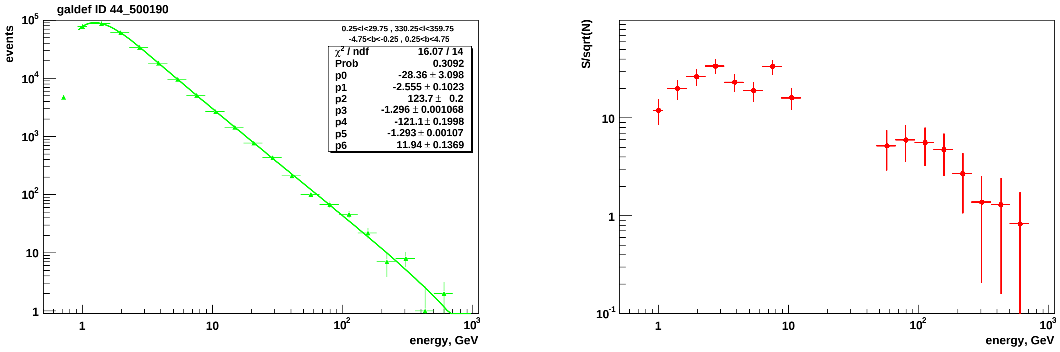

(a) (b)

Figure 7.9: (a) Fit of the simulated Signal+background events. (b) $S/\sqrt{N}$ after 3 years data taking from inner Galaxy region.

any region of the sky, where the γ component is expected to be very low, taking advantage of the isotropy of the CR distribution; for example, the background events could be studied very far from the galactic plane. In the present fitting procedure only the normalization of $N^p(E_K)$ was considered as variable parameter. This gives the possibility to adjust the background level for different lengths of the period of data taking and for different angular dimensions of the pointed sky region. On the contrary, all the parameters of the photon curve were allowed to change.

The fit of one of the simulated data set is shown in Fig. 7.9 (a). From the results of the fit, the number of signal events in each energy bin, $N^{\gamma}_{REC}(E_K)$ and the γ-rays differential flux, $d\Phi^{\gamma}(E)/dE$, for the central value of each bin were reconstructed. In particular, the differential flux was calculated by inverting Eq.7.6:

$$\frac{d\Phi^{\gamma}(E=E_K)}{dE} = \frac{1}{\Delta E_K \Delta\Omega} \cdot \frac{N^{\gamma}_{REC}(E_K)}{\displaystyle\sum_{l,b}\sum_{I} t_I(l,b) \int_{\Delta E_K} \langle A(E,\psi)\rangle_I dE} \tag{7.17}$$

where ΔE_K is the width of the K-th energy interval and $\Delta\Omega$ is angular dimension of the inner Galaxy region.

The accuracy of the measurements obtained by our fitting procedure was estimated by simulating 10000 experiments. For each point of the spectrum the distribution of values of $d\Phi^{\gamma}(E)/dE$ was calculated: the dispersion of the distribution gives the error bar of the flux estimate. Fig. 7.10 shows the resulting precision for the measurement of the spectrum of photons for energies between 1 and 700 GeV. The continuous blue line, already shown in Fig. 7.3, is the spectrum expected by the theoretical model. The two colored-filled areas indicate the confidence intervals

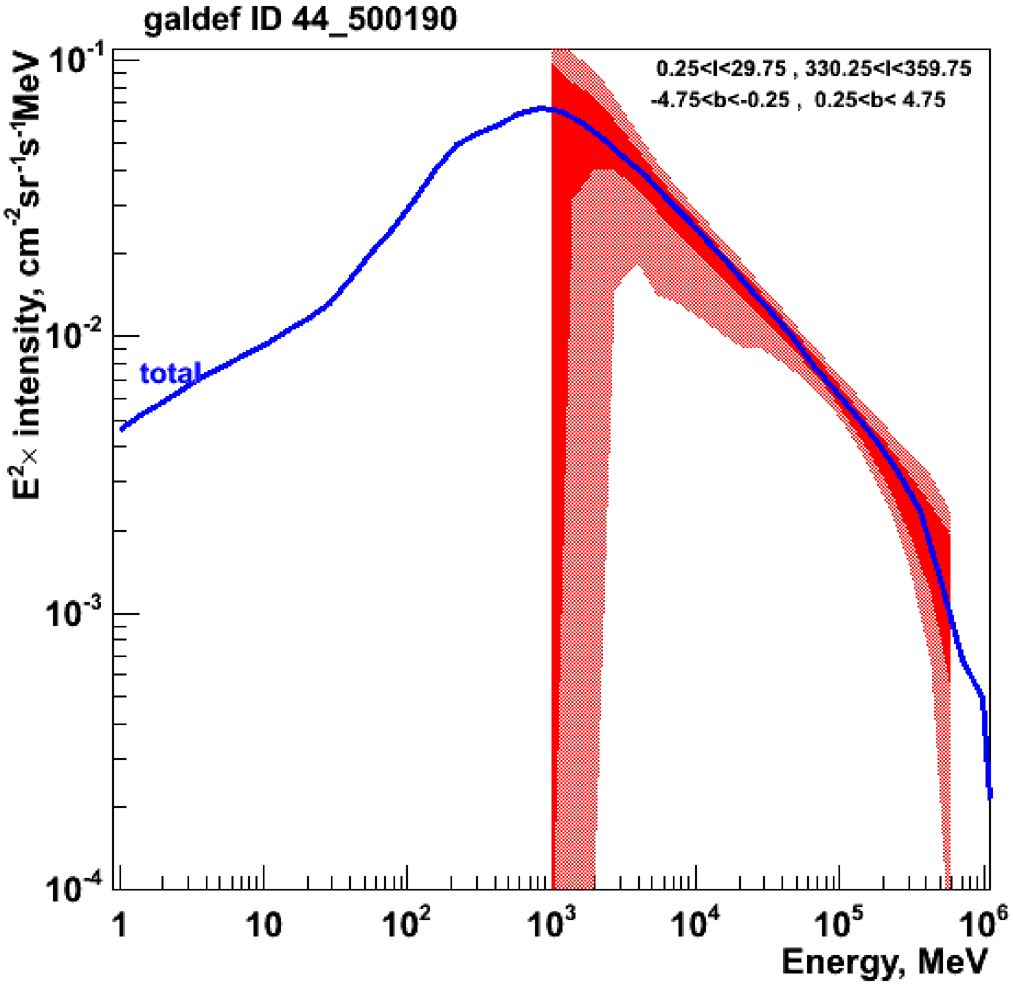

Figure 7.10: Galaxy center region flux measured by AMS-02.

calculated for a confidence level of 68 % (red colored) and the 95 % (light red)[2].

Energy band [GeV]	$\Sigma_{68\,\%C.L.}/S$ [%]	$\Sigma_{68\,\%C.L.}/S$ [%] (Bkg+30 %)	$\Sigma_{68\,\%C.L.}/S$ [%] (Bkg+60 %)
$1.2 \div 1.6$	46	47	49
$1.6 \div 2.3$	29	30	31
$2.3 \div 3.2$	20	21	21
$3.2 \div 4.5$	16	17	17
$4.5 \div 6.3$	14	15	16
$6.3 \div 8.8$	13	14	15
$8.8 \div 12$	12	13	14
$12 \div 17$	11	12	13
$17 \div 24$	10	11	11
$24 \div 34$	9	10	10
$34 \div 47$	8	9	9
$47 \div 66$	8	8	9
$66 \div 93$	8	9	9
$93 \div 130$	9	10	10
$130 \div 182$	12	13	13
$182 \div 255$	16	17	18
$255 \div 357$	24	25	26
$357 \div 500$	35	38	40
$500 \div 700$	56	60	63

Table 7.2: Relative error for different energy bands between 1.2 and 700 GeV. $\Sigma_{68\,\%C.L.}$ is computed as the half width of the confidence interval for the 68 % of confidence level. S is the central value of the confidence interval. The results obtained increasing the background by a 30 % percentage and a 60 % percentage are reported in the third and in the fourth column.

In the Table 7.2 the half width of the confidence intervals, for the 68 % C.L., for different bands of the spectrum between 1 and 700 GeV is reported. In an energy range between 5 and 250 GeV, the accuracy of the measurement will be better than 15 %. Above this range, as expected, the lack of statistics clearly affects the precision of the measure. Below 5 GeV instead, the background contamination is still at too much high level to assure a reliable flux estimate.

---

[2] In the confidence interval computation, the lower and the upper limits were taken symmetrically respect to the peak of the distribution; this peak was calculted by a gaussian fit.

The results of a very preliminary study of the systematic errors are also shown in Table 7.2. To understand how much our results are dependent from a wrong estimate of the proton rejection factors, the expected number of background events was increased by a constant factor of 30 % and 60 %. In both case the changes in the error bars are almost negligible.

Conclusion

One of the main physics goals of the AMS-02 experiment is the measure of diffuse γ-rays spectrum over the so far unexplored energy band between 10 and few hundreds GeV. In AMS-02, the electromagnetic calorimeter, provided with a "stand alone" neutral particle trigger, will be used to directly detect photons.

The AMS-02 electromagnetic calorimeter is under construction and its performances, evaluated on the basis of beam test measurements, meet the requirements to perform a high precision measurement of cosmic ray and gamma ray spectra up to hundreds GeV.

The ECAL "stand alone" trigger has been designed in order to have the highest possible efficiency down to the lowest possible energies. The trigger provides an efficiency larger than 99 % above 5 GeV. Also the efficiency at 1 GeV is appreciable ($\sim$ 20 %). At the same time, even for polar orbits, where the most relevant background fluxes are expected, the total Level 1 trigger rate is limited to $\sim$ 120 Hz (about 20 times less than the initial). The trigger hardware implementation, based on the use of the PMT's last dynode signals, complies with the requirements of power consumption, timing and robustness against major component failures. At present a prototype of the trigger card (ETRG) is under test in Pisa INFN laboratories, showing very promising results.

Among triggered events, a very efficient procedure of background suppression will be strongly required to reveal the small γ-rays signal. To get rid of background (produced by the most abundant cosmic rays components like p, He, C, e^-), it's necessary to look for a specific signature, corresponding to the presence of an electromagnetic shower in the ECAL and to a reconstructed incoming direction inside the TOF acceptance (while almost nothing is found in the other AMS-02 subdetectors). The ECAL 3D imaging is an essential tool to discriminate e.m. showers from hadronic cascade. For this purpose, a set of selection criteria based on the shower shape analysis of events in ECAL has been developed and applied to investigate the AMS-02 capability to directly detect γ-rays in a combined analysis, which makes use of the information of all sub-detectors.

The performances of the proposed signal identification method has been evaluated by using a detailed Monte Carlo simulation of the whole instrument. A global contamination factor of $3.2 \pm 0.5 \cdot 10^{-3}$ is estimated over the energy range $1 \div 1000\,\mathrm{GeV}$, corresponding to a mean photon efficiency of $\sim 75\,\%$. Moreover the dynamic acceptance achievable in *single photon mode* (about $600\,\mathrm{cm}^2\mathrm{sr}$ above $10\,\mathrm{GeV}$), will comparable to the one obtained with the silicon tracker in *conversion mode*.

The results of the MC analysis were applied to estimate the precision expected in the measurement of the diffuse continuum emission from the inner Galaxy region. The direct detection of photons with ECAL clearly reveals to be a very promising technique. Over a three year mission, it will be possible to achieve a precision of the order of $10 \div 15\,\%$ over a large energy range between 5 and 250 GeV improving the best current results in terms of both collected statistics and upper detectable energy. For comparison the indirect dection of converting incident photons, used by both GLAST and AMS-02 itself, will hardly give a reliable precision at energies above 100 GeV: at high energy (especially in absence of a magnetic field) the aperture angle of the electron-positron pairs becomes too small to reconstruct two distinct tracks, even with a silicon tracker. As a consequence, this key signature of the photon events is lost and the background rejection power is considerably reduced.

Appendix A

Summary multivariate analysis

A.1 Discriminant analysis

Discriminant analysis is a set of methods and tools used to distinguish between groups of populations Π_j and to determine how to allocate new observations into groups. In general one has populations $\Pi_j, j = 1, 2, ..., J$ and has to allocate an observation $\boldsymbol{x}$ to one of these groups. A discriminant rule is a separation of the sample space (in general $\mathbb{R}^p$) into sets R_j such that, if $\boldsymbol{x} \in R_j$, it is identified as a member of population Π_j. The main task of discriminant analysis is to find "good" regions R_j such that the error of misclassification is small.

In the following such rules are described when one has to solve the problem of classyfing two populations; for each rule different hypotheses on the distribution probability of the populations are assumed.

A.1.1 Linear discriminant rule

Let the densities of each population Π_j be described by $f_j(\boldsymbol{x})$. The maximum likelihood discriminant rule (ML rule) is given by allocating $\boldsymbol{x}$ to Π_j maximizing the likelihood:

$$L_j(\boldsymbol{x}) = f_j(\boldsymbol{x}) = \max_i f_i(\boldsymbol{x}) \tag{A.1}$$

Mathematically, the sets R_j given by the ML discriminant rule are defined as:

$$R_j = \{\boldsymbol{x} : L_j(\boldsymbol{x}) > L_i(\boldsymbol{x}) \text{ for } i = 1, \ldots, J, i \neq j\} \tag{A.2}$$

By classifying the observation into certain group, a misclassification error may be encountered. For $J = 2$ groups, the probability to put $\boldsymbol{x}$ into group 2 although it belongs to population 1, can be calculated as:

$$P(2|1) = P(X \in R_2|\Pi_1) = \int_{R_2} f_1(\boldsymbol{x})d\boldsymbol{x} \tag{A.3}$$

The misclassified observations create a cost $C(i|j)$ when a Π_j observation is assigned to R_i. The cost structure can be pinned down in a cost matrix:

	Π_1^C	Π_2^C
Π_1^T	0	$C(2\|1)$
Π_2^T	$C(1\|2)$	0

where Π_j^C represents the classified population and Π_j^T represents the true population.

Let π_j be the prior probability of population Π_j, where "prior" means the "a priori" probability that an individual selected at random belongs to Π_j. In this case the conditional probability of classifying an object as belonging from one population Π_1, although it actually comes from the other, becomes:

$$P'(\beta|\alpha) = P(\beta|\alpha)\pi_\alpha \tag{A.4}$$

The expected cost of misclassification (ECM) is given by

$$ECM = C(2|1)P(2|1)\pi_1 + C(1|2)P(1|2)\pi_2 \tag{A.5}$$

The target is the classification of rules, that keep the ECM small or minimize it over a class of rules. The regions R_1 and R_2, that minimize ECM, are defined by the value x, which the following inequalities hold for:

$$\begin{aligned} R_1 &= \left\{ x : \frac{f_1(\boldsymbol{x})}{f_2(\boldsymbol{x})} \geq \frac{C(1|2)}{C(2|1)}\frac{\pi_2}{\pi_1} \right\} \\ R_2 &= \left\{ x : \frac{f_2(\boldsymbol{x})}{f_1(\boldsymbol{x})} < \frac{C(1|2)}{C(2|1)}\frac{\pi_2}{\pi_1} \right\} \end{aligned} \tag{A.6}$$

The minimum ECM depends, therefore, on the ratio of the densities $f_1(\boldsymbol{x})/f_2(\boldsymbol{x})$ or equivalently on the difference $\ln\{f_1(x)\} - \ln\{f_2(x)\}$. Moreover the ML discriminant rule is a special case of the ECM rule for equal misclassification costs and equal prior probabilities.

Let's suppose to have two multinormal populations $\Pi_i = N_p(\boldsymbol{\mu}_i, \Sigma_i)$ with $\Sigma_1 = \Sigma_2 = \Sigma$. Following from Eq. A.6, one has:

$$R_1 : exp\Big[-\frac{1}{2}(\boldsymbol{x} - \boldsymbol{\mu}_1)^T\Sigma^{-1}(\boldsymbol{x} - \boldsymbol{\mu}_1) + \frac{1}{2}(\boldsymbol{x} - \boldsymbol{\mu}_2)^T\Sigma^{-1}(\boldsymbol{x} - \boldsymbol{\mu}_2) \Big] \geq \frac{C(1|2)}{C(2|1)}\frac{\pi_2}{\pi_1} \tag{A.7}$$

and taking logarithm both sides:

$$\frac{1}{2}(\boldsymbol{x}-\boldsymbol{\mu}_1)^\top\Sigma^{-1}(\boldsymbol{x}-\boldsymbol{\mu}_1) \leq \frac{1}{2}(\boldsymbol{x}-\boldsymbol{\mu}_2)^T\Sigma^{-1}(\boldsymbol{x}-\boldsymbol{\mu}_2) - \ln\frac{C(1|2)}{C(2|1)}\frac{\pi_2}{\pi_1} \tag{A.8}$$

, which reduces to the so called "Mahalanobis distance" rule for unity cost case, $C(1|2) = C(2|1) = 1$, and equal prior probabilities, $\pi_2 = \pi_1$.

Rearranging terms leads to:

$$\boldsymbol{a}^\top(\boldsymbol{x}-\boldsymbol{\mu}) \geq \ln\frac{C(1|2)}{C(2|1)}\frac{\pi_2}{\pi_1} \tag{A.9}$$

where $\boldsymbol{\mu} = \frac{1}{2}(\boldsymbol{\mu}_1 + \boldsymbol{\mu}_2)$ and:

$$\boldsymbol{a}^\top = (\boldsymbol{\mu}_1 - \boldsymbol{\mu}_2)^\top\Sigma^{-1}$$

The discriminant rule defined in Eq. A.9 is based on linear combinations and belongs to the family of Linear Discriminant Analysis (LDA) methods. While standard sequential cuts could be visualized as defining a rectangular box in the feature space, the linear discriminant analysis may be visualized as defining a multi-dimensional hyperplane.

A variant of this rule occurs when the parameters of the populations distribution are estimated from data. In this case $\boldsymbol{\mu}_1$, $\boldsymbol{\mu}_2$ are replaced by the sample means $\bar{\boldsymbol{x}}_1$, $\bar{\boldsymbol{x}}_2$ and the Σ is replaced by the pooled covariance matrix:

$$S_p = \frac{(n_1-1)S_1 + (n_2-1)S_2}{n_1+n_2-2} \tag{A.10}$$

where n_1 and n_2 are the number of observations for each population.

A.1.2 Quadratic discriminant rule

When the covariance for both density functions differs, the allocation rule becomes more complicated:

$$\begin{aligned} R_1 : -\frac{1}{2}\boldsymbol{x}^T(\Sigma_1^{-1} - \Sigma^{-2})\boldsymbol{x} + (\bar{\boldsymbol{x}}_1^T\Sigma_1^{-1} - \bar{\boldsymbol{x}}_2^T\Sigma_2^{-1})\boldsymbol{x} - \\ \frac{1}{2}\ln(\frac{|\Sigma_1|}{|\Sigma_2|}) - \frac{1}{2}(\bar{\boldsymbol{x}}_1^T\Sigma_1^{-1}\bar{\boldsymbol{x}}_1 - \bar{\boldsymbol{x}}_2^T\Sigma_2^{-1}\bar{\boldsymbol{x}}_1) \geq \ln\frac{C(1|2)}{C(2|1)}\frac{\pi_2}{\pi_1} \end{aligned} \tag{A.11}$$

The classification regions are defined by quadratic functions. Therefore they belong to the family of Quadratic Discriminant Analysis (QDA) methods. It's easy to see that this quadratic classification rule coincides with the LDA rule when $\Sigma_1 = \Sigma_2$, since the term $\frac{1}{2}\boldsymbol{x}^T(\Sigma_1^{-1} - \Sigma_2^{-1})\boldsymbol{x}$ disappears.

A.1.3 Fisher's discriminant rule

Another approach to the problem stems from R. A. Fisher. His idea was to trasform the multivariate data $\boldsymbol{x}$ to univariate data y such that the y's derived from Π_1 and Π_2 where separated as much as possible. No hypotheses on the priors' distribution were assumed.

Let the difference in the sample means be $\boldsymbol{d} = \bar{\boldsymbol{x}}_1 - \bar{\boldsymbol{x}}_2$ and S_p be the pooled covariance matrix. Consider an arbitrary linear combination of the observed variables:

$$y = \boldsymbol{b}^\top \boldsymbol{x}$$

Then the difference in the sample means of this linear combination is:

$$\bar{y}_1 - \bar{y}_2 = \boldsymbol{b}^\top \boldsymbol{d} \tag{A.12}$$

and the sample variance of y is:

$$Var(Y) = \boldsymbol{b}^\top S_p \boldsymbol{b} \tag{A.13}$$

Fisher asked what linear combination has the greatest difference of the sample means relative to its sample standard deviation; this linear combination discriminates best between the two samples. The algebric problem is to maximize:

$$\frac{(\bar{y}_1 - \bar{y}_2)^2}{Var(Y)} = \frac{(\boldsymbol{b}^\top \boldsymbol{d})^2}{\boldsymbol{b}^\top S_p b} \tag{A.14}$$

with respect to $\boldsymbol{b}$. A solution is:

$$\boldsymbol{b} = S_p^{-1} \boldsymbol{d} \tag{A.15}$$

In this case the $y = \boldsymbol{b}^\top \boldsymbol{x}$ function is called the Fisher's linear discriminant function and can be used to classify a future observation x_0 as coming from the first population, if the distance between y_0 and $\frac{1}{2}(\bar{y}_1 + \bar{y}_2)$ is greater than or equal to 0. With this classification rule one obtains:

$$R_1 : (\bar{\boldsymbol{x}}_1 - \bar{\boldsymbol{x}}_2)^\top S_p^{-1} \boldsymbol{x}_0 \geq \frac{1}{2} (\bar{\boldsymbol{x}}_1 - \bar{\boldsymbol{x}}_2)^\top S_p^{-1} (\bar{\boldsymbol{x}}_1 + \bar{\boldsymbol{x}}_2) \tag{A.16}$$

which, remembering Eq. A.8, correspond to the minimum ECM rule when two multinormal population with same Σ and $C(1|2)\pi_2 = C(2|1)\pi_1$ are present.

The Fisher discriminanting methods can be extend for several populations problem, replacing $\boldsymbol{d}$ by the "between-groups" covariance matrix S_B and using the "within-groups" matrix S_W. In this case Fisher's suggestion is to look for the linear function $\boldsymbol{b}^\top \boldsymbol{x}$ which maximizes the ratio:

$$\frac{\boldsymbol{b}^\top S_B \boldsymbol{b}}{\boldsymbol{b}^\top S_W \boldsymbol{b}} \tag{A.17}$$

That's equivalent to find the $s \leq \min(g-1, p)$ nonzero eigenvalues of $S_W^{-1} S_B$. For each eigeinvalue, the linear combinations between the corresponding eigenvector and $\boldsymbol{x}$, produces a Fisher discriminanting function with a discriminanting power proportional to the magnitude of the eigenvalue.

A.2 Logistic regression

The problem of classifying an observation into one of several populations is discriminant analysis, or classification. Relating qualitative variables to other variables through a logistic functional form is often called "logistic regression". It is well known that if the populations are normal and if they have identical covariance matrices, discriminant analysis estimators are to be preferred over those generated by logistic regression for the discriminant analysis problem. This situation is atypical, however, since in most discriminant analysis applications, at least one variable is qualitative (ruling out multivariate normality). Under nonnormality, the logistic regression model with maximum likelihood estimators is usually preferred for solving both the discriminant analysis problem and the logistic regression problem.

In the *binomial (or binary) logistic regression* the dependent variable is a dichotomy and the independent or predictor variables are of any form. That is, logistic regression makes no assumption about the distribution of the independent variables. They do not have to be normally distributed, linearly related or of equal variance within each group.

Assume as in Sec. A.1 that one has two populations Π_j with $j = 1, 2$ and a single observation to one of these groups is available. Let y be the dichotomus variable, equal to 0 if event belongs to Π_1, equal to 1 if event belongs to Π_2. One is interested in estimating the probability p of each event beeing a 1 or a 0, according to N observed outcomes. The *likelihood principle* says that all inference about a parameter should utilize observed data only through how it affects the likelihood function, i.e. the probability of observing the observed data given p. In our case the likelihood is:

$$\begin{aligned} L(p) &= P(Y = (1,1,1,0,0,1,....,1,1,0)|p) \\ &= p \times p \times p \times (1-p) \times (1-p) \times p \times ... \times p \times p \times (1-p) \\ &= p^{\sum y_i} (1-p)^{N - \sum y_i} \end{aligned} \tag{A.18}$$

It is often more convenient to work with the log-likelihood function.

$$\log L(p) = l(p) = (\sum y_i) \log p + (N - \sum y_i) \log(1-p) \tag{A.19}$$

A good estimator $\hat{p}$ for p is the maximum likelihood estimator, MLE, which selects $\hat{p}$ to be the value of p that would make the observed data most likely: the log-likelihood function (A.19) is maximized by differentiating with respect to p, setting the equation equal to 0, and solve for the MLE, $\hat{p}$.

Usually for each observation, p depends on the independent variables $\boldsymbol{x}_i$, i.e. it's not a scalar but a function $p(\boldsymbol{x}_i)$ of the covariates. Substituting in A.19, one obtains:

$$\begin{aligned} l(p) &= \sum y_i \log p(\boldsymbol{x}_i) + (1-y_i)\log(1-p(\boldsymbol{x}_i)) \\ &= \sum y_i \log \frac{p(\boldsymbol{x}_i)}{1-p(\boldsymbol{x}_i)} + \log(1-p(\boldsymbol{x}_i)) \end{aligned} \tag{A.20}$$

Note that $p(\boldsymbol{x})$ enters the likelihood through the function $\log\frac{p(\boldsymbol{x}_i)}{1-p(\boldsymbol{x}_i)}$, commonly known as the *logit* of p or the log-odds. This function is also known as the *canonical link function* (linking y to $\boldsymbol{x}$) for the logistic regression. Conveniently, it takes values on the whole real line, making it simplifying the modeling process. Reparameterizing $p(\boldsymbol{x})$ as:

$$f(\boldsymbol{x}) = \log \frac{p(\boldsymbol{x})}{1-p(\boldsymbol{x})} \tag{A.21}$$

, from its inverse:

$$p(\boldsymbol{x}) = \frac{1}{1+e^{-f(\boldsymbol{x})}}$$

the log-likelihood for $f(\boldsymbol{x})$ can be calculated as:

$$\begin{aligned} l(f) &= \sum y_i f(\boldsymbol{x}_i) + \log\left(1 - \frac{1}{1+e^{-f(\boldsymbol{x}_i)}}\right) \\ &= \sum y_i f(\boldsymbol{x}_i) - \log\left(1 + e^{f(\boldsymbol{x}_i)}\right) \end{aligned} \tag{A.22}$$

Finally to determine a functional form for $f(\boldsymbol{x})$, using a linear model, one assumes $f(\boldsymbol{x}) = \boldsymbol{b}^\top \boldsymbol{x}$. The logistic log-likelihood for the linear model becomes:

$$l(b) = \sum y_i \boldsymbol{x}_i^\top \boldsymbol{b} - \log(1 + e^{\boldsymbol{x}_i^\top \boldsymbol{b}}) \tag{A.23}$$

Starting from an initial $\boldsymbol{b}_0$ and iteratively computing $\boldsymbol{b}$ as showed in [79], one can determine the maximum likelihood estimator $\hat{\boldsymbol{b}}$. The classification region R_j are defined according to the estimator $\hat{p}$:

$$\hat{p} = \frac{e^{\hat{\boldsymbol{b}}^\top \boldsymbol{x}}}{1+e^{\hat{\boldsymbol{b}}^\top \boldsymbol{x}}} \tag{A.24}$$

Bibliography

[1] P. Sreekumar *et al.*, Phys. Rev. Lett. **70** (1993) 127.

[2] J. Bednarz and M. Ostrowski, Phys. Rev. Lett. **80** (1998) 3911 [arXiv:astro-ph/9806181].

[3] S. P. Swordy *et al.*, Astrophys. J. **349** (1990) 625.

[4] M. Giller and M. Lipski, J. Phys. G **28** (2002) 1275.

[5] H. Nakanishi and Y. Sofue, Publ. Astron. Soc. Jap. **55** (2003) 191 [arXiv:astro-ph/0304338].

[6] A. Dar and A. De Rujula, Mon. Not. Roy. Astron. Soc. **323** (2001) 391 [arXiv:astro-ph/0005080].

[7] T. M. Dame, D. Hartmann and P. Thaddeus, arXiv:astro-ph/0009217.

[8] R. Beck, arXiv:astro-ph/0012402.

[9] W. R.Webber, G. A.Simpson and H. V.Cane, Astrophys. J. **236** (1980) 448

[10] S. D. Hunger *et al.*, Astrophys. J. **481** (1997) 205.

[11] D. D. Dixon *et al.*, New Astron. **3** (1998) 539 [arXiv:astro-ph/9803237].

[12] A. W. Strong, J. R. Mattox A&A **308** (1996) L21.

[13] A. W. Strong and I. V. Moskalenko, arXiv:astro-ph/9812260.

[14] A. W. Strong, I. V. Moskalenko and O. Reimer, Astrophys. J. **537** (2000) 763 [Erratum-ibid. **541** (2000) 1109] [arXiv:astro-ph/9811296].

[15] E. S. Seo, V. S. Ptuskin, Astrophys. J. **431** (1994) 705

[16] J. J. Connell, Astrophys. J. **501** (1998) L59

[17] I. V. Moskalenko, A. W. Strong, J. F. Ormes and M. S. Potgieter, Astrophys. J. **565** (2002) 280 [arXiv:astro-ph/0106567].

[18] I. V. Moskalenko and A. W. Strong, Astrophys. J. **493** (1998) 694 [arXiv:astro-ph/9710124].

[19] M. Pohl and J. A. Esposito, Astrophys. J. **507** (1998) 327

[20] A. W. Strong, I. V. Moskalenko and O. Reimer, arXiv:astro-ph/0406254.

[21] A. W. Strong, I. V. Moskalenko and O. Reimer, arXiv:astro-ph/0405441.

[22] A. W. Strong and I. V. Moskalenko, arXiv:astro-ph/0106505.

[23] A. W. Strong, I. V. Moskalenko and O. Reimer, arXiv:astro-ph/0306346.

[24] F. W. Stecker and M. H. Salamon, Astrophys. J. **464** (1996) 600

[25] M. H. Salamon and F. W. Stecker, Astrophys. J. **493** (1998) 547

[26] A. Dolgov and J. Silk, Phys. Rev. D **47** (1993) 3144.

[27] D. N. Page and S. W. Hawking, Astrophys. J. **206** (1976) 1

[28] S. W. Hawking, Scientific. American **236** (1977) 34

[29] N. Y. Gnedin and J. P. Ostriker, Astrophys. J. **400** (1992) 1

[30] G. Jungman, M. Kamionkowski and K. Griest, Phys. Rept. **267** (1996) 195 [arXiv:hep-ph/9506380].

[31] F. W. Stecker, Astropart. Phys. **11** (1999) 83 [arXiv:astro-ph/9812286].

[32] P. Sreekumar *et al.*, Astrophys. J. **494** (1998) 523

[33] R. Mukherjee and J. Chiang, Astropart. Phys. **11** (1999) 213 [arXiv:astro-ph/9902003].

[34] J. Chiang and R. Mukherjee, Astrophys. J. **496** (1998) 752

[35] P. Sreekumar *et al.*, Astrophys. J. **400** (1992) L67

[36] A. Dar and N. J. Shaviv, Phys. Rev. Lett. **75** (1995) 3052 [arXiv:astro-ph/9501079].

[37] M. Pohl, arXiv:astro-ph/9706151.

[38] Y. C. Lin *et al.*, Astrophys. J. **525** (1999) 191

[39] J. R. Ellis, T. Falk, G. Ganis and K. A. Olive, Phys. Rev. D **62** (2000) 075010 [arXiv:hep-ph/0004169].

[40] L. Bergstrom, Rept. Prog. Phys. **63** (2000) 793 [arXiv:hep-ph/0002126].

[41] A. Tasitsiomi and A. V. Olinto, Phys. Rev. D **66** (2002) 083006 [arXiv:astro-ph/0206040].

[42] J. F. Navarro, C. S. Frenk and S. D. M. White, Astrophys. J. **462** (1996) 563 [arXiv:astro-ph/9508025].

[43] "GLAST: Exploring nature's highest energy processes with the Gamma Ray Large Area Space Telescope", NASA document **NP-2000-9-107-GSFC** (2001), http://glast.gfsc.nasa.gov/resources/brochures/gsd/.

[44] B. Alpat, Nucl. Phys. Proc. Suppl. **54B** (1997) 335.

[45] A. D. Dolgov, Nucl. Phys. Proc. Suppl. **113** (2002) 40.

[46] G. A. Steigman, Rev. Astr. Astrophys. **14** (1976) 339.

[47] A. G. Cohen, A. De Rujula and S. L. Glashow, Astrophys. J. **495** (1998) 539 [arXiv:astro-ph/9707087].

[48] P. Maestro, "Dark Matter Search in the Positron Channel with the AMS-02 Experiment", PhD Thesis, Universit degli Studi di Siena, 2003.

[49] E. Falchini, PhD Thesis, Universit degli Studi di Siena, 2004.

[50] G. Valle, "Dark Matter Search in the Gamma Channel with the AMS-02 Experiment", PhD Thesis, Universit degli Studi di Siena, 2003.

[51] F. Hauler *et al.*, IEEE Trans. Nucl. Sci. **51** (2004) 1365.

[52] L. Baldini *et al.*, arXiv:hep-ex/0108042.

[57]

[54] B. Blau *et al.*, Nucl. Instrum. Meth. A **518** (2004) 139.

[55] E. Cortina [AMS-02-Tracker Collaboration], *Prepared for 28th International Cosmic Ray Conferences (ICRC 2003), Tsukuba, Japan, 31 Jul - 7 Aug 2003*

[56] M. Buenerd *et al.*, arXiv:astro-ph/0306224.

[57] C. H. Lin, AMS Internal Note **AMS-JT-JLV1-LOGIC-R01A** (2003), http://linch.home.cern.ch/linch.

[58] D. Casadei *et al.*, AMS Internal Note (2004), in preparation.

[59] P. Maestro, AMS Internal Note **2003-01-01** (2003).

[60] G. Lamanna, AMS Internal Note **2001-05-01** (2001).

[61] F. Cervelli *et al.*, Nucl. Instrum. Meth. A **490** (2002) 132.

[62] F. Cadoux *et al.*, Nucl. Phys. Proc. Suppl. **113** (2002) 159.

[63] M. Sapinski, AMS Internal Note **2004-02-02** (2004).

[64] G. Lamanna, AMS Internal Note **2003-03-03** (2003).

[65] J. Alcaraz and I. Sevilla, AMS Internal Note **2004-03-07** (2004).

[66] J. Alcaraz *et al.* [AMS Collaboration], Phys. Lett. B **472** (2000) 215 [arXiv:hep-ex/0002049].

[67] J. Alcaraz *et al.* [AMS Collaboration], Phys. Lett. B **494** (2000) 193.

[68] J. Alcaraz *et al.* [AMS Collaboration], Phys. Lett. B **484** (2000) 10 [Erratum-ibid. B **495** (2000) 440].

[69] V. Choutko, G. Lamanna, A. Malinin, Int. J. Mod. Phys. **A17** (2002) 1817.

[70] R. Brun *et al.*, GEANT3, CERN-DD/EE/84-1 (Revised 1987).

[71] L. J. Gleeson, W. I. Axford, Astrophys. J. **154** (1968) 1011.

[72] U. Amaldi, Phyis. Scripta **154** (1981) 409.

[73] J.F Hair, R. L. Tatham, R. E. Anderson, W. Black, “Multivariate data analysis”, Prentice Hall, 5-th edition (1998).

[74] W. Hardle, L. Simar, “Applied Multivariate Statistical Analysis”, Springer (2003).

[75] J. Bolmont, M. Sapinski, I. Sevilla Noarbe, G. Lamanna, AMS Internal Note **2004-02-01** (2004).

[76] I. Sevilla, AMS Internal Note **2004-03-03** (2004).

[77] http://www.gamma.mpe.mpg.de/ aws/aws.html

[78] INTEGRAL Science Data Centre (ISDC),
http://isdc.unige.ch/Soft/AstroRoot/

[79] G. Ridgeway,
http://www.i-pensieri.com/gregr/ModernPrediction/L2logistic.pdf (2004).